eXPRESS Polymer Letters Vol.2, No.9 (2008) 614
Available online at www.expresspolymlett.com
DOI: 10.3144/expresspolymlett.2008.73

Editorial corner – a personal view

Shape memory polymers and their future developments

B. K. Kim[*]

Department of Polymer Science and Engineering, Pusan National University, Busan 609-735, Korea

Since the shape memory (SM) effect was first utilized for the production of heat shrinkable polyethylene as far back as 1951, it took over 30 years to industrialize the same effect with block copolymers by Japanese companies. However, most works by then were based on their commercial products as documented in patents, and detailed structure-property relationships were sparse in open literatures. Since late 1990s, SM polymers (SMP) have drawn intensive scientific attentions as functional materials with ample potential applications.

SMP recovers its original shape from a large deformation when exposed to a stimulus which is mostly heat. Light, electric and magnetic fields may also be used to trigger shape change in suitable SMPs. However, these stimuli are generally used to generate heat. SM effect results from the combination of morphology and processing program.

Morphologically, SMP consists of fixed (hard) segments and reversible (soft) segment, or their aggregations (phases). Transition temperature of soft segment is switching temperature (T_s). So, block and segmented copolymers are major classes of SMP. Fixed phase contains physical or chemical cross-links which are thermally stable above T_s. It is typically dispersed in reversible phase and is triggered by external stimuli. Morphology of soft segment and intercross-link distance determine the recoiling above T_s.

SMP has rooms for performance improvement in strain fixity, recovery, and durability. Moreover, reversibility rather than the one way operation, and high recoiling force would open up a new era of SMP. Switching by light, pH, pressure, sound, moisture, etc will make the materials more versatile. Multifunctionalization like the coupling of SM effect with biocompatibility and biodegradability will find biomedical device applications.

Skilled molecular design for specific environment is of prime importance. Hybridization with other polymers and inorganic fillers in nano-order are other choices. Multiple SM behavior where strain is recovered in multiple steps could be designed from multiphase polymers. Simple addition of fillers often gives partial success as to SM effect. However, when fillers are chemically bonded onto the polymer chains, excellent SM performances can be achieved. SMP is a rapidly moving area and a lot more are expected to come in the near future.

Prof. Dr. Byung K. Kim
Member of International Advisory Board

---

[*] Corresponding author, e-mail: bkkim@pnu.edu

eXPRESS Polymer Letters Vol.2, No.9 (2008) 615–622
Available online at www.expresspolymlett.com
DOI: 10.3144/expresspolymlett.2008.74

Domain of validity and fit of Gent-Thomas and Flory-Erman rubber models to data

T. Beda[1*], *H. Gacem*[2], *Y. Chevalier*[2], *P. Mbarga*[1]

[1]Department of Industrial and Mechanical Engineering, Ecole Nationale Supérieure Polytechnique, University of Yaounde I, BP 8390 Yaounde, Cameroon
[2]Institut Supérieur de Mécanique de Paris, Laboratoire d'Ingénierie des Structures Mécaniques et des Matériaux (LISMMA), Supméca de Paris. 3, rue F. Hainaut, 93407 Saint-Ouen Cedex, France

Received 13 May 2008; accepted in revised form 10 July 2008

Abstract. In rubber investigation, many strain energy models have been proposed for the hyperelastic behavior. One of earlier models, that of Gent-Thomas (1958), based on theoretical and experimental considerations, has been forsaken in the rubber modeling literature, because of difficulties in establishing its domain of validity and then evaluating the relative mechanical parameters. This note presents how to validate a partial model that is suitable just in a portion of the complete experimental domain: moderate, transition and stiffening deformations. Illustrations of domain validation for the incomplete phenomenological Gent-Thomas model and a simulation with the constrained chain model of Flory-Erman are exposed and their numerical characterisation from experimental data is also revealed.

Keywords: *rubber, partial modeling, domain validation, mechanical properties, identification process*

1. Introduction

In behavior modeling of hyperelastic materials, the stress-stretch relations are obtained from the strain energy function. The problem is the mastery of this strain energy function W. In material investigation, many starting forms of this energy have been proposed [1–5]. The use of an energy form depends on the mastery of parameters estimation from experimental acquisitions (or from molecular considerations). A principal reason why some earlier interesting models such as that of Gent-Thomas [2] were not often used, lies in the fact that the common procedure (least squares in single process) of parameter estimation does not allow their identification within a restricted region of the experimental (complete) domain. However, the earlier practical Mooney (or Mooney-Rivlin) model [1], which unfortunately fails in predicting other deformation modes such as shear or biaxial deformation, is frequently used (even recently [6]), in hyperelastic literature because its validation and fitting are well mastered by the use of the Mooney plot technique (the plot of the reduced stress as a function of reciprocal stretch in extension-compression). Let us note that according to Mooney model, the secant shear modulus is independent of the stretch, i.e., is constant. This is incorrect since experiment shows that the reduced shear stress varies as the stretch varies [7, 8].

The fit of a model to data is an essential means for validating a model in hyperelasticity [8, 9].

2. Hyperelastic uniaxial behavior

The uniaxial behavior of incompressible, homogenous and isotropic Green materials is given by Equation (1):

---

[*] Corresponding author, e-mail: tbeda@yahoo.com

$$\sigma_n = \frac{\partial W}{\partial \lambda} \tag{1}$$

where W is the strain energy function, σ_n the nominal stress and λ the stretch. This law can be rewritten in the strain invariants-based by Equation (2):

$$\sigma_n(\lambda) = 2\left(\lambda - \frac{1}{\lambda^2}\right)\left(\frac{\partial W}{\partial I_1} + \frac{1}{\lambda}\frac{\partial W}{\partial I_2}\right) \tag{2}$$

where $I_1 = \lambda^2 + 2\lambda^{-1}$ and $I_2 = 2\lambda + 2\lambda^{-2}$ are respectively the first and the second strain invariants.
The reduced stress $\phi(\lambda)$ is defined by Equation (3):

$$\phi(\lambda) = \frac{\sigma_n}{(\lambda - \lambda^{-2})} = \frac{\sigma}{(\lambda^2 - \lambda^{-1})} \tag{3}$$

where σ is the stress (Cauchy stress).

3. Validating domain and fitting the phenomenological Gent-Thomas model

The choice of the continuum Gent-Thomas model [2] lies in the fact that this model verifies theoretical and experimental requirements as concerns the dependence of the energy strain function on the strain invariants I_1, I_2; and conditions on $\partial W/\partial I_1$ and $\partial W/\partial I_2$ [10, 11]. The Gent-Thomas model is given by Equation (4):

$$W_{GT} = K_1(I_1 - 3) + K_2 \ln\frac{I_2}{3} \tag{4}$$

where K_1 and K_2 are material characteristics. The relative uniaxial behavior law can be rewritten, from Equations (2) and (3), as in Equation (5):

$$\phi_{GT} = 2\left(K_1 + K_2\frac{\lambda}{2\lambda^3 + 1}\right) \tag{5}$$

where ϕ_{GT} is the reduced stress according to the Gent-Thomas model.

3.1. Ordinary procedure for parameters identification

The ordinary least squares procedure considers as base of approximation $<P(\lambda)>$ given by Equation (6):

$$\langle P(\lambda)\rangle = \left\langle \xi_1(\lambda) = 1, \xi_2(\lambda) = \frac{\lambda}{2\lambda^3 + 1}\right\rangle \tag{6}$$

$\xi_k(\lambda)$ is a generating function. This leads to the estimated parameters K_1 and K_2 given by Equation (7):

$$\begin{Bmatrix} K_1 \\ K_2 \end{Bmatrix} = \begin{bmatrix} L_{11} & L_{12} \\ L_{12} & L_{22} \end{bmatrix}^{-1} \begin{Bmatrix} f_1 \\ f_2 \end{Bmatrix} \tag{7}$$

The matrix coefficients are given by Equations (8) and (9):

$$L_{ij} = \sum_{k=1}^{M} \xi_i(\lambda_k)\xi_j(\lambda_k) \tag{8}$$

$$f_i = \sum_{k=1}^{M} \xi_i(\lambda_k)\phi(\lambda_k) \tag{9}$$

Thus, Equations (10), (11), (12), (13) and (14) give the values of the coefficients:

$$L_{11} = M \tag{10}$$

$$L_{12} = \sum_{k=1}^{M} \frac{\lambda_k}{2\lambda_k^3 + 1} \tag{11}$$

$$L_{22} = \sum_{k=1}^{M} \frac{\lambda_k^2}{(2\lambda_k^3 + 1)^2} \tag{12}$$

$$f_1 = \sum_{k=1}^{M} \frac{\sigma_{nk}}{\lambda_k - \lambda_k^{-2}} \tag{13}$$

$$f_2 = \sum_{k=1}^{M} \frac{\lambda_k \sigma_{nk}}{(2\lambda_k^3 + 1)(\lambda_k - \lambda_k^{-2})} \tag{14}$$

where (λ_k, σ_{nk}) are experimental data.
The estimated parameters are recorded in Table 1.

Table 1. Estimated parameters of the Gent-Thomas model from Pak-Flory elastomer data

Parameters	K_1	K_2
Simple Process (SP)	0.0707	0.1321
Multi-Stage Process (MSP)	0.0671	0.1456

3.2. Multi-stage procedure

Let us consider, for $x \in V_N$, $\xi_N(x)$ being the equivalent function of the function $y(x)$, this leads to Equation (15):

$$y(x) \approx a_N \xi_N(x) \quad \text{for} \quad x \in V_N \tag{15}$$

Plotting $y(x)$ versus $\xi_N(x)$, that is, $(\xi_N(x), y(x))$, should give a linear curve for $x \in V_N$. The method consists in plotting the curve $(\xi_k(x), y(x))$ by varying k to get a linear portion for certain values of x, which defines the identification sub-domain. The partial solution $\xi_k(x)$ is then determined and the weighting coefficient a_k is given by the slope of the relative linear curve. Reiterating this procedure leads to the following recurrence formula [12] given by Equation (16):

$$y_k(x) = y(x) - \sum_{j=0}^{k-1} a_{N-j}\xi_{N-j}(x); \; k = 1, N$$

$$y_0(x) = y(x) \tag{16}$$

where $y_k(x)$ is the function to be identified in the sub-domain V_k.

To evaluate the Gent-Thomas parameters, one has first to look for the valid domain of the model. From Equations (3) and (5), a change of variable is not possible, because the change $X = \lambda/(2\lambda^3 + 1)$ is not a univocal function. This necessitates the use of the graphical step-by-step approach [12]. As previously stated, when plotting $\phi(x)$ versus $\lambda/(2\lambda^3+1)$, the domain where the curve is linear corresponds to the valid domain of the Gent-Thomas model, Figures 1a, 1b. The value of the parameter K_2 is given by the gradient of the straight line and that of K_1 is the intercept. These parameters can be graphically estimated or, for more accuracy, can be evaluated by the least squares method within the appropriate domain [13] identified (within the linear curve area).

3.3. Results

Let us consider for illustration purposes: on one hand, data of uniaxial tension of the Pak-Flory elastomer [14], Figure 1; and on the other hand, those of the Treloar rubber [15], Figure 2.

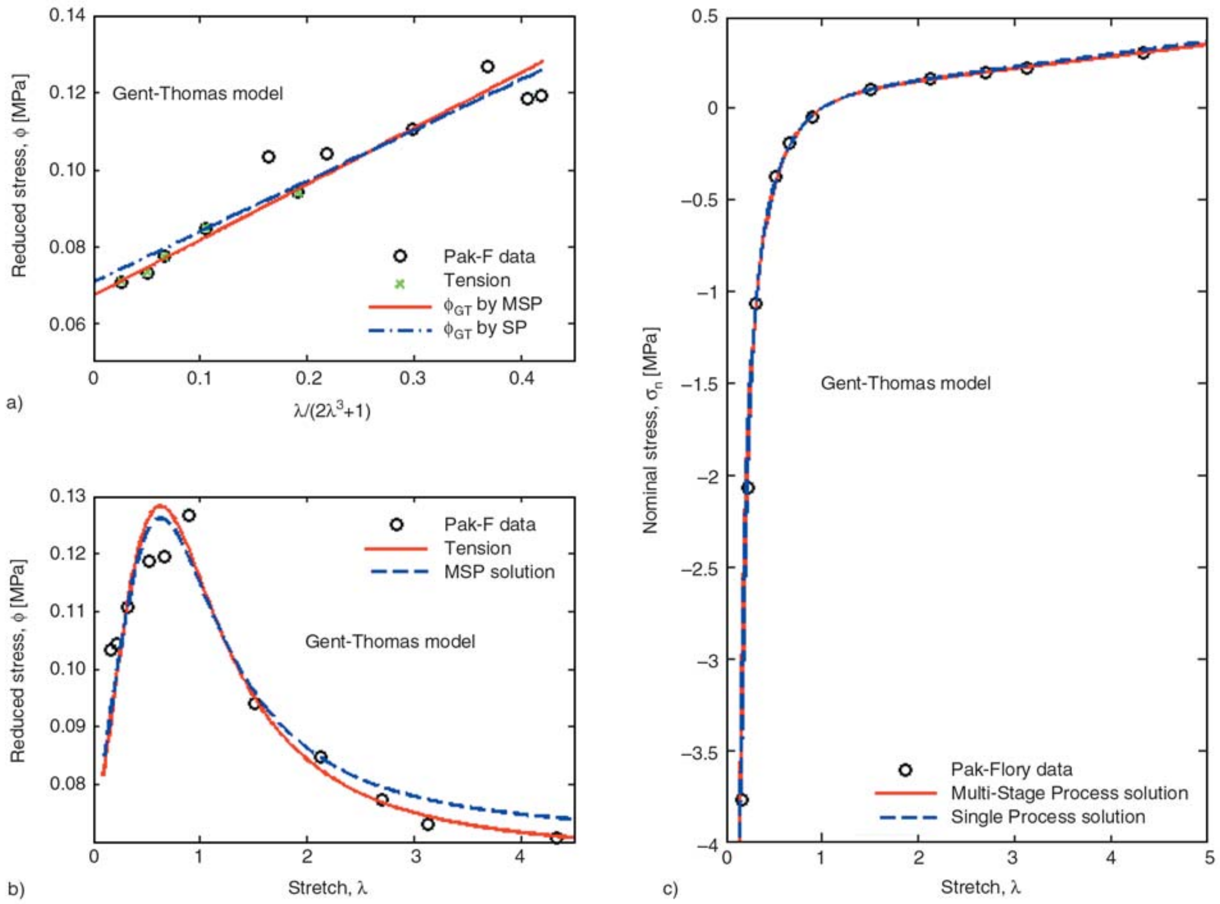

Figure 1. Validating and fitting the Gent-Thomas model to Pak-Flory elastomer data. (a): validating domain of interest and parameters evaluation (Straight line); (b): estimated reduced curves compared to data; (c): estimated compression-extension curves compared to data.

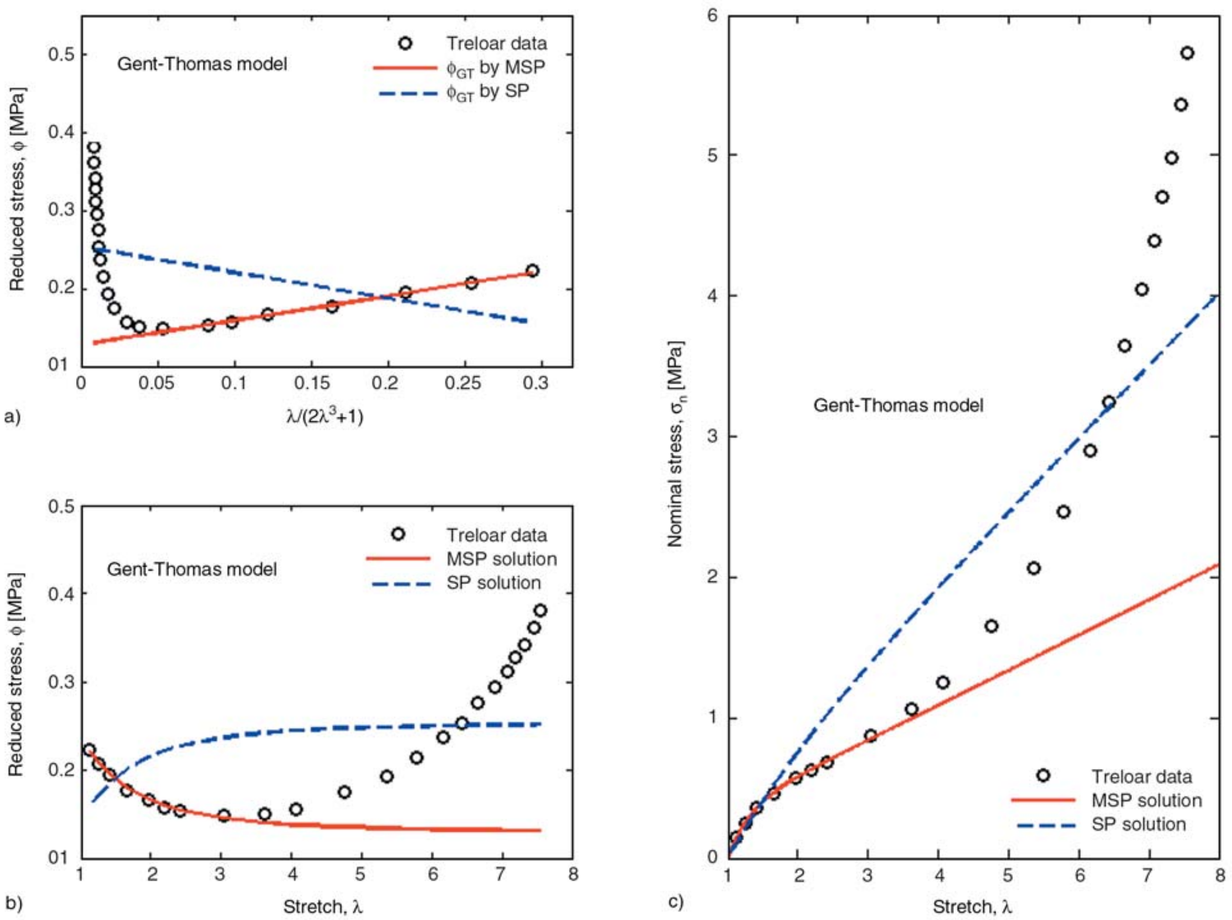

Figure 2. Validating and fitting the Gent-Thomas model to Treloar rubber data. (a): validating domain of interest and parameters evaluation (Straight line); (b): estimated reduced curves compared to data; (c): estimated compression-extension curves compared to data.

– For the Pak-Flory data, one can use the single as well as the multi-stage procedure. The multi-stage procedure (where only extension data are taken into account for the resolution) permits just more precision on the estimated parameter values, Figure 1a. The parameter values obtained are recorded in Table 1. Figure 1b, 1c shows a good fit of data from compression to moderate tension, by the single as well as the multi-stage process. The Gent-Thomas model is valid over the entire experimental deformation domain of Pak-Flory, i.e., moderate and transition deformation zones. For this band of deformation, the use of the ordinary (single process) least squares procedure remains operational for validating and fitting the Gent-Thomas model to data.

– For the Treloar data, one sees in Table 2 that the coefficient K_2 is negative-valued. This is at variance with the regression analysis of the constrained energy function by Johnson *et al.* [16]. From Figure 2a, we see that the single process is irrelevant. Figure 2b, 2c shows that the solution curves diverge markedly from the whole experimental data by the single process. While by the multi-stage process, a good fit of data is observed from small to moderate deformations though a noticeable deviation appears at large deformations. This is understandable because one does not a priori know the domain where the restricted Gent-Thomas model is suitable. The ordinary procedure uses the whole experimental data to evaluate the energy parameters in a single process. Considering a single process means that the reduced stress should be linear in the whole deformation region when plotting $\phi(\lambda)$ versus the generating function $\xi_2(\lambda)$. This is not always accurate since experimental data do not corroborate it in Figure 2a. This is due to the fact that the Treloar experimental domain is complete: moderate deformation field, transition zone and stiffening domain. This shows that the Gent-Thomas model is only valid in a limited deformation region, i.e., stretches under the upturn point of the reduced stress curve (in other words, at the falling part of the curve),

Table 2. Estimated parameters of the Gent-Thomas model from Treloar rubber data

Parameters	K_1	K_2
Simple Process (SP)	0.2543	–0.3296
Multi-Stage Process (MSP)	0.1286	0.3137

Figure 2b. Consequently, it is a partial model, which is applicable and functional in a limiting area, within a restricted deformation domain of interest located under the inflexion point of the tension curve, Figure 2c. Table 2 presents estimated parameters by the multi-stage process compared to those by the single process. Thus, by the multi-stage process, one first of all looks for the valid domain of a model before evaluating relative parameters. For a rubber material, if one considers just two deformation zones: the first zone, where the tension curve is concave, as moderate stretches; the other zone, where it is rather convex, as the high deformations region, one can deduce that the Gent-Thomas model is suitable only for moderate stretches, i.e., under the stiffening deformation zone, Figure 2c.

4. Simulation: Validating domain and fitting the molecular Flory-Erman model

It is well known that for a constrained chain model, parameters are obtained from molecular consideration. But we propose a simulation approach for estimating these parameters by means of a numerical approach in order to appreciate the efficiency of the studied method.

4.1. Uniaxial behavior law

The constrained chain model of Erman-Mannorie [17, 18] is given by Equation (17):

$$W_{EM} = \frac{1}{2}\eta kT\sum_{j=1}^{3}(\lambda_j^2 - 1) + \frac{1}{2}\eta kT\sum_{j=1}^{3}\left(\frac{N}{\eta}\left[B_j + D_j - \ln(1+B_j) - \ln(1+D_j)\right]\right) \tag{17}$$

where B_j, D_j and $h(\lambda)$ are given by Equations (18), (19) and (20):

$$B_j = \frac{\kappa h(\lambda_j)\left[1-\left(1-\frac{2}{\gamma}\right)^{2/3}\right](\lambda_j^2 - 1)}{[\lambda_j^2 + h(\lambda_j)]^2} \tag{18}$$

$$D_j = \frac{\lambda_j^2 B_j}{h(\lambda_j)} \tag{19}$$

$$h(\lambda_j) = \kappa\left[1 + \frac{\left(1-\frac{2}{\gamma}\right)^{2/3}(\lambda_j^2 - 1)}{3}\right] \tag{20}$$

η is the cyclic rank of a network, k the Boltzmann's constant, T the absolute temperature, γ is the number of chains meeting at a junction (the functionality of the network junction), κ is a measure of strengths of the constraints, N is the chain density ($\eta = N/2$ for a perfect tetra functional network).

For the Flory-Erman model [18, 19] γ is equal to two, so $h(\lambda)$, B_j and D_j are given by Equations (21), (22) and (23):

$$h(\lambda_j) = \kappa \tag{21}$$

$$B_j = \kappa^2\frac{\lambda_j^2 - 1}{(\lambda_j^2 + \kappa)^2} \tag{22}$$

$$D_j = \kappa\lambda_j^2\frac{\lambda_j^2 - 1}{(\lambda_j^2 + \kappa)^2} \tag{23}$$

From Equation (1), the behavior law is given by Equation (24) ($\lambda_1 = \lambda$; $\lambda_2 = \lambda_3 = \lambda^{-1}$; $\eta = N/2$):

$$\sigma_n = \frac{NkT}{2}\left(\lambda - \frac{1}{\lambda^2}\right) + \frac{NkT}{2}\sum_{j=1}^{3}\left(\frac{\partial B_j}{\partial\lambda} + \frac{\partial D_j}{\partial\lambda} - \frac{1}{1+B_j}\frac{\partial B_j}{\partial\lambda} - \frac{1}{1+D_j}\frac{\partial D_j}{\partial\lambda}\right) \tag{24}$$

This expression shows a unique corresponding generating function $\xi_1(\lambda)$.

Let us consider $\xi_1(\lambda) = \xi_{FE}(\lambda)$. Hence, $\xi_{FE}(\lambda)$ is given by Equation (25):

$$\xi_{FE}(\lambda) = \lambda - \frac{1}{\lambda^2} + \sum_{j=1}^{3}\left(\frac{\partial B_j}{\partial\lambda} + \frac{\partial D_j}{\partial\lambda} - \frac{1}{1+B_j}\frac{\partial B_j}{\partial\lambda} - \frac{1}{1+D_j}\frac{\partial D_j}{\partial\lambda}\right) \qquad (25)$$

4.2. Ordinary procedure for parameters identification

For the ordinary procedure, the base of approximation contains a unique generating function and is given by Equation (26):

$$\left\langle P(\lambda)\right\rangle = \left\langle \xi_{FE}(\lambda)\right\rangle \qquad (26)$$

As a result, the parameter NkT is given by Equation (27):

$$NkT = \frac{\sum_{k=1}^{M}\xi_{FE}(\lambda_k)\sigma_{nk}}{\sum_{k=1}^{M}\xi_{FE}^2(\lambda_k)} \qquad (27)$$

where (λ_k, σ_{nk}) are experimental data. The estimated parameters of the Flory-Erman model are recorded in Tables 3 and 4 and are compared to theoretical values (real values, from molecular considerations) [19, 20]. Figure 3 depicts the model prediction in comparison with Pak-Flory data. From this Figure, it emerges that the usual single procedure can be applied in this case; while in Figure 4, one sees that the single process is incongruous, the reasons are enumerated above.

Table 3. Estimated parameter *NkT* for the Flory-Erman model from Pak-Flory elastomer data ($\kappa = 3.58$)

Parameter NkT	Estimated value	Theoretical value [20] (Real value)
Simple Process (SP)	0.0660	0.06269
Multi-Stage Process (MSP)	0.0608	–

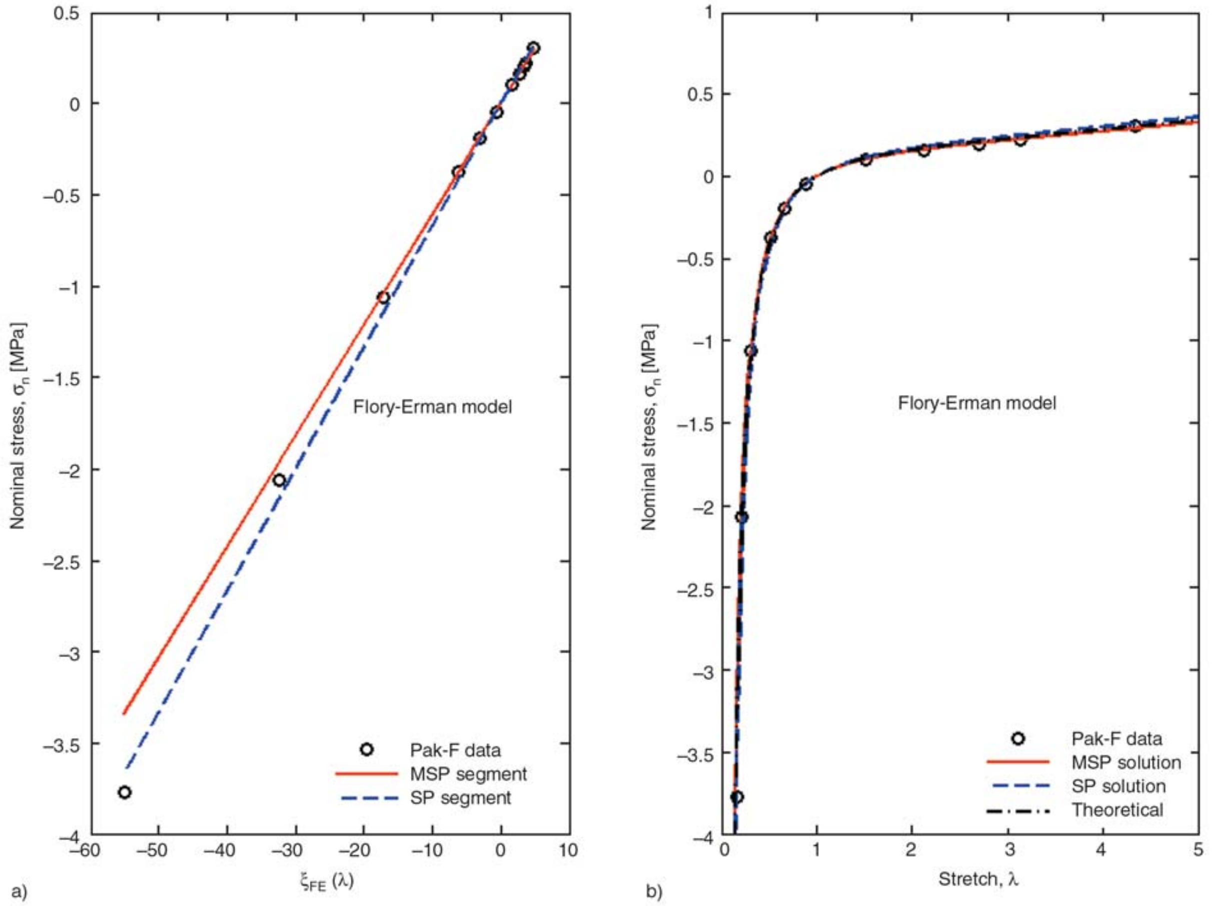

Figure 3. Validating and fitting the Flory-Erman model to Pak-Flory data. (a): validating domain of interest and parameters evaluation; (b): estimated compression-extension curves compared to data.

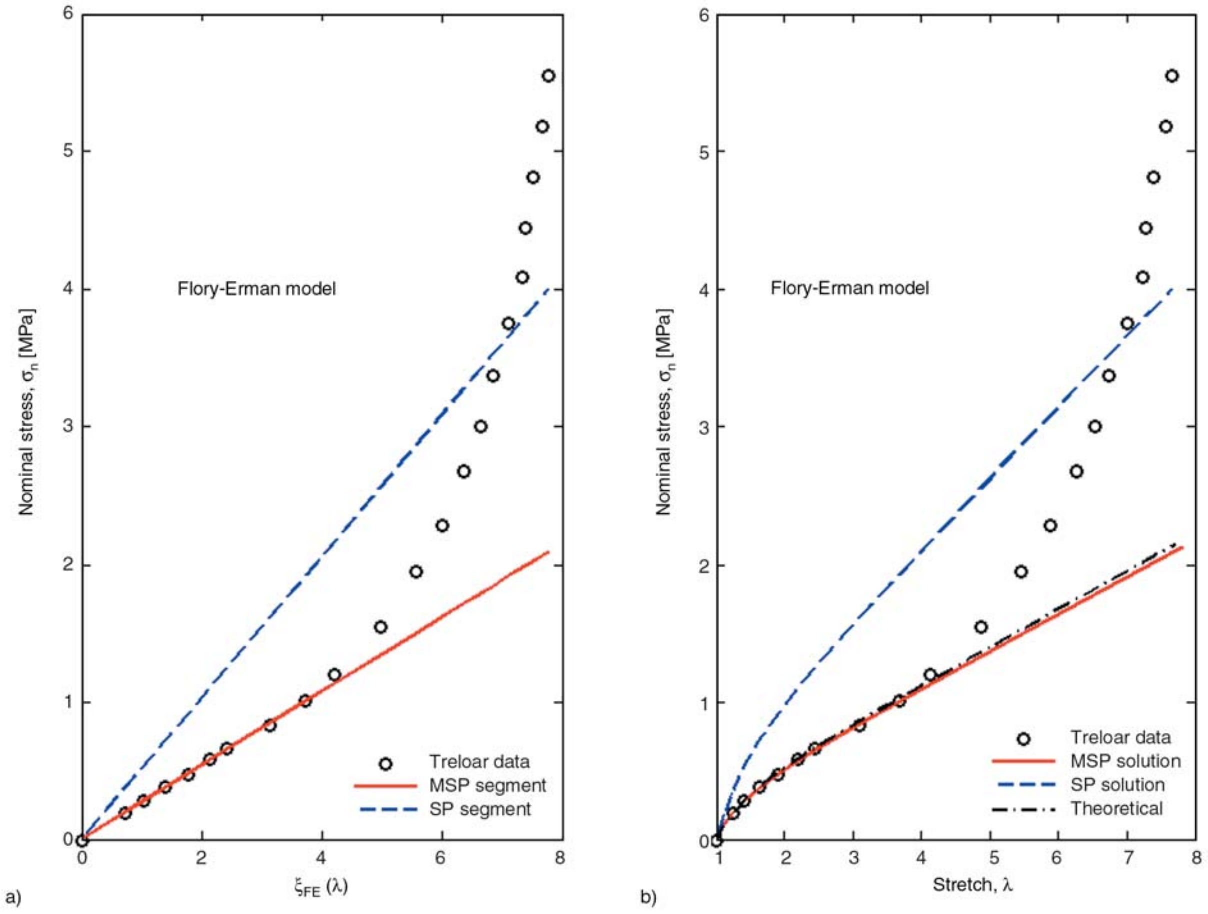

Figure 4. Validating and fitting the Flory-Erman model to Treloar data. (a): validating domain of interest and parameters evaluation; (b): estimated compression-extension curves compared to data.

Table 4. Estimated parameter *NkT* for the Flory-Erman model from Treloar rubber data ($\kappa = 0.68$)

Parameters NkT	Estimated value	Theoretical value [19] (Real value)
Simple Process (SP)	0.5151	0.55
Multi-Stage Process (MSP)	0.5382	–

4.3. Multi-stage procedure for identification

As previously seen, to evaluate parameters by the multi-stage procedure, one plots the reduced stress versus the generating function $\xi_{FE}(\lambda)$. It permits both the determination of the valid domain of the model, i.e., where the curve is linear; and the value of the parameter *NkT*, which is given by the gradient of the straight part of the curve, Figures 3a and 4a. Tables 3 and 4 show the estimated and the theoretical parameter values of the Flory-Erman model. A comparison of theoretical and estimated predictions of the model with data is illustrated in Figure 3b for Pak-Flory elastomer and in Figure 4b for Treloar rubber.

Let us note that the Gent-Thomas and the Flory-Erman models give similar results [21].

5. Complete models

This paper presents how to validate a partial model in general and that of Gent-Thomas in particular, because of difficulties when using the ordinary identification procedure. The complete modeling is not considered in this work.

Let us note that for a complete model such as that of Pucci-Saccomandi (also called Gent-Gent model) [22] given by Equation (28) or that of Beda (the extended Gent-Thomas model) [21] given by Equation (29), the ordinary as well as the multi-stage procedure remains appropriate for evaluating the parameters [9, 12, 13, 21]. The Gent-Gent model is given by Equation (28):

$$W_{PS} = K_2 \ln\frac{I_2}{3} - \frac{\mu}{2} J_m \ln\left(1 - \frac{I_1 - 3}{J_m}\right) \quad (28)$$

where $J_m = I_m - 3$; K_2 and μ are material parameters and I_m is the limiting value of the invariant I_1 to the deformation when the network is fully stretched.

The Beda (extended Gent-Thomas) model is given by Equation (29):

$$W_B = K_1(I_1-3) + K_2 \ln\frac{I_2}{3} + K_3(I_1-3)^{M-1} + K_4(I_1-3)^M \qquad (29)$$

where K_i are positive real numbers characteristic of material. The integer M (condition apply: $M \geq 3$) is the order of the model or material order [21].

Let us also note that the Pucci-Saccomandi (Gent-Gent) and Beda (extended Gent-Thomas) models give similar precise results [21].

6. Conclusions

A technique of validating partial hyperelastic models over a complete experimental range of deformation is set out. The Gent-Thomas model, an earlier and starting partial model, which successfully verifies experimental and theoretical requirements, but unfortunately not sufficiently exploited in hyperelastic modeling, can now be easily employed in rubber modeling and characterization. It comes out that the Gent-Thomas model is valid only under the stiffening deformation domain of rubber material.

References

[1] Mooney M.: A theory of large elastic deformation. Journal of Applied Physics, **11**, 582–592 (1940).

[2] Gent A. N., Thomas A. G.: Forms for the stored (strain) energy function for vulcanized rubber. Journal of Polymer Science, **28**, 625–637 (1958).

[3] Valanis R. C., Landel R. F.: The strain-energy function of a hyperelastic material in terms of the extension ratios. Journal of Applied Physics, **38**, 2997–3002 (1967).

[4] James A. G., Green A.: Strain energy function of rubber. II. The characterization of filled vulcanizates. Journal of Applied Polymer Science, **19**, 2319–2330 (1975).

[5] Ogden R. W.: Non-linear elastic deformations. Ellis Harwood, Chichester (1984).

[6] Lin D. C., Dimitriadis E. K., Horkay F.: Elasticity of rubber-like materials measured by AFM nanoindentation. Express Polymer Letters, **1**, 576–584 (2007).

[7] Yeoh O. H., Fleming P. D.: A new attempt to reconcile the statistical and phenomenological theories of rubber elasticity. Journal of Polymer Science, Part B: Polymer Physics, **35**, 1919–1931 (1997).

[8] Beda T.: Reconciling the fundamental phenomenological expression of the strain energy of rubber with established experimental facts. Journal of Polymer Science, Part B: Physics, **43**, 125–134 (2005).

[9] Ogden R. W., Saccomandi G., Sgura I.: Fitting hyperelastic models to experimental data. Computational Mechanics, **34**, 484–502 (2004).

[10] Rivlin R. S., Saunders D. W.: Large elastic deformation of isotropic materials. VII. Experiments of the deformation of rubber. Philosophical Transaction of the Royal Society, Series A: Mathematical and Physical Sciences, **243**, 251–288 (1951).

[11] Rivlin R. S.: Large elastic deformations. in 'Rheology: Theory and Applications' (ed.: Eirich F. R.) Academic Press, New York, 351–385 (1956).

[12] Beda T., Chevalier Y.: Non-linear approximation method by an approach in stages. Computational Mechanics, **32**, 177–184 (2003).

[13] Beda T.: Combining approach in stages with least squares for fits of data in hyperelasticity. Comptes Rendus Mecanique, **334**, 628–633 (2006).

[14] Pak H., Flory P. J.: Relationship of stress to uniaxial strain in crosslinked poly(dimethylsiloxane) over the full range from large compressions to high elongations. Journal of Polymer Science, Polymer Physics Edition, **17**, 1845–1854 (1979).

[15] Treloar L. R. G.: The physics of rubber elasticity. Oxford University Press, Oxford (1975).

[16] Johnson A. R., Quigley C. J., Mead J. L.: Large strain viscoelastic constitutive models for rubber, Part I: Formulations. Rubber Chemistry and Technology, **67**, 904–917 (1994).

[17] Erman B., Monnerie L.: Theory of elasticity of amorphous networks: Effect of constrains along chains. Macromolecules, **22**, 3342–3348 (1989). Correction: **25**, 4456 (1992).

[18] Flory P. J., Erman B.: Theory of elasticity of polymer networks, 3. Macromolecules, **15**, 800–806 (1982).

[19] Boyce M. C., Arruda E. M.: Constitutive models of rubber elasticity: A review. Rubber Chemistry and Technology, **73**, 504–523 (2000).

[20] Han W. H., Horkay F., McKenna G. B.: Mechanical and swelling behaviors of rubber: A comparison of some molecular models with experiment. Mathematics and Mechanics of Solids, **4**, 139–167 (1999).

[21] Beda T.: Modeling hyperelastic behavior of rubber: A novel invariant-based and a review of constitutive models. Journal of Polymer Science, Part B: Physics, **45**, 1713–1732 (2007).

[22] Pucci E., Saccomandi G.: A note on the Gent model for rubber-like materials. Rubber Chemistry and Technology, **75**, 839–851 (2002).

eXPRESS Polymer Letters Vol.2, No.9 (2008) 623–629
Available online at www.expresspolymlett.com
DOI: 10.3144/expresspolymlett.2008.75

Non-isothermal crystallization and melting of ethylene-vinyl acetate copolymers with different vinyl acetate contents

X. M. Shi, J. Zhang[*]*, J. Jin, S. J. Chen*

Department of Polymer Science and Engineering, College of Materials Science and Engineering, Nanjing University of Technology, Nanjing 210009, People's Republic of China

Received 25 May 2008; accepted in revised form 20 July 2008

Abstract. Non-isothermal crystallization and subsequent melting of three grades of ethylene-vinyl acetate copolymer were investigated by differential scanning calorimetry (DSC) technique. The DSC crystallization curves show that vinyl acetate (VAc) content has the same effect on the onset, peak and final crystallization temperatures, and these copolymers have almost the same spacing of thermal windows under identical crystallization condition. Subsequent melting DSC results suggest that EVA14 (14 wt% VAc) has the narrowest distribution of lamellar thickness and the most perfect crystals. Though the instantaneous nucleation was preferred, non-isothermal crystallization kinetics shows that EVA14 could form tridimensional crystallites, whereas EVA18 (18 wt% VAc) and EVA28 (28 wt% VAc) are prone to crystallize two-dimensionally, as a result of more noncrystallizable VAc co-monomers introduced in the crystallizable ethylene segments. The growth rate falls on the following sequence: EVA14>EVA18>EVA28. Moreover, the kinetic crystallizability G also well characterizes the variation of the non-isothermal crystallization of these EVA materials, in the view of structural impediment caused by the VAc content.

Keywords: *thermal properties, ethylene-vinyl acetate copolymer (EVA), crystallization and melting, crystallization kinetics*

1. Introduction

The crystallization and melting behavior of semicrystalline polymers has been studied for many years, but there is still much work to be done due to the differences in the molecular structure for different polymers. The reaction rate constant does not depend on temperature in case of isothermal measurement, while during non-isothermal experiment the value of rate constant depends on temperature. In these cases the results are less reliable, but the non-isothermal crystallization behavior is of more practical interest than isothermal behavior. This is because polymers are usually processed under nonisothermal cycles rather than under isothermal condition.

Ethylene-vinyl acetate copolymer (EVA) is a random copolymer synthesized from ethylene monomer and vinyl acetate (VAc) co-monomer. The copolymer is often produced by continuous bulk polymerization under high pressure similarly to low density polyethylene (LDPE) [1]. Its properties are easily variable by the adjustment of the comonomer ratio. When the VAc content is low, the copolymer is more akin to polyethylene and has enough ability to crystal, but for high VAc content the pendent acetoxy is excessive enough and prevents adjacent polyethylene chains packing into the crystal lattice [2], then totally amorphous and rubber-like EVA is expected when the VAc content is more than 43% by weight as indicated by Kamath and Wakefield [3]. It should be noticed that Varga

---

[*]Corresponding author, e-mail: zhangjun@njut.edu.cn

and his coworkers revealed that the crystallization and melting characteristics of PE are very sensitive to the VAc content [4].

In the present discussion, the non-isothermal crystallization kinetics for three different grades of EVA was investigated by differential scanning calorimetry (DSC) technique. The main objective for this work is to study the effect of VAc co-monomer content on the crystallization behavior of these copolymers. The non-isothermal DSC crystallization and melting curves of these copolymers were considered and the derived kinetic parameters were analyzed based on Avrami equation and its modified formulation. The kinetic crystallizability was also employed to evaluate the crystallization differences arising from the influence of VAc content on the EVA structure.

2. Experimental

2.1. Materials

Three grades of ethylene-co-vinyl acetate copolymer (EVA) with varying amounts of vinyl acetate (VAc) content are given in Table 1. EVA14 and EVA18 were supplied by Beijing Organic Chemical Plant, China; while EVA28 was supplied by Sumitomo Chemical Company, Japan. Generally, the VAc co-monomer can be considered to be randomly distributed along the copolymer chains.

2.2. Differential scanning calorimetry measurements

The non-isothermal crystallization and the following melting experiments of EVA samples with different VAc contents were carried out with a differential scanning calorimeter (DSC) instrument (model Pyris 1, PerkinElmer, USA). Details of samples as received were listed in Table 1. Samples weighing about 10 mg were cut off for the DSC. Argon purge gas with a flux of 20 ml/min was used to prevent thermal degradation of samples during the scanning. In order to remove the volatile impurities and erase the former thermal history, EVA samples were first heated up to150°C at a rapid heating rate of 20°C/min and kept at 150°C for 5 minutes. Then they were cooled down from 150 to 0°C at the rate of 5°C/min to obtain the non-isothermal crystallization curves. Finally, the remelting was finished by second heating run from 0 to 150°C at 10°C/min.

The crystallinity (X_c) of the samples was calculated according to Equation (1):

$$X_c = \frac{\Delta H_f}{\Delta H_f^*} \cdot 100\% \tag{1}$$

where ΔH_f^* is the enthalpy of fusion of the perfect polyethylene (PE) crystal and ΔH_f is the enthalpy of fusion of the EVA samples, respectively. The value of ΔH_f^* for PE is 277.1 J/g [5].

3. Results and discussion

3.1. Non-isothermal crystallization behavior

Figure 1 shows the non-isothermal crystallization DSC curves of the three grades of EVA. The corresponding values from the curves are collected in Table 2. As expected, DSC curves exhibit only one crystallization peak, and the crystallization peak

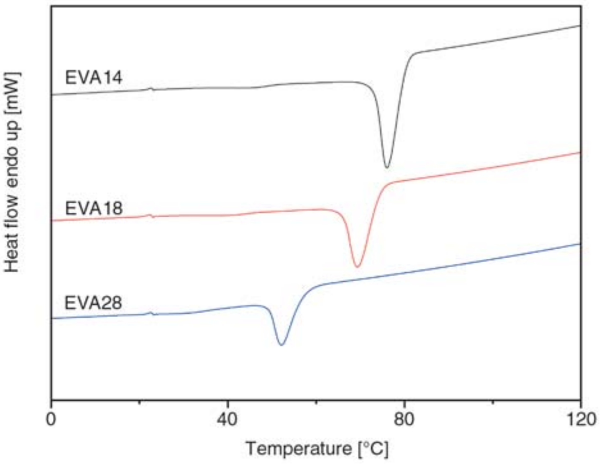

Figure 1. DSC curves of non-isothermal crystallization for the three EVA materials

Table 1. Details of EVA materials used

Grade	Nominal VAc [wt%]	Density [g/cm³]	Melt flow rate [g/10 min]	Nomenclature
14–2	14	0.940	2[a]	EVA14
18–3	18	0.935	3[a]	EVA18
KA-31	28	0.960	7[b]	EVA28

[a] ASTM D1238
[b] JIS K6924-2 1997

Table 2. DSC results of non-isothermal crystallization

EVA sample	T_c^{on} [°C]	T_c^p [°C]	T_c^f [°C]	ΔT [°C]	ΔH [J/g]
EVA14	80.4	76.1	73.4	7.0	36.5
EVA18	74.6	69.4	66.2	8.4	28.7
EVA28	57.1	52.2	49.5	7.6	17.0

T_c^{on}: onset crystallization temperature; T_c^p : peak crystallization temperature; T_c^f: final crystallization temperature; $\Delta T_c = T_c^{on} - T_c^f$; ΔH_c: enthalpy of crystallization

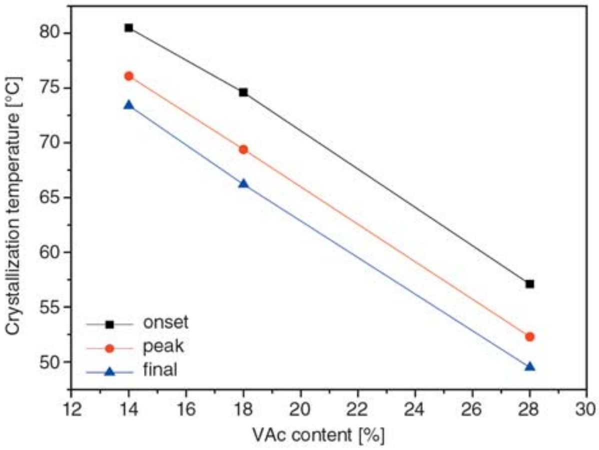

Figure 2. The relationships of crystallization temperatures and VAc content

shifts to lower temperature as the VAc content increases. This suggests that the VAc co-monomer reduces the stereoregularity of polyethylene macromolecular chain and the crystallization is restricted to certain degree. The same tendency of T_c^{on}, T_c^p and T_c^f is observed in Figure 2. It is interesting to notice that there are good linear relationships between these crystallization temperatures and the VAc content. The slopes of the onset, peak and final crystallization temperature against VAc content are parallel well with each other, indicating the same effect of VAc content on these crystallization temperatures. However, ΔT_c difference of these EVA materials is not so large as expected. All these EVA materials have a close ΔT_c value around 8°C. It could be inferred that these polymers have the same spacing of thermal windows under the same non-isothermal crystallization condition, independent of difference in VAc contents.

3.2. Subsequent melting behavior

To investigate the subsequent melting behavior of these EVA materials after the same non-isothermal crystallization condition, the melting curves were recorded in Figure 3. The characteristic data from the DSC curves are summarized in Table 3. Like the crystallization temperatures above, melting peak and final temperatures decrease accordingly with the increase in VAc content, indicating the lamellar thickness decrease since the melting temperature of a given sample decreases with decrease of lamellar thickness [6]. There is almost 20°C in peak melting temperature difference between EVA14 and EVA28. It is also apparent from the melting curves that the melting peak of EVA14 which has the lowest VAc content is the sharpest among the three EVA materials. It has been considered that the width of melting peak can reflect the distribution of the lamellar thickness [7]. Therefore, EVA14 has a narrower distribution of lamellar

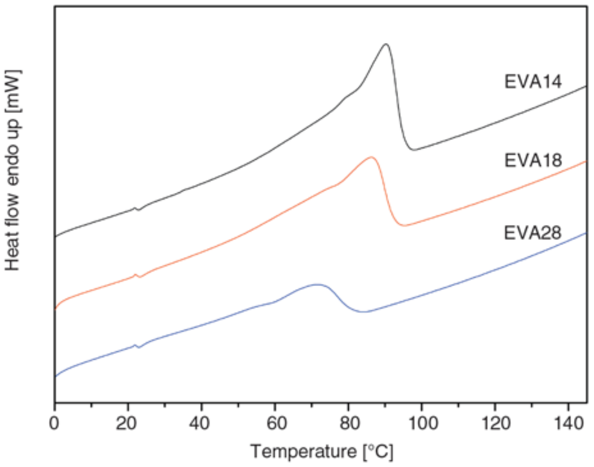

Figure 3. DSC curves of subsequent melting for the three EVA materials

Table 3. DSC results of subsequent melting

EVA sample	T_m^p [°C]	T_m^f [°C]	ΔH_f [J/g]	X_c [%]
EVA14	90.2	95.2	63.9	23.1
EVA18	86.0	92.5	50.6	18.3
EVA28	70.5	81.6	21.8	7.9

T_m^p : peak melting temperature; T_m^f: final melting temperature; ΔH_f: enthalpy of melting; X_c: crystallinity thickness than that of EVA18 and EVA28. Similarly, the crystallinity confirms the difference of the crystal perfection of these copolymers. The crystallinity of EVA28 is only 7.9% which is no more than 45% of EVA18 or no more than 35% of EVA14. It is worth noting that the onset melting temperatures of these copolymers are difficult to discern because of broad melting range, indicating all of these EVA materials have a wide size distribution of the crystallites. All the results above can be explained based on the amount of total non-crystallizable, intra-molecular defects [7] (i.e. VAc defects). The EVA material with high VAc content should have high amount of the VAc defects, and tend to crystallize imperfectly.

3.3. Non-isothermal crystallization kinetics

Crystallization kinetics of a material can be analyzed by evaluating the extent or degree of phase transformation which is often denoted as X_t. The relative crystallinity X_t as a function of time or temperature by recording the heat flow during crystallization process and is defined as Equation (2) [8, 9]:

$$X_t = \frac{\int_{T_0}^{T} H(T)\mathrm{d}T}{\int_{T_0}^{T_\infty} H(T)\mathrm{d}T} \cdot 100\,\% \qquad (2)$$

where T_0 and T_∞ are the initial and end crystallization temperature, respectively, and $H(T)$ is the heat flow at temperature T. X_t is determined from the crystallization curve by integral method.

The relative crystallinity is plotted versus different crystallization temperatures and time as is shown in Figures 4 and 5. At the same cooling rate of 5°C/min, development curves for the relative crystallinity of these EVA materials display the same reversed *S* type as the crystallization temperature goes down, whereas the curves display the similar *S* type as the crystallization time elapses. Though the three grades of EVA possess different VAc content, the whole crystallization process of these polymers is a similar packing work of the crystallizable ethylene segments between uncrystallizable vinyl acetate segments. So these EVA materials undoubtedly display similar development curves with crystallization temperature or time.

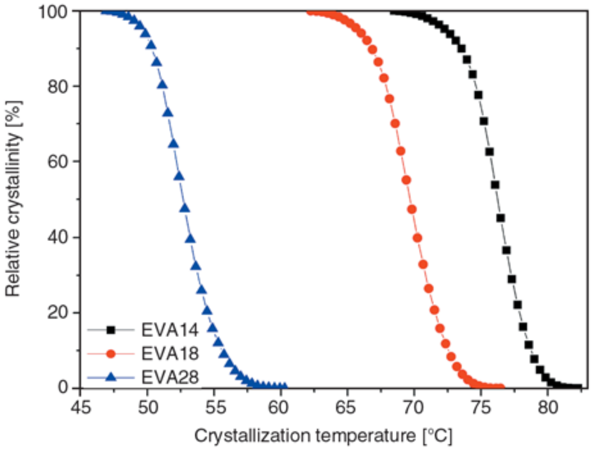

Figure 4. Plots of relative crystallinity vs. crystallization temperature for the three EVA materials

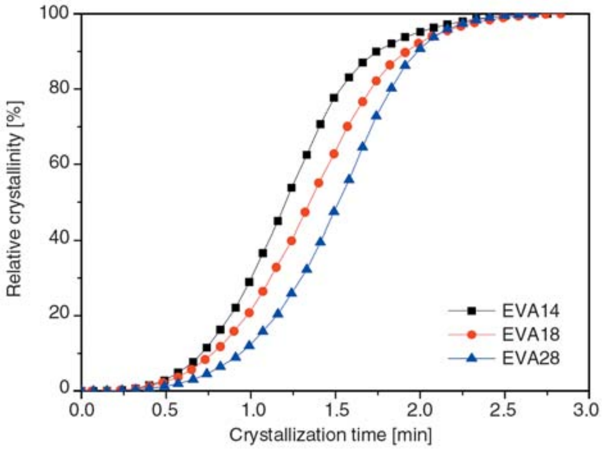

Figure 5. Plots of relative crystallinity vs. crystallization time for the three EVA materials

Majority of the proposed formulations for predicting non-isothermal crystallization kinetics are based on the modification of Avrami equation. Avrami equation for non-isothermal crystallization is expressed by Equation (3) [10–12]:

$$1 - X_t = \exp(-Zt^n) \qquad (3)$$

where the exponent n is a mechanism constant which value depends on the type of nucleation and the growth dimension, and the parameter Z is a growth rate constant involving both nucleation and growth rate parameters [13].

The kinetics parameters of non-isothermal crystallization were determined, based on the assumptions that non-isothermal crystallization may be treated as a sequence of isothermal crystallization steps

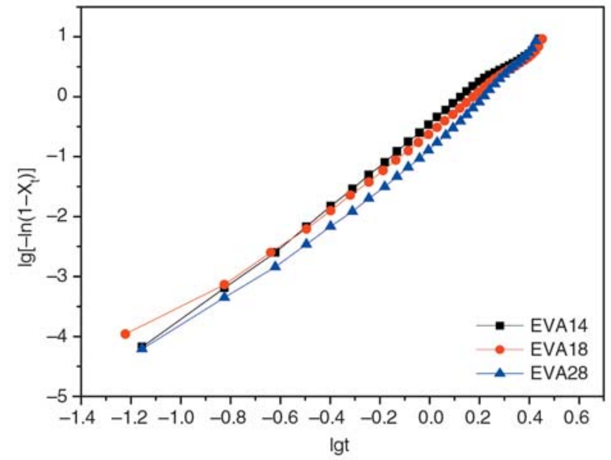

Figure 6. Plots of lg[–ln(1-X_t)] vs. lg$t$ for the three EVA materials

[14, 15]. In this case, Equation (3) can be transformed into Equation (4):

$$\lg[-\ln(1-X_t)] = \lg Z + n\lg t \tag{4}$$

Figure 6 gives the plots of lg[–ln(1–X_t)] versus lg$t$, they show relatively good linear relationship (the correlation coefficient for linear regression, R>0.98 for all these curves). However, all the three straight lines terminate with an upward tail, which is considered as the secondary crystallization as observed in other polymers [16–18]. The Avrami exponent n and constant Z can be obtained from the slope and the intercept of the plot of lg[–ln(1–X_t)] against lg$t$. Considering the non-isothermal character of the process investigated, the growth rate constant is corrected by the cooling rate ϕ, then the final form of growth rate constant Z_c is obtained from Equation (5) [14]:

$$\lg Z_c = \frac{\lg Z}{\phi} \tag{5}$$

where n and Z_c values are listed in Table 4. It is found that the Avrami exponent of EVA14 is between 3 and 4, whereas the Avrami exponents of EVA18 and EVA28 are around 3. It seems that there may be differences in the nucleation and growth mechanisms of these EVA materials. EVA14 could form coexistent tridimensional crystallites from instantaneous and sporadic nucleation (n = 3.33). In the case of EVA18 and EVA28, the Avrami exponents imply two possibilities: the two EVA materials may form tridimensional crystallites from sporadic nucleation; or they probably form two-dimensionally growing crystallites from instantaneous nucleation [19, 20]. Since no other heterogeneous material was introduced, the instantaneous nucleation was preferred for the crystallization of the three EVA materials. Consequently, EVA14 is prone to form tridimensional crystallites as polyethylene material often does, whereas EVA18 and EVA28 are forced to crystallize in two-dimensional caused by the impediment of more acetoxy side chains. In addition, the lowest half crystallization time ($t_{0.5}$) of EVA14 indicate the relative fast crystallization compared with EVA18 and EVA28. The same conclusion can also be drawn from the comparison of the growth rate constant Z_c.

To characterize the kinetics of non-isothermal crystallization of PET, Jeziorny [14] used a parameter G, known as 'the kinetic crystallizability'. It characterizes the degree of transformation obtained over the entire crystallization range (T_m, T_g) with unit cooling rate. The calculation of the parameter is done by Equation (6):

$$G = \left(\frac{\pi}{\ln 2}\right)^{\frac{1}{2}} \frac{\int_{t_0}^{t_{\max}} H_t \mathrm{d}t}{\int_{t_{\max}}^{t_f} H_t \mathrm{d}t} \frac{1}{t_{\max}} \frac{D}{2} \tag{6}$$

where t_0, t_{max}, t_f are the time corresponding to T_c^{on}, T_c^p and T_c^f, respectively; D is the half width of the crystallization curve.

This parameter, like the growth rate constant Z above, requires proper correction. The final form of this parameter is shown in Equation (7):

$$G_c = \frac{G}{\phi} \tag{7}$$

Table 4. Parameters for the non-isothermal crystallization of the three EVA materials

EVA sample	n	$t_{0.5}$ [min]	Z_c [min^{-n}]	G_c
EVA14	3.33	1.20	0.80	1.697
EVA18	2.96	1.35	0.77	1.659
EVA28	2.96	1.53	0.72	1.559

G_c values of these EVA materials are listed in Table 4. It is quite evident that the G_c value decreases with an increase in VAc content. Jeziorny [14] recommended G_c for characterizing the kinetics of non-isothermal crystallization, because this parameter aims at the determination of quantitative relations between the kinetics of polymer crystallization and the structural features. From the data in Table 4, it is found that the G_c value of EVA18 is very close to that of EVA14, and the G_c value of EVA28 is relatively low due to the high VAc content compared with the other two grades of EVA. It has been reported that the increase in the amount of total co-monomer in EAA or E-MA-AA will enhance the energy barrier for crystallizable segments to crystallize [7]. Since the increase in the amount of the randomly distributed VAc co-monomer will result in a decrease in both the number and length of the crystallizable ethylene segment, the EVA28 material which has the most VAc content should have the biggest energy barrier for the ethylene segments to overcome. This is also consistent with the fact that bulky nature of the acetoxy side chain will reduce the ability of the polymer chains to pack closely together to form crystallites [1]. It can be thought from the results above that the VAc content undoubtedly has a negative effect on the crystal growth of EVA material as a result of the strong dependence of the copolymer structure on the VAc co-monomer.

4. Conclusions

The non-isothermal crystallization for the three grades of EVA materials indicates that the crystallization tendency of EVA decreases with increasing of VAc content. VAc content has the same effect on the onset, peak and final crystallization temperatures. And with increasing of VAc content, perfection of EVA crystals decreases.

In addition, the results of non-thermal crystallization kinetics show that the simplified assumption of a sequence of isothermal crystallization is suitable for characterizing the non-isothermal crystallization of these EVA materials. Though the instantaneous nucleation was preferred, there is difference for the growth of these EVA materials. EVA14 could form tridimensional crystallites whereas EVA18 and EVA28 are prone to crystallize in two-dimensional as a result of more noncrystallizable VAc co-monomers introduced in the crystallizable ethylene segments. The growth rate falls on the following sequence: EVA14>EVA18>EVA28. The kinetic crystallizability G also well characterizes the difference of the non-isothermal crystallization of these EVA materials, in the view of structural impediment caused by the VAc content.

References

[1] Whelan A., Lee K. S.: Developments in rubber technology, 3. Thermoplastic rubbers. Applied Science Publishers, London (1982).

[2] Henderson A. M.: Ethylene-vinyl acetate (EVA) copolymers: A general review. IEEE Electrical Insulation Magazine, **9**, 30–38 (1993).

[3] Kamath P. M., Wakefield R. W.: Crystallinity of ethylene-vinyl acetate copolymers. Journal of Applied Polymer Science, **9**, 3153–3160 (1965).

[4] Varga J., Menczel J., Solti A.: The melting of high-pressure polyethylene subjected to stepwise heat treatment. Journal of Thermal Analysis and Calorimetry, **17**, 333–342 (1979).

[5] Brandrup J., Immergut E. H., Grulke E. A.: Polymer handbook. Wiley-Interscience, New York (1999).

[6] Wunderlich B.: Macromolecular physics. Academic Press, New York (1976).

[7] Somrang N., Nithitanakul M., Grady B. P., Supaphol P.: Non-isothermal melt crystallization kinetics for ethylene-acrylic acid copolymers and ethylene-methyl acrylate-acrylic acid terpolymers. European Polymer Journal, **40**, 829–838 (2004).

[8] Bhattarai N., Kim H. Y., Cha D. I., Lee D. R., Yoo D. I.: Nonisothermal crystallization and melting behavior of the copolymer derived from *p*-dioxanone and poly(ethylene glycol). European Polymer Journal, **39**, 1365–1375 (2003).

[9] Mya K. Y., Pramoda K. P., He C. B.: Crystallization behavior of star-shaped poly(ethylene oxide) with cubic silsesquioxane (CSSQ) core. Polymer, **47**, 5035–5043 (2006).

[10] Avrami M.: Kinetics of phase change I. General theory. Journal of Chemical Physics, **7**, 1103–1112 (1939).

[11] Avrami M.: Kinetics of phase change, II. Transformation-time relations for random distribution of nuclei. Journal of Chemical Physics, **8**, 212–224 (1940).

[12] Xiong H., Gao Y., Li H. M.: Non-isothermal crystallization kinetics of syndiotactic polystyrene-polystyrene functionalized SWNTs nanocomposites. Express Polymer Letters, **1**, 416–426 (2007).

[13] Kong X., Yang X., Zhou E., Ma D.: Nonisothermal crystallization kinetics of ethylene terephthalate-ethylene oxide segmented copolymers with two crystallizing segments. European Polymer Journal, **36**, 1085–1090 (2000).

[14] Jeziorny A.: Parameters characterizing the kinetics of the non-isothermal crystallization of poly(ethylene terephthalate) determined by DSC. Polymer, **19**, 1142–1144 (1978).

[15] Kalam M. R., Chu E.: Isothermal and nonisothermal crystallization of polyethylene. Polymer Engineering and Science, **23**, 27–31 (1983).

[16] Liu T. X., Mo Z., Wang S. G., Zhang H.: Nonisothermal melt and cold crystallization kinetics of poly(aryl ether ether ketone ketone). Polymer Engineering and Science, **37**, 568–575 (1997).

[17] Run M. T., Yao C. G., Wang Y. J.: Morphology, isothermal and non-isothermal crystallization kinetics of poly(methylene terephthalate). European Polymer Journal, **42**, 655–662 (2006).

[18] Maa Y-L., Hu G-S., Ren X-L., Wang B-B.: Non-isothermal crystallization kinetics and melting behaviors of nylon 11/tetrapod-shaped ZnO whisker (T-ZnOw) composites. Materials Science and Engineering, Part A: Structural Materials Properties Microstructure and Processing, **460–461**, 611–618 (2007).

[19] Gupta A. K., Rana S. K., Deopura B. L.: Crystallization kinetics of high-density polyethylene/linear low-density polyethylene blend. Journal of Applied Polymer Science, **51**, 231–239 (1994).

[20] Xu X., Xu J., Chen L., Liu R., Feng L.: Nonisothermal crystallization kinetics of ethylene-butene copolymer/low-density polyethylene blends. Journal of Applied Polymer Science, **80**, 123–129 (2001).

eXPRESS Polymer Letters Vol.2, No.9 (2008) 630–638
Available online at www.expresspolymlett.com
DOI: 10.3144/expresspolymlett.2008.76

Studies of structural, thermal and electrical behavior of polymer nanocomposite electrolytes

Dillip K. Pradhan, R. N. P. Choudhary, B. K. Samantaray*

Department of Physics and Meteorology, Indian Institute of Technology, Kahargapur-721302, India

Received 19 June 2008; accepted in revised form 27 July 2008

Abstract. Structural, thermal and electrical behavior of polymer-clay nanocomposite electrolytes consisting of polymer (polyethylene oxide (PEO)) and NaI as salt with different concentrations of organically modified Na^+ montmorillonite (DMMT) filler have been investigated. The formation of nanocomposites and changes in the structural properties of the materials were investigated by X-ray diffraction (XRD) analysis. Complex impedance analysis shows the existence of bulk and material-electrode interface properties of the composites. The relative dielectric constant (ε_r) decreases with increase in frequency in the low frequency region whereas frequency independent behavior is observed in the high frequency region. The electrical modulus representation shows a loss feature in the imaginary component. The relaxation associated with this feature shows a stretched exponential decay. Studies of frequency dependence of dielectric and modulus formalism suggest that the ionic and polymer segmental motion are strongly coupled manifeasting as peak in the modulus (M'') spectra with no corresponding feature in dielectric spectra. The frequency dependence of ac (alternating current) conductivity obeys Jonscher power law feature in the high frequency region, where as the low frequency dispersion indicating the presence of electrode polarization effect in the materials.

***Keywords:** nanocomposites, X-ray diffraction, ac conductivity, conductivity relaxation*

1. Introduction

The combination of clay and functional polymers interacting at atomic level constitute the basis for preparing an important class of inorganic-organic nanostructured materials i.e., polymer nanocomposites [1, 2]. Among these nanocomposites, the intercalation of electroactive species into the interlayer spacing of 2:1 phyllosilicate (such as montmorillonite, hectorite, laponite etc.) is a method to construct a novel hybrid supermolecular assembly with particular electrical behavior [1–5]. Intercalation of polymers, in principle, leads to the formation of new materials, which combine the optical and electrical properties of the polymer with mechanical strength, thermal stability etc. of the inorganic host and so possesses properties which may not be achieved by either component separately. Solid polymer electrolytes (SPEs) formed by complexing alkali metal salts with polyethers such as polyethylene oxide (PEO) have widely been studied for potential applications in solid state batteries and other electrochemical devices [6–8]. They are also of fundamental interest because of their unusual mechanism of ionic transport, which they exhibit and for which a detailed understanding is still lacking [8]. It is now well established that significant ionic motion occurs only in the elastomeric amorphous phase of the polymer and is closely associated with the segmental motion of polymers [8]. Measurement and analysis of SPEs are complicated by various factors. First these materials are often heterogeneous with both amorphous and crystalline regions and the distribution of salt concentration may vary throughout the poly-

---

*Corresponding author, e-mail: crnpfl@phy.iitkgp.ernet.in mer electrolyte [9]. Second at certain salt concentrations (where significant coupling occurs), there is an anionic contribution to the conductivity [10]. Moreover because of the low dielectric constant of PEO, polymer mediated cation anion pair formation is unavoidable [11]. The intercalated polymer nanocomposite electrolytes (PNCEs) are attractive because the bulky anions cannot enter into the nanometric gallery of the layered silicate (such as montmorillonite, hectorite, laponite etc.), whereas the polymer and cation can enter into that nanometric channel of the clay. Hence the formation of cation anion pair and dual ionic conduction are expected to be minimum. These PNCEs, in principle, therefore provide the opportunity to investigate conductivity and associated relaxation in polymer electrolyte free from previously mentioned problems. We have used here montmorillonite (MMT) clay as inorganic filler, which possesses intercalation property. The filler is organically modified with dodecyl amine so that the hydrophilic nature of the silicate layer is changed into hydrophobic, and the interlayer spacing expands. Indeed this creates appropriate environment for the intercalation of polymer chains between clay layers [12]. Though there has been a considerable amount of work performed on synthesis and characterization of PNCEs (polymer-layered silicate nanocomposite electrolytes) by various research groups [1–5, 12, 13], not much work has been reported on dielectric and electrical properties of PNCEs as yet.

In view of the above, the present paper aims to report structural, thermal and electrical behavior of an ionicallly conducting polymer nanocomposites system: $(PEO)_{25}$-NaI + x wt% DMMT with different values of x. The effect of DMMT (i.e., dodecyl amine modified MMT) concentration on electrical and ac conductivity response has been investigated in order to gain better understanding of ion transport behavior in PNCEs.

2. Experimental details

Polymer-clay nanocomposite electrolytes [$(PEO)_{25}$-NaI + x wt% DMMT (x = 0,5, 10, 15, 20, 30, 50)] consist of polymer, polyethylene oxide (PEO) with molecular weight of $6\cdot10^5$ (M/S Aldrich, USA) and NaI (M/S Merck India Ltd, Mumbai, India) as salt with different concentrations of DMMT (MMT supplied by University of Missouri, Coulambia, USA) have been synthesized by a tape casting technique using the self designed tape caster. The PEO and sodium salt molar ratio was maintained at 25:1 (i.e., $(PEO)_{25}$-NaI). It means that the there is sufficient number of available sites (i.e., the oxygen atoms in PEO) for Na-ion to hop from one site to another one. Detailed preparation and characterization methods for similar type of systems have already been reported [14, 15]. The X-ray diffraction pattern of the PNCEs films was recorded at room temperature using an X-ray powder diffractometer (Rigaku Miniflex) with CuK_α radiation (λ = 0.15405 nm) in 2θ (Bragg angles) range ($2°\leq2\theta\leq10°$) at a scan speed of 0.5°/min. Thermogravimetric (TG) analysis was performed using a SHIMADZU thermogravimetric analyzer. Samples were heated in a platinum pan from room temperature to 600°C at a heating rate of 10°C/min under nitrogen atmosphere. An analysis of the electrical behavior of PNCE films was carried out using impedance spectroscopy on the application of a small ac signal (100 mV) across the symmetrical cell of the type SS||PNCE||SS (where SS stands for stainless steel blocking electrodes). Complex impedance parameters (i.e., impedance, phase angles, permittivity and tangent loss parameters) were obtained by a computer-controlled impedance analyzer (HIOKI LCR Hi-Tester, Model:3532, Japan) as a function of frequency (100 Hz to 1 MHz) at different temperatures (30 to 150°C). The ac conductivity was evaluated from dielectric data in accordance with the relation: $\sigma_{ac} = \omega\,\varepsilon_0\,\varepsilon_r \tan\delta$ where $\varepsilon_r = C/C_0$ is the relative permittivity, $\tan\delta$ = loss tangent, C_0 = vacuum capacitance of the cell. The real and imaginary parts of impedance, permittivity and electric modulus were calculated using Equations (1)–(5):

$$Z^* = Z' - jZ'' \tag{1}$$

$$\varepsilon^* = \varepsilon' - j\varepsilon'' \tag{2}$$

where

$$\varepsilon' = \frac{-Z''}{\omega C_0 (Z'^2 + Z''^2)} \tag{3}$$

$$\varepsilon'' = \frac{Z'}{\omega C_0 (Z'^2 + Z''^2)} \tag{4}$$

and

$$M^* = M' + jM'' = \frac{1}{\varepsilon^*} = j\omega\varepsilon_0 Z^* \qquad (5)$$

3. Results and discussion

3.1. X-ray diffraction

XRD studies have been carried out in order to monitor the formation of the nanocomposites. Figure 1 shows the XRD patterns of Na$^+$-MMT, DMMT and (PEO)$_{25}$-NaI +x wt% DMMT for different values of x at room temperature in the range of 3–10°. The peaks were assigned to the 001 basal reflection of DMMT. It is observed that Na$^+$-MMT exhibits (001) reflection peak at an angle (2θ = 7.27°) corresponding to the interlayer spacing (d_{001}) 1.215 nm. Upon modification with dodecyl amine, the peak shifts toward the lower angle side corresponding to interlayer spacing of 1.568 nm, indicating the successful intercalation of alklyl ammonium ion into the gallery of MMT. When DMMT is added to polymer salt complex, there is an increase in the d_{001} (i.e., the peak position of (001) plane shift towards the lower angle side), which indicates that there is an increase in the gallery height. This suggests the successful intercalation of polymer-salt complex into the nanometric gallery of the DMMT confirming the formation of nanocomposites [16].

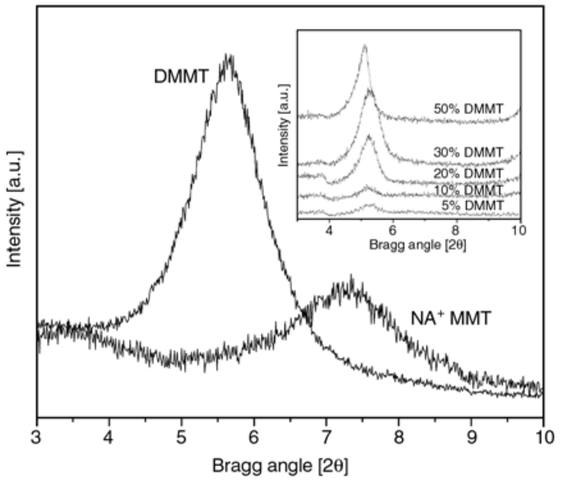

Figure 1. Comparison of XRD patterns of Na$^+$-MMT, DMMT and (PEO)$_{25}$-NaI + x wt% DMMT with different concentrations of DMMT (x)

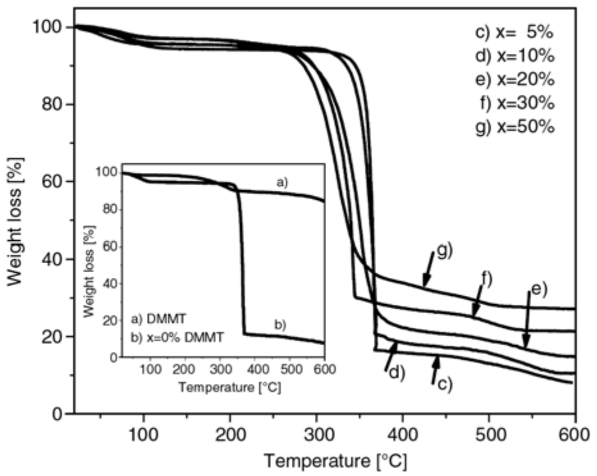

Figure 2. TGA thermograms of DMMT (a) and PNCEs films of (PEO)$_{25}$-NaI + x wt% of DMMT with different values of x, i.e., x = 0% (b), x = 5% (c), x = 10% (d), x = 20% (e), x = 30% (f) and x = 50% (g)

3.2. Thermogravimetric analysis

Figure 2 shows the TGA curves of (PEO)$_{25}$-NaI + x wt% of DMMT with different value of x. For both, the polymer-salt complexes and PNCEs, a small amount of mass loss at low temperatures (T<125°C) is assigned to elimination of water or residual solvent (if any). For x = 0 (i.e., polymer-salt complex), a sharp mass loss occurs corresponding to the decomposition of PEO after the elimination of water. It has been established [17] that the volatile evolution of both PEO and polymer-salt complexes occurs in a single step after elimination of water, while the complex leaves a residual quantity above 500°C. In addition to this sharp weight loss, another broad weight loss occurs at higher temperatures for PNCEs. It is generally assumed [18], that in intercalated PNCEs materials, some PEO chains reside inside the gallery and others outside the gallery. So the sharp weight loss is expected due to the PEO chains residing outside the gallery. The broad loss (at higher temperatures) is attributed to the decomposition of PEO inside the gallery since no weight loss for DMMT is observed in the same temperature range. PEO chains inside the silicate gallery are responsible for broader weight loss, as the degradation products need more temperature to depart from the silicate gallery. From the Figure 2, it is observed that on addition of small amount of clay the (residual) weight loss increases because of the restriction of thermal motion of the polymer in the silicate layer. Again, the residual weight loss increases on increasing DMMT concentration.

3.3. Complex impedance spectroscopy

Figure 3 represents the complex impedance spectrum/Nyquist plot (Z'' vs. Z') of PNCE films of $(PEO)_{25}$-NaI + x wt% of DMMT for various clay concentrations (x) at room temperature. The typical Nyquist plot of the samples comprises of a broadened semicircle in the high frequency region followed by a tail (spike) in the lower frequency region. The higher frequency semicircle can be ascribed mainly to the bulk properties of the materials, where as the low frequency spike indicates the presence of double layer capacitance at the electrode/sampleinterface [19]. The intercept of the semicircle with the real axis (Z') at low frequency (end) give rise to the bulk (ionic) resistance (R_b) of the materials.

Figure 4 shows the temperature dependence of impedance spectra of (a) $(PEO)_{25}$-NaI and (b) $(PEO)_{25}$-NaI + 5 wt% DMMT as a representative plot. It is clear that the diameter of the semicircle of high frequency region decreases with rise in temperature, and finally it vanishes above 60°C, leaving only a spike in the spectrum. The presence of semicircle signifies the persistence of capacitance associated with the heterogeneity textures of the composites. The polymer electrolytes are heterogeneous due to the presence of both amorphous and crystalline regions. The disappearance of the semicircle indicates the homogeneity of the system, which agrees well with the reported one [20]. The change in the diameter of semicircle indicates that R_b decreases with increase of temperature. On the other hand, the slope of the straight line (due to material electrode interface) does not vary significantly with temperature, which indicates that no electrochemical degradation of the electrodes occurs during the conductivity measurement. Similar type of explanation has been reported elsewhere [21] in many other systems.

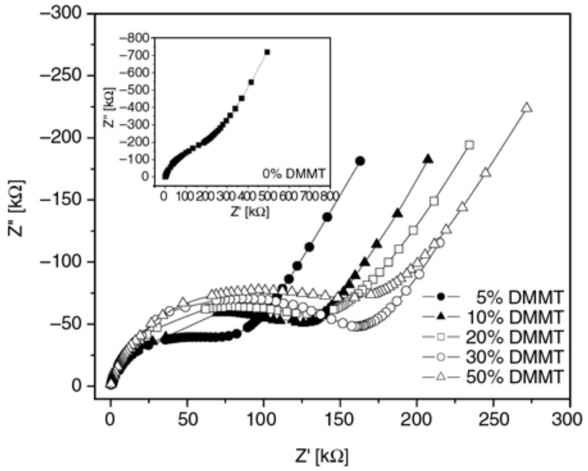

Figure 3. Variation of imaginary (Z'') with real (Z') part of impedance of $(PEO)_{25}$–NaI + x wt% of DMMT with different concentrations (x) of DMMT at room temperature (30°C)

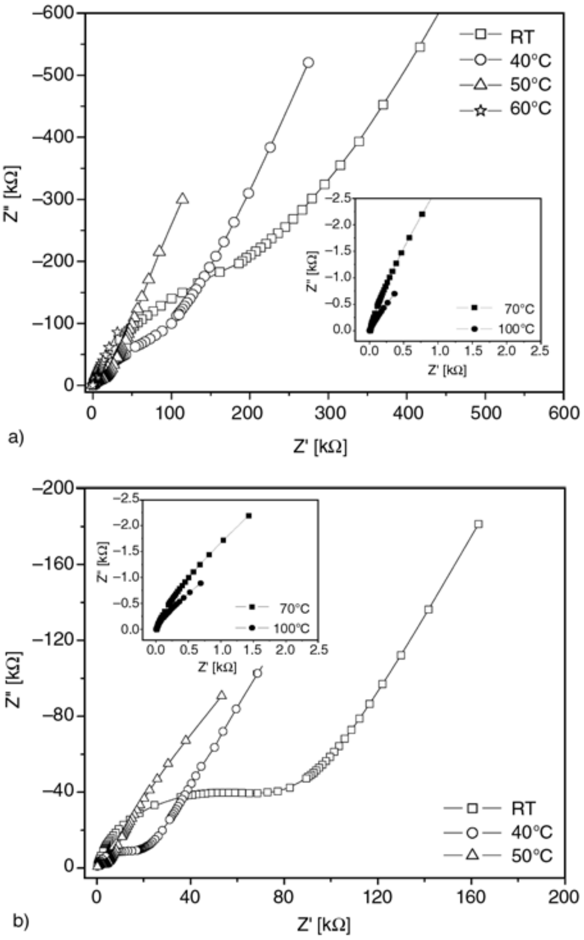

Figure 4. Complex impedance spectrum of (a) $(PEO)_{25}$-NaI and (b) $(PEO)_{25}$-NaI + 5 wt% DMMT as representative at different temperatures

3.4. Dielectric properties

Figure 5 shows the variation of relative dielectric constant (ε_r) with frequency of the PNCE films with varying DMMT concentration at room temperature. In all cases, a strong frequency dispersion of permittivity was observed in the low frequency region followed by a nearly frequency independent behavior above 5 kHz. The decrease of ε_r with increase in frequency is attributed to the electrical relaxation processes, but at the same time the material electrode polarization cannot be ignored, as our samples are ionic conductors. It has been observed

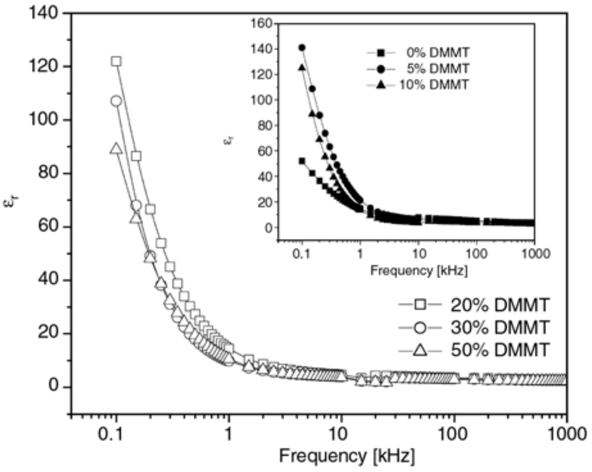

Figure 5. Variation of relative dielectric constant (ε_r) of PNCEs with frequency for different concentrations of DMMT of $(PEO)_{25}$-NaI + x wt% DMMT at room temperature (30°C)

that the relative permittivity of PNCEs is higher than that of the polymer-salt complex, and the maximum value is found for 5% clay concentration. The enhancement of dielectric properties may be due to the following reasons. The large scale heterogeneity in polymer salt complex is suppressed in the nanocomposite, and is replaced by small scale heterogeneity. The small scale heterogeneity is connected to the presence of silicate layer, which increases the free volume, due to looser segmental packing in chains confined to nanovolume [22].

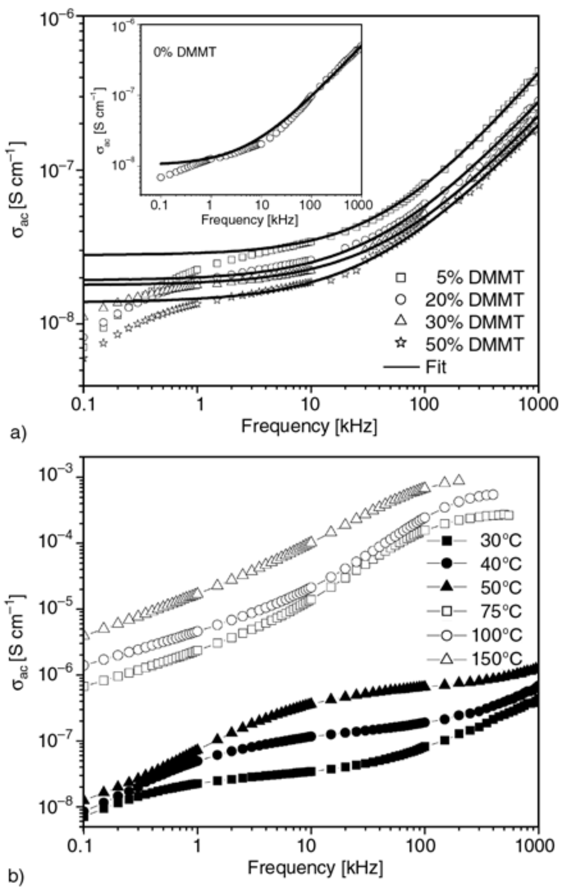

Figure 6. Comparison of frequency dependent ac conductivity of $(PEO)_{25}$-NaI + x wt% DMMT for (a) different values of x at room temperature (30°C); (b) for x = 5% at different temperatures. The continuous solid line represents the fit of experimental to the power law $\sigma(\omega) = \sigma_0 + A\omega^n$.

3.5. AC conductivity

The frequency dependent ac conductivity of $(PEO)_{25}$-NaI + x wt% DMMT for (a) different values of x at room temperature (30°C) and (b) for x = 5% for different temperatures is shown in Figure 6. The ac conductivity patterns show a frequency independent plateau in the low frequency region and exhibits dispersion at higher frequencies. This behavior obeys the universal power law [23, 24], $\sigma(\omega) = \sigma_0 + A\omega^n$, where σ_0 is the *dc* conductivity (frequency independent plateau in the low frequency region), A is the pre-exponential factor and n is the fractional exponent between 0 and 1 (the solid line is the fit to the expression). The effect of electrode polarization is evidenced by small deviation from σ_{dc} (plateau region) value in the conductivity spectrum (in the low frequency region). With rise in temperatures, the low frequency electrode polarization phenomena become more prominent and thus plateau region shifts to higher frequency side (Figure 6b). The values of σ_0, A and n obtained by fitting the universal power law are given in Table 1 (for Figure 6a). Generally, for ionic conductors, power law exponents can be between 1 and 0.5 indicating the ideal long-range pathways and diffusion limited hopping (tortuous pathway) respectively [25]. The value of exponent (Table 1) of the higher frequency slopes shows that the long-range drift of ions may be one of the main reasons of ionic conduction [25] in the system. It has been observed that (Table 1) the maximum value of conductivity was found to be $2.8 \cdot 10^{-8}$ S·cm^{-1} for 5% DMMT concentration whereas for higher DMMT concentration the conductivity decreases monotonically (room temperature). This observation can be explained by an empirical Equation (6):

$$\sigma = \sum n_i \mu_i z_i \tag{6}$$

Table 1. Comparison of parameters obtained from fit to the experimental data to $\sigma(\omega) = \sigma_0 + A\omega^n$ and $\Phi = \Phi_0 \exp[(-t/\tau)^\beta]$ functions respectively of $(PEO)_{25}$-NaI $+x$ wt% DMMT, for different DMMT concentration (x) at room temperature

x [%]	σ_0 [S·cm^{-1}]	A	n	τ [s]	β	M_∞
0	$1.04 \cdot 10^{-8}$	$1.58 \cdot 10^{-11}$	0.748	$1.2 \cdot 10^{-5}$	0.52	0.21
5	$2.80 \cdot 10^{-8}$	$2.03 \cdot 10^{-12}$	0.883	$5.3 \cdot 10^{-5}$	0.57	0.26
10	$2.08 \cdot 10^{-8}$	$1.31 \cdot 10^{-12}$	0.887	–	–	–
20	$1.92 \cdot 10^{-8}$	$3.11 \cdot 10^{-11}$	0.819	$5.0 \cdot 10^{-5}$	0.55	0.36
30	$1.78 \cdot 10^{-8}$	$2.74 \cdot 10^{-12}$	0.813	$5.5 \cdot 10^{-5}$	0.56	0.40
50	$1.38 \cdot 10^{-8}$	$3.45 \cdot 10^{-12}$	0.787	$5.5 \cdot 10^{-5}$	0.57	0.42

where n_i, μ_i, and z_i refer to charge carrier, ionic mobility, and ionic charge of i^{th} ion respectively. It is clear from the equation that the conductivity depends on the amount of charge carrier (n_i), and the mobility of the ionic species in the system. Addition of clay can increase the fraction of free ions (i.e., increase of n_i) because the negative charge in the silicate layers can interact with the Na^+ cation and disturb the attractive forces between cation and anion of the salt. When excesses amount of DMMT is added to polymer-salt complex, there may be an increase in the system viscosity and thus restricted cation mobility (i.e., decrease of μ_i), as a result, lower ionic conductivity is observed. Therefore, it can be concluded that the addition of optimum clay concentration (i.e., 5% DMMT) provides the most suitable environment for the ionic transport and achieving the highest conductivity, which is consistent with the reported one [26].

Microscopic models such as dynamic bond percolation and dynamic disorder hopping models have been proposed [27] to describe the long-range ion transport in polymer electrolytes. According to these models, the renewal time, τ_{ren}, for the segmental reorganization arising from the changes in the local geometry due to the coordination of cations with the polymer Lewis base sites, lie within the microwave range. Moreover, these models explain the frequency dependence of conductivity satisfactorily only above 100 MHz region. Hence, a physical model (i.e., jump relaxation model) was developed for structurally disordered ionic conductors [28] in order to rationalize the observed frequency dispersion. Since the dynamical effects of the polymer host due to the segmental renewing rates become less significant below microwave region. According to jump relaxation model, at very low frequencies ($\omega \to 0$) an ion can jump from one site to its neighboring vacant site successfully contributing to the dc conductivity. At higher frequencies, the probability for the ion to go back again to its initial site increases due to the short time periods available. This high probability for the correlated forward-backward hopping at higher frequencies together with the relaxation of the dynamic cage potential is responsible for the observed high frequency conductivity dispersion.

3.6. Electrical modulus analysis

The conductivity behavior in the frequency domain is more conveniently interpreted in terms of conductivity relaxation time, τ, using the representation of electrical modulus, $M^* = 1/\varepsilon^*$ [29]. The M^* representation is now widely used to analyze ionic conductivities by associating a conductivity relaxation time with the ionic process [30, 31]. In the M^* representation, a relaxation peak is observed for the conductivity process in the frequency spectra of the imaginary component of M^*. Comparison of the M^* and ε^* representations has been used to distinguish localized dielectric relaxation processes from long-range conductivity [32]. Figure 7 shows the variation of imaginary part of electrical modulus (M'') as a function of frequency for different clay concentration. The observed M'' peak in the plot is related to conuctivity relaxation of the materials. The KWW (Kohlrausch-Williams-Watts) stretched exponent function, given in Equation (7):

$$\Phi = \Phi_0 \exp\left[\left(\frac{-t}{\tau}\right)^\beta\right] \tag{7}$$

(where β is the stretching constant and τ is the characteristic relaxation time) was used to fit the M'' data. The modulus fitting was performed using the procedure of Moynihan *et al.* [29, 30] and the fitting (alogorithim) described in literature [33] was

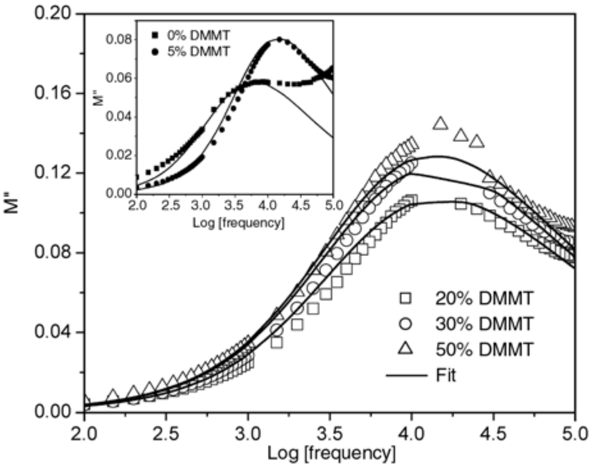

Figure 7. Imaginary part of electrical modulus (M'') vs. log(f) for different concentration of DMMT at room temperature. The continues solid line represents the fit of experimental M'' data to the decay function $\Phi = \Phi_0 \exp[(-t/\tau)^\beta]$.

used in our analysis. The continuous line of Figure 7 denotes the fitted value of M'' whereas the symbol corresponds to experimental data. A good agreement between the experimental data and fitted curve is evident from the figure. The value of stretching exponent parameter β, the conductivity relaxation time τ and the high frequency limit of the real part of M^* ($M_\infty = 1/\varepsilon_\infty$) obtained from the fitting are compared in Table 1 for different clay concentration. From the table it is clear that β value of the nanocomposite is always higher than that of the polymer salt complexes and the M_∞ value increases on increasing clay concentration. It is well known that β is the relaxation parameter, which increases by decreasing in the width of the relaxation time distribution.

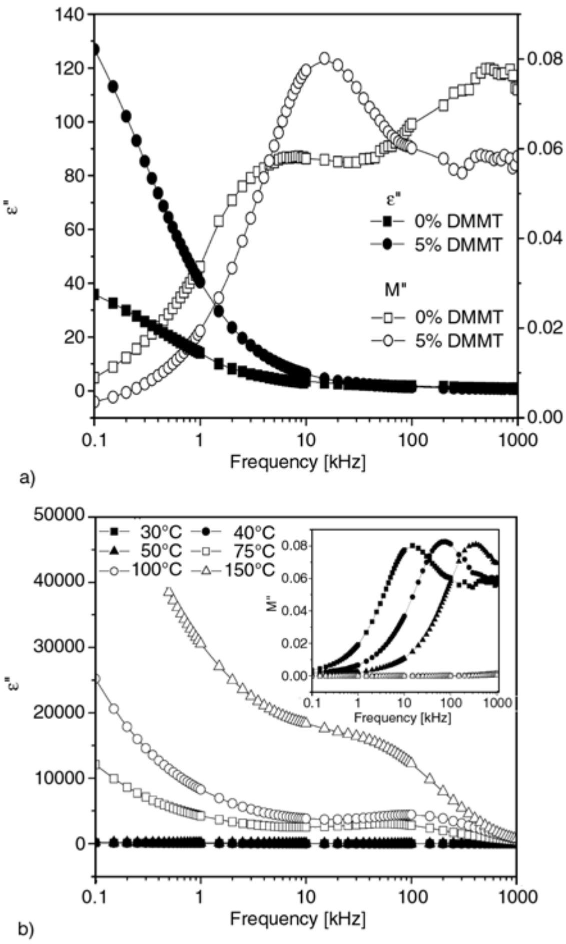

Figure 8. Variation of imaginary part of dielectric permittivity and modulus of PNCEs as a function of frequency for (a) $(PEO)_{25}$-NaI+x wt.% DMMT for $x = 0\%$ and 5% at room temperature (30°C) (b) for $x = 5\%$ at different temperatures.

For dielectric relaxation processes, however, relaxation peaks are observed in both M^* and ε^* representation when the two peak position in two representations are related by the ratio $\varepsilon_s/\varepsilon_\infty$ where ε_s is the static dielectric constant and ε_∞ is the dielectric constant at higher frequency limit. A comparison of the experimental data of the M^* and ε^* formalism is, therefore, useful to distinguish long-range conduction process from the localized dielectric relaxation. To visualize this, we have plotted the imaginary part of complex dielectric permittivity (ε'') and modulus (M'') as a function of frequency for 0 and 5% clay concentration of PNCEs as representative (Figure 8a) (similar behaviors are found for other compositions). Dielectric relaxation is a result of the reorientation process of dipoles in the polymer chains, which show a peak in ε'' spectra. For electrolyte, with higher ion concentration the movement of ions from one site to another will perturb the electric potential of the surroundings. Motion of the other ions in this region will be affected by perturb potential. Such a cooperative motion of ions will lead to non-exponential decay, or a conduction processes with distribution of relaxation time [34]. In the imaginary part of modulus spectra a relaxation peak is observed (Figure 8a) for the conductivity processes, whereas no peak is observed in the dielectric spectra. This suggests that ionic motion and polymer segmental motion are strongly coupled manifesting as peak in the M'' spectra with no corresponding feature in dielectric spectra [35]. Similar results have been reported by Fu *et al.* [34] for PPG-$LiCF_3SO_3$ system with higher salt concentration (i.e., O:Li = 30:1, 16:1, and 12:1). So the conduction in polymer electrolytes takes place through charge migration of ions between coordinated sites of the polymer along with its segmental relaxation. In addition to the main M'' peak in the low frequency region, a small peak is observed at the high frequency which is less pronounced in the 5% DMMT composite. The existence of these two peaks may be due to the heterogeneity in the texture of the polymer composites [36]. The temperature dependence of imaginary part of dielectric permittivity (ε'') and modulus (M'') as a function of frequency for $x = 5\%$ clay concentration (as representative) is shown in Figure 8b. The low frequency M'' peak shifts towards the high frequency side with rise in temperatures, but at higher temperatures we do not observe any peak. At lower temperatures, ε'' decreases on increasing frequency whereas at higher temperatures ε'' first decreases with rise in frequency (in low frequency region) followed by a peak in the loss spectra. The higher value of dielectric loss (ε'') at low frequency is due to the free charge motion within the materials. The appearance of peak is attributed to the relaxation phenomena of polymer.

4. Conclusions

The frequency dependent electrical conductivity and the associated conductivity relaxation of an ionically conducting polymer nanocomposite films was studied for different DMMT concentration. X-ray diffraction (XRD) analysis shows that the polymer-salt complexes have been intercalated into the nanometric channel of silicate layers of DMMT suggesting the formation of nanocomposites. Complex impedance analysis shows the existence of bulk and material-electrode interface properties of the nanocomposites. The electrical modulus formalism (used to describe the conductivity relaxation process), shows that the conductivity relaxation data can best be represented in terms of the stretched exponential correlation function, $\Phi = \Phi_0 \exp[(-t/\tau)^\beta]$. The ac conductivity spectrum obeys the universal power law in the high frequency region whereas strong low frequency dispersion was assigned to the electrode polarization effect. The conduction may be due to the drift of ions coupled to polymer segmental relaxation of polymer matrix.

References

[1] Pinnavaia T. J., Beall G. W.: Polymer-clay nanocomposites. John Wiley and Sons, New York (2001).

[2] Tjong S. C.: Structural and mechanical properties of polymer nanocomposites. Materials Science and Engineering: Reports, **53**, 73–197 (2006).

[3] Ruiz-Hitzky E.: Conducting polymers intercalated in layered solids. Advanced Materials, **5**, 334–340 (1993).

[4] Ruiz-Hitzky E., Aranada P., Casal B., Galvan J. C.: Nanocomposite materials with controlled ion mobility. Advanced Materials, **7**, 180–184 (1995).

[5] Gainnelis E. P.: Polymer layered silicate nanocomposite. Advanced Materials, **8**, 29–35 (1996).

[6] MacCallum J. R., Vincent C. A.: Polymer electrolyte review-I. Elsevier, London (1987).

[7] Meyer W. H.: Polymer electrolytes for lithium-ion batteries. Advanced Materials, **10**, 439–448 (1998).

[8] Gray F. M: Polymer electrolytes. The Royal Society of Chemistry, Cambridge (1997).

[9] Fauteux D., Lupien M. D., Robitaille C. D.: Phase diagram, conductivity and transference number of PEO-NaI electrolyte. Journal of the Electrochemical Society, **134**, 2761–2767 (1987).

[10] Rietman E. A., Kaplan M. L., Cava R. J.: Lithium ion-poly(ethylene oxide)complexes. I. Effect of anion on conductivity. Solid State Ionics, **17**, 67–73 (1985).

[11] Bruce P. G.: Solid state electrochemistry. Cambridge University Press, Cambridge (1995).

[12] Sinha Ray S., Okamoto M.: Polymer/layered silicate nanocomposites: A review from preparation to processing. Progress in Polymer Science, **28**, 1539–1641 (2003).

[13] Ratna D., Divekar S., Samui A. B., Chakraborty B. C., Banthia A. K.: Poly(ethylene oxide)/clay nanocomposite: Thermomechanical properties and morphology. Polymer, **47**, 4068–4074 (2006).

[14] Thakur A. K., Pradhan D. K., Samantaray B. K., Choudhary R. N. P.: Studies on an ionically conducting polymer nanocomposite. Journal of Power Sources, **159**, 272–276 (2006).

[15] Pradhan D. K., Samantaray B. K., Choudhary R. N. P., Thakur A. K.: Effect of plasticizer on structure-property relationship in composite polymer electrolyte. Journal of Power Sources, **139**, 384–393 (2005).

[16] Chen H-W., Lin T-P., Chang F-C.: Ionic conductivity enhancement of the plasticized PMMA/$LiClO_4$ polymer nanocomposite electrolyte containing clay. Polymer, **43**, 5281–5288 (2002).

[17] Cameron G. G., Ingram M. D., Qureshi M. Y., Gearing H. M., Costa L., Camino G.: The thermal degradation of poly(ethylene oxide) and its complexes with NaCNS. European Polymer Journal, **25**, 779–784 (1989).

[18] Shen Z., Simon G. P., Cheng Y-B.: Saturation ratio of poly(ethylene oxide) to silicate in melt intercalated composite. European Polymer Journal, **39**, 1917–1924 (2003).

[19] Macdonald J. R.: Impedance spectroscopy, emphasizing solid materials and systems. Wiley, New York (1987).

[20] Dias F. B., Batty S. V., Voss J. P., Ungar G., Wright P. V.: Ionic conductivity of a novel smectic polymer electrolyte. Solid State Ionics, **85**, 43–49 (1996).

[21] Qian X., Gu N., Cheng Z., Yang X., Wang E., Dong S.: Plasticizer effect on the ionic conductivity of PEO-based polymer electrolyte. Materials Chemistry and Physics, **74**, 98–103 (2002).

[22] Kanapitas A., Pissis P., Kotsilkova R.: Dielectric studies of molecular mobility and phase morphology in polymer-layered silicate nanocomposites. Journal of Non-Crystalline Solids, **305**, 204–211 (2002).

[23] Jonscher A. K.: Dielectric relaxation in solids. Chelsea Dielectric Press, London (1983).

[24] Jonscher A. K.: The universal dielectric response. Nature, **267**, 673–679 (1977).

[25] Mauritz K. A.: Dielectric relaxation studies of ion motion in electrolyte-containing perfluorosulfonate ionmres. 4. Long range ion transport. Macromolecules, **22**, 4483–4488. (1989).

[26] Chen H-W., Chiu C-Y., Wu H-D., Shen I-W., Chang F-C.: Solid-state electrolyte nanocomposites based on poly(ethylene oxide), poly(oxypropylene)diamine, mineral clay and lithium perchlorate. Polymer, **43**, 5011–5016 (2002).

[27] Ratner M. A., Shriver D. F.: Ion transport in solvent free polymers. Chemical Reviews, **88**, 109–124 (1988).

[28] Funke K.: Jump relaxation in solid electrolytes. Progress in Solid State Chemistry, **22**, 111–195 (1992).

[29] Macedo P. B., Moynihan C. T., Bose R.: Role of ionic diffusion in polarization in vitreous ionic conductors. Physics and Chemistry of Glasses, **13**, 171–179 (1972).

[30] Moynihan C. T., Boesch L. P., Laberge N. L.: Decay function for the electric field relxation in vitreous ionic conductors. Physics and Chemistry of Glasses, **14**, 122–125 (1973).

[31] Angell C. A.: Dynamic processes in ionic galsses. Chemical Reviews, **90**, 523–542 (1990).

[32] Gerhardt R.: Impedance and dielectric spectroscopy revisited: Distinguishing localized relaxation from long-range conductivity. Journal of Physics and Chemistry of Solids, **55**, 1491–1506 (1994).

[33] Baskaran N.: Conductivity relaxation and ion transport processes in glassy electrolyte. Journal of Applied Physics, **92**, 825–833 (2002).

[34] Fu Y., Pathmanathan K., Stevens J. R.: Dielectric and conductivity relaxation in poly(propylene oxide)-lithium triflate complexes. The Journal of Chemical Physics, **94**, 6323–6329 (1991).

[35] Jeevanandam P., Vasudevan S.: Arrhenius and non-Arrhenius conductivities in intercalated polymer electrolytes. Journal of Chemical Physics, **109**, 8109–8117 (1998).

[36] Chanmal C. V., Jog J. P.: Dielectric relaxations in PVDF/$BaTiO_3$ nanocomposites. Express Polymer Letters, **2**, 294–301 (2008).

eXPRESS Polymer Letters Vol.2, No.9 (2008) 639–654
Available online at www.expresspolymlett.com
DOI: 10.3144/expresspolymlett.2008.77

Synthesis and characterization of functional copolymer/organo-silicate nanoarchitectures through interlamellar complex-radical (co)terpolymerization

E. Söylemez[1], *N. Çaylak*[2], *Z. M. O. Rzayev*[1*]

[1]Department of Chemical Engineering, Faculty of Engineering, Hacettepe University, 06800 Ankara, Turkey
[2]Department of Physics, Faculty of Art & Science, Sakarya University, 54187 Sakarya, Turkey

Received 26 June 2008; accepted in revised form 27 July 2008

Abstract. The functional copolymers, having a combination of rigid/flexible linkages and an ability of complex-formation with interlayered surface of organo-silicate, and their nanocomposites have been synthesized by interlamellar complex-radical (co)terpolymerization of intercalated monomer complexes of maleic anhydride (MA) and itaconic acid (IA) with dimethyl dodecylamine surface modified montmorillonite (organo-MMT) (MA…DMDA-MMT and IA…DMDA-MMT) *n*-butyl methacrylate (BMA) and/or BMA/styrene monomer mixtures. The results of nanocomposite structure–composition–property relationship studies indicate that interlamellar complex-formation between anhydride/acid units and surface alkyl amine and rigid/flexible linkage balance in polymer chains are important factors providing the effective intercalation/exfoliation of the polymer chains into the silicate galleries, the formation of nanostructural hybrids with higher thermal stability, dynamic mechanical behaviour and well dispersed morphology.

Keywords: *polymer synthesis, molecular engineering, interlamellar copolymerization, nanocomposites, thermal properties, dynamic mechanical properties*

1. Introduction

In the last decade, the attention of many researchers focused on thermoplastic and thermoset polymer silicate layered (PLS), polymer/silica hybrid and polymer/carbon nanotube nanocomposites. This considerable scientific and engineering interest has been stimulated by possibility of the significant improvements in physical, mechanical, thermal and other important specific properties of PLS materials. The results of these researches were summarized and discussed in several reviews and articles [1–7]. PLSs are a class of organic-inorganic hybrids, composed of organic polymer matrix in which layered silicate particles of nano-scale dimension are embedded because these nanocomposites show enhanced mechanical properties [8, 9], gas barrier properties [10], and improved thermal stability [5, 11, 12], low flammability [11, 12] and protection effects from corrosion [13, 14].

Nowadays, organo-clays, especially organo-montmorillonite (MMT) are the most widely utilized silicates in polymer nanotechnology. MMT is a layered silicate crystal lattice which consists of two silica tetrahedral and one aluminium octahedral sheets with a plate-like structure of 1 nm thickness and 100 nm length [15]. The synthesis ways from functional monomers (maleic anhydride and its analogues) to polymer/clay (or silica) nanocomposites include three main methods such as (1) interlamellar (or intercalative, intragallery, etc.) copolymerization in the presence of various type of mineral silicates and organo-silicates, (2) intercalation

---

[*]Corresponding author, e-mail: zmo@hacettepe.edu.tr

of thermoplastic polymers in melt by reactive extrusion *in situ* processing and (3) sol(hydro)-gel method, i.e., reactions of anhydride (or carboxylic group)-containing polymers with organosilanes (polymer/silica hybrid synthesis). Last two methods, especially intercalation of polymers, are the most promising ways to synthesize polymer/intercalant-clay nanocomposites on the base of graft copolymers of maleic anhydride and its analogues as reactive compatibilizers.

Although the most promising reaction to great polymer/clay nanocomposites is the *in situ* polymerization of functional monomers, such as styrene [16, 17], *N*-vinylcarbazole [18], 4-vinyl-pyridine [19], methyl methacrylate [20, 21], acrylonitrile [22] and *N*-*n*-butylmaleimide [23], as well as synthesis of low-molecular-weight polyamide 6/hydrotalcite intercalated nanocomposites via *in situ* polymerization [24], whereas the intercalative radical copolymerization of binary or ternary monomer systems in the presence of mineral clay has been scarcely investigated. The polymerization of acrylate [25, 26], styrene-4-sulfonate [27], sulfopropyl methacrylate [28] and acrylic acid [29] in the inorganic layered materials have also been investigated as organic/inorganic nanocomposite materials. Yu *et al*. [29] completely polymerized the acrylic acid regularly fixed in layered aminopropylsilica without initiator at 100°C for 24 h to form a novel organic/inorganic nanocomposite named as layered polyacrylamide propylsilica. Examples for interlamellar polymerization of the binary monomer systems are bulk copolymerization of styrene-methyl methacrylate [23, 27, 30], emulsion copolymerization of styrene-acrylonitrile [31], styrene-phenyl maleimide (PhMI) [32] and styrene-butyl methacrylate [33] monomer pairs. It was observed that the polymerization rate was accelerated by the addition of the clay in reaction medium; this addition also significantly influenced the structure and properties of the prepared polymer nanocomposites [23, 27, 34]. Liu *et al.* [35] investigated the bulk, solution and emulsion copolymerization of styrene with methyl methacrylate and *N*-phenylmaleimide (PhMI) (at 1:9 molar PhMI/styrene feed ratio) in the presence of organo(cetyltrimethyl ammonium bromide)-modified MMT or Na^+-MMT in order to prepare nanocomposites with good dispersability of clay. According to the authors, the catalytic effect of the clay on a polymerization may be mostly caused by the small-size effect of the clay layers, and the active sites are on the surface of the clay particles rather than between layers. Wang *et al.* [36, 37] showed that a comparison of solution, emulsion, suspension and bulk polymerization along the nanocomposites may also be prepared by melt *in situ* reactive blending of monomer/polymer/clay mixtures.

Recently, we have reported the synthesis of the functional copolymer/silica (or organo-silicate) hybrids and polypropylene/organo-MMT nanocomposites by (1) reaction of anhydride-containing copolymers with γ-aminopropyltriethoxysilane [38–40], (2) interlamellar copolymerization of maleic anhydride with some vinyl and acrylic comonomers [40] and (3) reactive extrusion *in situ* processing [4, 40]. In this work, we present (a) the synthesis of poly[maleic anhydride (MA)-*co*-*n*-butylmethacrylate (BMA)/organo-MMT, poly(MA-*alt*-styrene-*co*-BMA)/organo-MMT, and poly[ita-

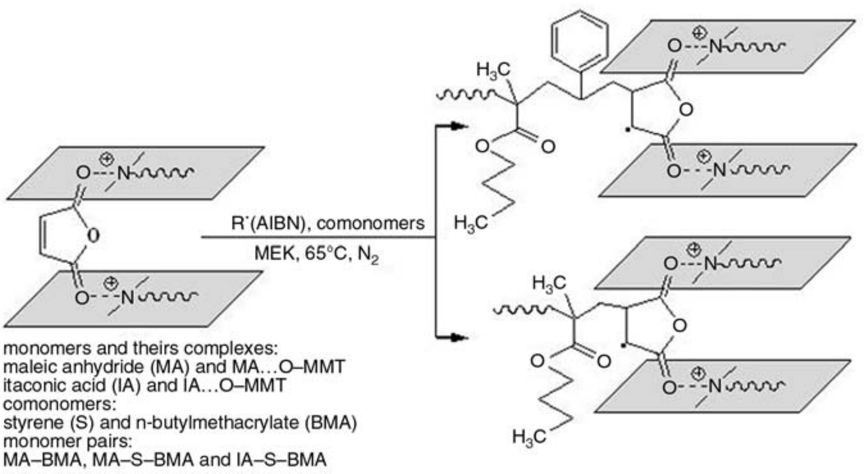

Figure 1. Schematic representation of interlamellar complex-radical (co)terpolymerizations

conic acid (IA)-*co*-styrene-*co*-BMA)]/organo-MMT nanoarchitectures prepared by complex-radical interlamellar copolymerization, (b) the results of the copolymer composition-nanostructure formation relationship studies, and (c) characterization of (co)terpolymer/organo-MMT nanocomposites by thermal (DSC and TGA-DTG), dynamic mechanical (DMA), X-ray diffraction (XRD) and scanning electron microscopy (SEM) analysis methods. Special attention is paid to the role of complex formation of MA (or IA) and its (co)terpolymers with dimethyldodecylamine (DMDA) surface modified silicate layers in interlamellar co(ter)polymerization reactions and intercalation/exfoliation of polymer chains between silicate galleries. Taking into consideration of this effect, general scheme of interlamellar (co)terpolymerizations can be represented as shown in Figure 1.

2. Experimental

2.1. Materials

S and BMA monomers (Aldrich) were purified before use by distillation under moderate vacuum. MA and IA monomers were obtained from Fluka (Switzerland). MA was purified by recrystallization from anhydrous benzene and sublimation in vacuum. IA monomer was purified by recrystallization from distilled water solution and drying at 60°C. The α,α′-azoisobutyronitrile (AIBN) (Fluka) was recrystallized twice before use from methanol. DMDA-MMT (Viscobent SB-1) was purchased from Bensan (Enez, Turkey) having the following average parameters: specific surface area 43.6 $m^2 \cdot g^{-1}$, specific mesopore volume 0.14 $cm^3 \cdot g^{-1}$, content of N 1.12% and C 32.56%, crystallinity 58.2% (by XRD), melting point (T_m) 160°C (by DSC for the surface alkyl ammonium complex), temperature of decomposition for $T_{d(onset)}$ 238°C and $T_{d(max)}$ 361°C (by TGA). All other solvents and reagents were of analytical grade and used without purification.

2.2. Terpolymerization procedure

Terpolymerization of MA, S and BMA using given molar monomer feed ratios of (MA (or IA):S):BMA = (1:1):1.23–5.0 were carried out in methyl ethyl ketone (MEK) or in *N,N′*-dimethylformamide (DMF) (for IA/basic monomer system) with AIBN as an initiator at constant total concentration of monomers under nitrogen atmosphere. Reaction conditions: $[M]_{total} = 2.86–3.04\ mol \cdot l^{-1}$, $[AIBN] = 2.03 \cdot 10^{-2}\ mol \cdot l^{-1}$, $[Solvent]/[M] = 3$, molar monomer ratios of (MA:S)/BMA = 0.20–0.81, reaction time 24 h, and conversion around 75–92 wt%. Appropriate quantities of monomers, solvent (MEK or DMF) and AIBN were placed in a standard Pyrex-glass reactor, and was cooled by liquid nitrogen and flushed with dried nitrogen gas for at least 3 min, then soldered and placed in a carousel type microreactor with a thermostated heater and magnetic mixer. The reaction mixture was stirred at 65 ± 0.1°C for 24 h. The resulting terpolymers were isolated from reaction mixture by precipitating with diethyl ether, then washed with several portions of benzene and dried at 40°C under vacuum. The terpolymer compositions were found by chemical (acid number for MA units) analysis, and ^1H NMR spectroscopy (Figure 2) using integral area of chemical shifts of monomer functional groups for quantitative analysis. Under similar conditions, poly(MA-*co*-BMA) with given composi-

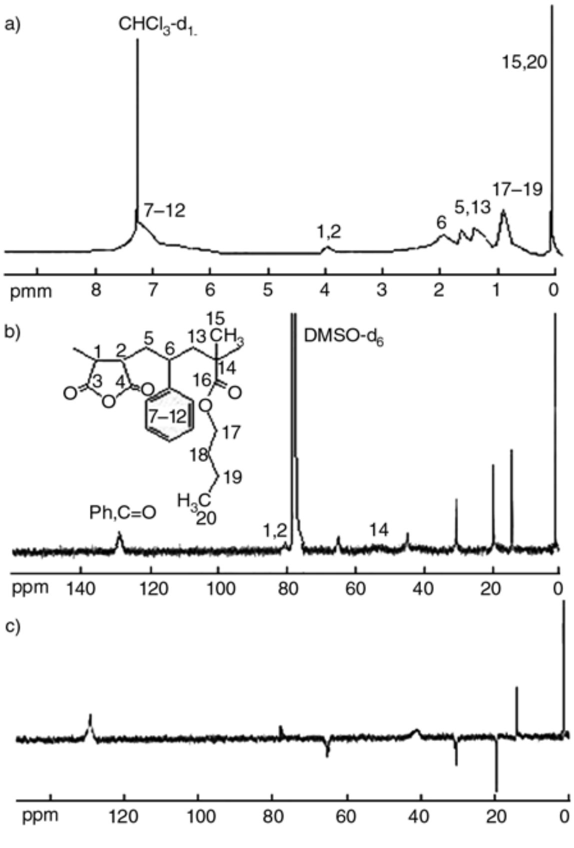

Figure 2. (a) ^1H NMR (in $CHCl_3$-d_1), (b) ^{13}C NMR (in DMSO-d_6) and (c) ^{13}C NMR-DEPT-135 (in DMSO-d_6, CH_2 region in negative position) spectra of poly(MA-*alt*-S-*co*-BMA)

Table 1. Some characteristics of the binary and ternary copolymers

(Co)terpolymers	**BMA-unit [mol%]** **(unit ratio)**	**Acid number** **[mg KOH·g^{-1}]**	**[η]$_{in}$ [g·dl^{-1}]** **in DMF at 25 ± 0.1°C**	**T$_g$ [°C]** **(by DSC)**
Poly(MA-*co*-BMA)	38.5 (1:1.25)	398	0.235	59.0
Poly(MA-*alt*-S-*co*-BMA)-1	36.7 (1:1:1.16)	301	0.384	122.5
Poly(MA-*alt*-S-*co*-BMA)-2	54.2 (1:1: 2.37)	205	0.352	100.6
Poly(MA-*alt*-S-*co*-BMA)-3	71.1 (1:1: 4.92)	125	0.305	80.2

tion was synthesized. Some characteristics of synthesized (co)terpolymers are presented in Table 1.

2.3. Interlamellar (co)terpolymerization procedure

MA (or IA) monomer was dispersed in MEK (or DMF)/DMDA-MMT mixture at monomer/alkyl amine molar ratio of 1:2 by intensive mixing at 40°C for 3 h before reaction to prepare the intercalated complex of monomer with surface alkyl amine. Then appropriate amount of S and BMA comonomers and AIBN (1.0 wt%) was added to reaction mixture containing organo-MMT…MA (or IA) complex and heated with mixing at 65°C under nitrogen atmosphere for 24 h. Prepared composition was isolated by precipitation with diethyl ether, then washed with several portions of benzene and dried under vacuum at 60°C.

2.4. Characterization

FT-IR spectra of the (co)terpolymers (KBr pellet) were recorded with FT-IR Nicolet 510 spectrometer in the 4000–400 cm^{-1} range, where 30 scans were taken at 4 cm^{-1} resolution. ^{1}H {^{13}C and ^{13}C-DEPT-135} NMR spectra were performed on a JEOL 6X-400 (400 MHz) spectrometer with $CHCl_3$-d_1 or DMSO-d_6 as a solvent at 25°C. Molar fractions of the comonomer units [m_1 and m_2, where m_1 is (MA–S) alternating diad and m_2 is BMA unit] in terpolymers were calculated according to the Equation (1) using NMR analysis data:

$$\frac{m_1}{m_2} = \frac{n_2 Am_1\ (\text{Ph or CH})}{n_1 Am_2\ (\text{CH}_3)} \tag{1}$$

where n_1 and n_2 are the integers of proton(s) in the functional groups of the monomer units, A_{m1} and A_{m2} are the integral areas per proton from corresponding groups of the monomer unit regions in ^{1}H NMR spectra.

Acid numbers of the anhydride (or carboxylic)-containing (co)terpolymers were determined by standard titration method. Intrinsic viscosities of the (co)terpolymers with different compositions were determined in DMF at 25 ± 0.1°C within the concentration range of 0.05–1.5 g·dl^{-1} using an Ubbelohde viscometer. Thermogravimetric (TGA) and differential thermogravimetric (DTG) analyses were performed on a Setaram Labsys TG-DTA 12 Thermal Analyzser (France) at a heating rate of 5°C/min, under nitrogen atmosphere. The differential scanning calorimetry (DSC) was performed on a Shimadzu calorimeter (Japan). Dynamic mechanical analysis (DMA) was performed on a TA Instrument-Q800. Scanning electron microscopy (SEM) patterns were recorded using a JSM-6400 JEOL SEM with an acceleration voltage of 30 kV.

The X-ray diffraction (XRD) patterns were obtained from a Rigaku D-Max 2200 powder diffractometer. The XRD diffractograms were measured at 2θ, in the range 1–50°, using a CuK$_\alpha$ incident beam (λ = 1.5406 Å), monochromated by a Ni-filter. The scanning speed was 1°/min, and the voltage and current of the X-ray tubes were 40 kV and 30 mA, respectively. The Bragg equation was used to calculate the interlayer spacing (d): $n\lambda = 2d\sin\theta$, where n is the order of reflection, and θ is the angle of reflection. Crystallinity of the nanocomposites was calculated using the Equations (2) and (3) [41]:

$$\chi_c = \frac{\int_0^\infty s^2 I_c(s) d}{\int_0^\infty s^2 I(s) d} \tag{2}$$

where s is the magnitude of the reciprocal-lattice vector which is given by $s = (2\sin\theta)/\lambda$ (θ is one-half the angle of deviation of the diffracted rays from the incident X-rays and λ is the wavelength); $I(s)$ and $I_c(s)$ are the intensities of coherent X-ray scattering from both crystalline and amorphous regions and from only crystalline region of polymer sample, respectively, and d is interlayer spacing.

$$\chi_c = \frac{W_c}{W_c + W_a} \cdot 100 \tag{3}$$

where W_c and W_a are the areas of the crystalline and amorphous portions in the X-ray diffractogram, respectively.

Intercalation or exfoliation degree (ED) was calculated according to the Equation (4):

$$\mathrm{ED}\,[\%] = \frac{I_e}{I_e + I_0} \cdot 10^{-2} \tag{4}$$

where I_e (or I_c) and I_0 are the intensity of the diffraction peaks associated with the exfoliated and non-exfoliated structures at corresponding 2θ values.

3. Results and discussion

3.1. Complex-radical interlamellar copolymerization

Intercalation and exfoliation of functional polymer chains between surface modified silicate layers are one of the most important processes proceeding through chemical or physical interactions of functional groups from the monomers and/or growing polymer chains with surface alkyl amine in the interlamellar copolymerization. Character of this interaction strongly depends on the nature and functionality of the chosen monomer and polymer chains, which may provide an effective interaction with silicate layers via complex-formation, hydrogen bonding, and amidization/imidization reactions (in the case of primary alkyl amine modified MMT [4]). Effect of H-bonding in ternary solvent/proton-donor polymer/proton-acceptor polymer system was also reported by Figueruelo *et al.* [42]. Taking this principle into consideration, we have investigated the radical-initiated interlamellar copolymerization of MA as a strong hydrophilic electron-acceptor monomer with BMA as an amphiphilic comonomer and interlamellar copolymerization of two monomer systems such as MA–BMA and itaconic acid (IA as a hydrophilic electron-acceptor monomer capable of H-bonding)–BMA in the presence of DMDA surface modified MMT silicate layers as a surfactant with positive charge tertiary amine group ending. The functional copolymers, having a combination of rigid/flexible linkages and an ability of complex-formation with interlayered surface of organo-silicate, and their nanocomposites have been synthesized by interlamellar complex-radical copolymerization of MA or IA (acceptor monomer) and *n*-butyl methacrylate (BMA-acceptor) in MEK (or DMF) at 70°C in the interlayered region of DMDA surface modified MMT (DMDA-MMT) used as a nano-reactor (Figure 1). To elucidate the effect of DMDA-MMT in copolymerization and its interaction with functional monomers, especially with MA and IA monomer units, and in the formation of nano-structures, we also synthesized pure copolymers under similar conditions without DMDA-MMT for the comparative analysis of the obtained results. It was observed that copolymerization rate and copolymer conversion significantly depend on the presence of DMDA-MMT. Addition of DMDA-MMT as a complex-forming agent essentially increases the copolymer yield. This fact can be explained by the catalytic effect of organo-MMT as a complex-forming agent, which is similar to the well known effect of Lewis acids in complex-radical polymerizations [43]. Catalytic effect of organo-silicates in radical polymerization of vinyl and acrylic monomers have also been observed by many researchers [23, 27, 34, 35].

In order to increase the effectivity of intercalation process and therefore, the formation of nano-structures in the studied system, MA and IA monomers were dispersed between silicate galleries before copolymerization reactions to prepare the fixed interlayer anhydride/alkyl amine (MA…DMDA-MMT) and carboxylic acid/alkyl amine (IA… DMDA-MMT through strong H-bonding) com-

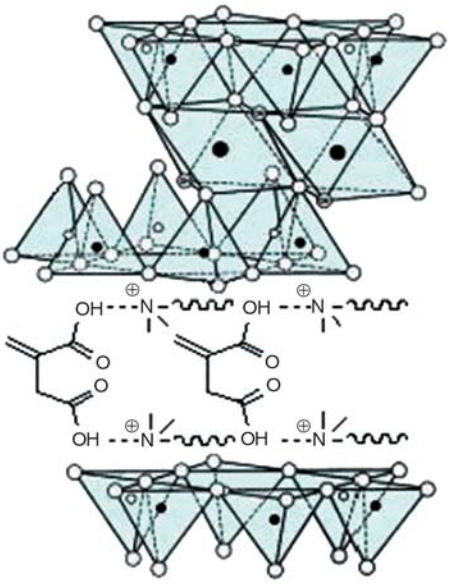

Figure 3. Interlamellar complex-formation via H-bonding in the IA/DMDA-MMT system

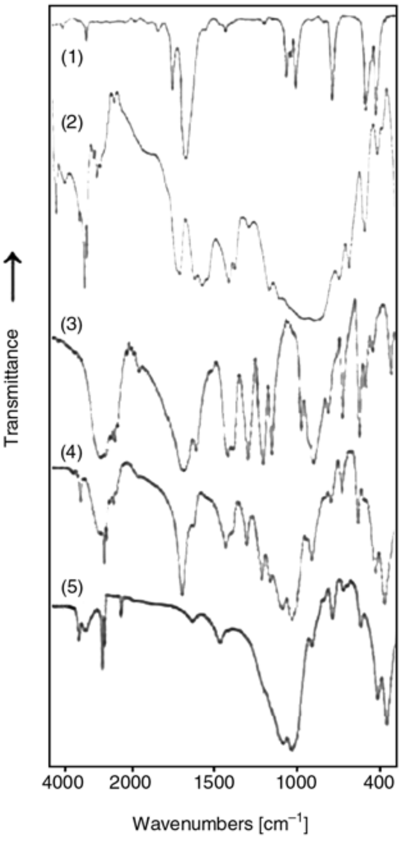

Figure 4. FTIR spectra of (1) MA monomer, (2) MA…DMDA-MMT complex, (3) IA monomer, (4) IA…DMDA-MMT complex and (5) pristine DMDA-MMT; effect of interlamellar complex-formation

plexes (Figure 3; here, well known lattice structural model of Hendricks for MMT was used [44]).

In this case, two carbonyl or carboxylic groups of the MA (or IA) monomer molecule interact with two neighbouring silicate platelet surfaces having tetrahedral structures, which contain alkyl ammonium cations, through interlayer complex or strong H-bonding. Structure of these molecular complexes was confirmed by FTIR spectroscopy (Figure 4). From comparative analysis of the spectra of free IA monomer, virgin DMDA-MMT and IA/DMDA-MMT system, the following changes of the characteristic bands were observed: (1) due to the formation of the interlayer molecular complexes, very broad 1705 cm^{-1} band (C=O in –COOH) of free IA monomer appeared in the spectra of IA–DMDA-MMT system in the form of a strong narrow band; (2) characteristic $CH_2=C <$ band at 1630 cm^{-1} for IA monomer shifted to 1636 cm^{-1} region due to the change of the conjugation effect of double bond with carbonyl group after its complex-formation with surface alkyl amine cations; (3) broad band at 3475 cm^{-1} associated with OH groups of DMDA-MMT disappeared, and a new broad band formed at 3125 cm^{-1}, overlapping with two weak bands for stretching ammonium cation and $CH_2=$ bands, respectively; (4) appearance of broad band at 4125 cm^{-1} can be related to complexed OH band in –COOH groups; (5) appearance of new bands at 1565–1470 (w) and 1400 cm^{-1} (m) related to the C–N deformation and –COO– sym. stretching bands, respectively, in $–(CH_2)_n–N^+ \cdot –OOC–$ complex.

Similar effect is obtained from comparative analysis of FT-IR spectra of the (co)terpolymers and their nanocompsities which are illustrated in Figure 5. The FT-IR spectra of poly(MA-*alt*-*S*-*co*-BMA), DMDA-MMT and their hybrid nanocomposite indicated the following changes of characteristic bands: (1) very broad absorption band around 1250–1000 cm^{-1} observed in the Si–O stretching region for virgin DMDA-MMT is transferred to relatively narrow doublet peak after interlamellar copolymerization, (2) appearance of a new band at 1625 cm^{-1} which is associated with complexed C=O band in $–C=O…N^+–$ complex as a result of *in situ* interaction between polar anhydride (or ester) unit and alkyl ammonium linkage, (3) presence of 850 and 800 cm^{-1} bands due to *in situ* esterification reaction of anhydride units of intercalated terpolymer macromolecules with surface silicate Si–OH groups, and (4) disappearance of 1633 cm^{-1} band

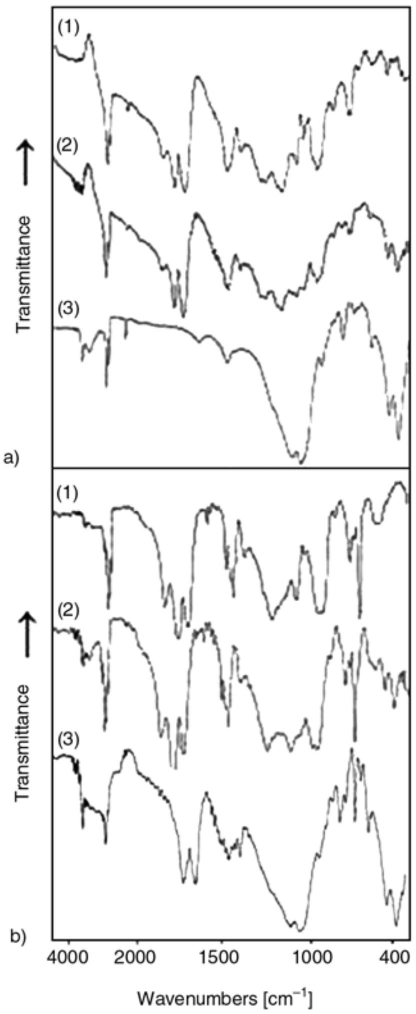

Figure 5. FTIR spectra of (a): (1) copolymer-1, (2) terpolymer-1, (3) virgin DMDA-MMT and (b): (1) copolymer-1/DMDA-MMT, (2) terpolymer-1/DMDA-MMT, (3) terpolymer-IA-1/DMDA-MMT

(water OH group) in DMDA-MMT spectra after intercalation/exfoliation due to the possible hydrolysis of anhydride units. These observed changes can serve as a reasonable agreement confirming the delamination of silicate layers due to the intercalation of the polar terpolymer macromolecules through *in situ* complexing with positive charged tertiary amine groups. On the other hand, hydrolysis and esterification of anhydride units with interlayer water molecules and Si–OH groups, respectively, in the surface of silicate layers during complex-radical interlamellar terpolymerization *in situ* processing are also possible.

3.2. Nanocomposite structure–thermal behaviour relationship

Studied (co)terpolymers consisting of an alternate sequence of rigid (MA or IA units and phenyl rings) and flexible (*n*-butylester side-chain and backbound main chain) molecular linkages can exhibit a liquid-crystalline behaviour [45]. Results of DSC analysis of virgin (co)terpolymers and their nanocomposites, illustrated in Figure 6 and summarized in Table 2, can serve as a reasonable agreement for this proposal. In both poly(MA-*co*-BMA) (C-1) and its nanocomposite (C-1-NC) DSC curves, the characteristic peaks at 59.0 and 63.0°C appeared, which can be related to glass transition (T_g) and melting point (T_m) temperatures for the amorphous and semi-crystalline copolymer and its nanocomposite, respectively. However, both systems did not exhibit recrystallization behaviour after reverse cooling of polymer samples from

Table 2. Thermal behaviour of the (co)terpolymers and their nanocomposites with constant amount of the DMDA-MMT (5.0 wt%)

Nanocomposite	DSC analysis		TGA analysis				
	T_m [°C]	ΔH [J/g]	$T_{d\ (onset)}$ [°C]	$T_{d\ (max)}$ [°C]	Weight loss [%] at [°C]		
					250	300	350
Poly(MA-*co*-BMA)/organo-MMT	63.0[a]	–	271 (262)[b]	381 (362)	0.0 (0.0)	3.2 (4.4)	23.8 (36.2)
Poly(MA-*alt*-S-*co*-BMA)-1/organo-MMT	143.2	10.9	274 (214)	427 (373)	0.0 (2.1)	5.9 (7.3)	18.3 (32.4)
Poly(MA-*alt*-S-*co*-BMA)-2/organo-MMT	115.0	15.6	301 (217)	382 (359)	0.0 (3.7)	5.2 (9.1	25.6 (38.4)
Poly(MA-*alt*-S-*co*-BMA)-3/organo-MMT	90.1	26.2	241 (237)	391 (373)	0.3 (1.4)	4.6 (6.8)	21.3 (34.1)
Poly(IA-*alt*-S-*co*-BMA)-1/organo-MMT	157.5	0.56	233	351	1.2	3.3	7.8
Pristine organo-MMT	160.0	1.3	238	361	3.7	9.4	38.2

[a] This value corresponds to T_g

[b] These values are related to the pure (co)terpolymers with different contents of BMA units (unit contents as in Table 1)

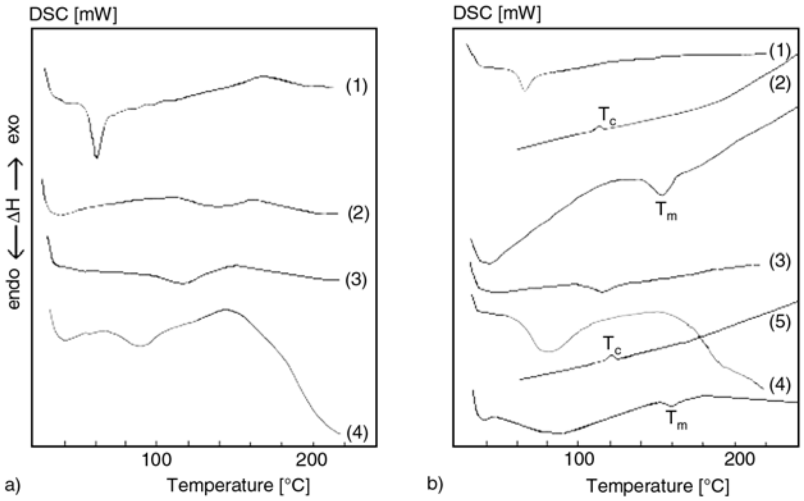

Figure 6. DSC curves of (a): (1) copolymer, (2) terpolymer-1, (3) terpolymer-2, and (4) terpolymer-3; (b): (1) copolymer/DMDA-MMT, (2) terpolymer-1/DMDA-MMT, (3) terpolymer-2/DMDA-MMT, (4) terpolymer-3/DMDA-MMT, and (5) pristine DMDA-MMT

200°C to room temperature in the DSC conditions. These results allow us to imply that these peaks are associated with glass transition or pseudo-melting temperature due to the side-chain *n*-butylester linkages which are able to form liquid crystalline structure. The terpolymers with different contents of BMA units exhibit typical T_g behaviour, the values of which essentially decrease with increasing flexible *n*-butylester units in the terpolymers. Unlike C-1-NC, terpolymer nanocomposites (T-1-NC, T-2-NC and T-3-NC) containing different mol% of BMA units exhibit T_m behaviour with characteristic recrystallization temperatures (T_c) (Figure 6). The Tm values of these nanocomposites significantly depend on the BMA content in terpolymers. As seen from DSC curves (Figure 6) and data in Table 2, the T_m values reduce from 140.1 to 94.8°C for virgin terpolymers and from 168.0 to 78.5°C for terpolymer/DMDA-MMT nanocomposites as a function of the content of flexible BMA linkages in terpolymers which is increased from 38.5 to 71.1 mol%. An increase of flexible hydrophobic *n*-butylester side-chain groups in terpolymer result with visible changes of enthalpy values (Δ*H*) of melting phase transition of nanocomposites. Poly(MA-*co*-BMA) and its nanocomposite exhibit typical glass-transition (T_g) behaviour with Δ*H* (copolymer) >Δ*H* (copolymer/DMDA-MMT).

As seen from Table 2, terpolymer/nanocomposite (T-1-IA-NC) prepared by interlamellar terpolymerization of IA, S and BMA exhibit relatively higher thermal behaviour than poly(MA-*alt*-S-BMA)/DMDA-MMT (T-1-NC) although the synthesized nanocomposites have an approximately similar composition and BMA unit content. This observed significant difference can be explained by the above mentioned structural factor, i.e., the formation of interlayer strong H-bonding in the presence of IA monomer and its terpolymer chain.

Nanocomposites and virgin organo-MMT showed a similar melting and re-crystallization behaviour while Δ*H* melting increased (area of peak decreased) in the case of the formation of nanostructural sections. Unlike virgin (co)terpolymers, the nanocomposites exhibit crystallization behaviour and similar dependence on the content of BMA linkage in terpolymers. The observed broad endo-peak around 65–110°C for virgin DMDA-MMT can be associated with the elimination of water trace. The weak endo- and exo-peaks observed in DSC curve of DMDA-MMT (Figure 6, curve b-3) can be related to the melting and crystallization processes of alkyl ammonium surfactant on the layered silicate surface, intensity (Δ*H* value) of which significantly increases after interlamellar copolymerization due to the formation of interlayer complexes between functional copolymer and alkyl amine.

TGA-DTG analysis (Figure 7) indicated the multistep degradation of virgin co(ter)polymers, while their DMDA-MMT nanocomposites showed a single step degradation. This observed effect can be explained by the formation of a more compact and organized structure in synthesized co(ter)copoly-

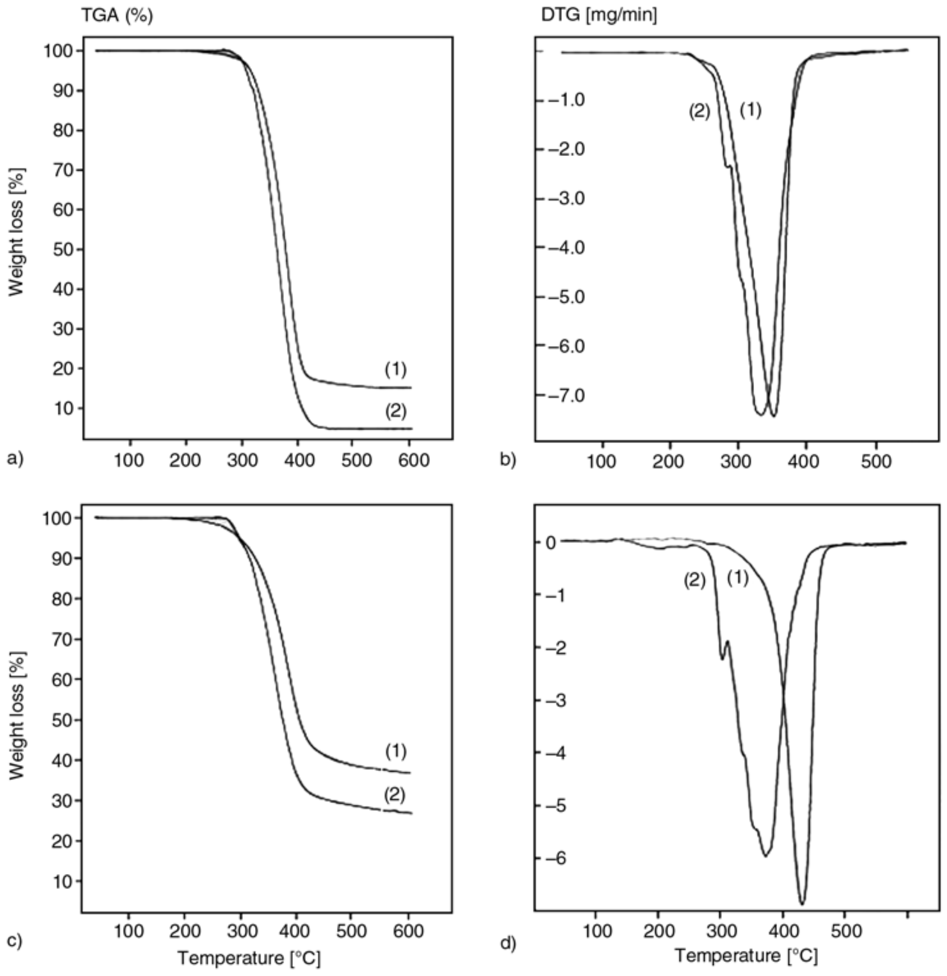

Figure 7. TGA (a and c) and DTG (b and d) curves of (1) (co)terpolymers and their (2) nanocomposites: (a)-1 and (b)-1 copolymer, (a)-2 and (b)-2 copolymer/DMDA-MMT, (c)-1 and (d)-1 terpolymer-1,(c)-2 and (d)-2 terpolymer-1/DMDA-MMT

mer/organo-MMT hybrids. Obtained results related to the thermal behaviour of virgin (co)terpolymers and (co)terpolymers/DMDA-MMT hybrids prepared by complex-radical copolymerization and interlamellar copolymerization, respectively, are summarized in Table 2. The comparative analysis of these results indicate that synthesized nanocomposites have relatively high T_m and thermal stability (degradation temperature and weight loss), and exhibit both the melting phase transition and crystallization behaviour. The improvement in the degradation temperature was significantly due to the homogeneous dispersion of the silicate galleries in the functional copolymer matrix.

Comparative DSC and TGA analyses of prepared (co)terpolymers and their nanocomposites showed that (1) the terpolymers exhibit relatively higher values of T_g and thermal stability as compared with copolymer due to the presence of the styrene units in the terpolymers and their high molecular weights (intrinsic viscosity values presented in Table 1), (2) unlike the copolymer composites, the terpolymer nanocomposites exhibit melting transition and crystallization behaviour, as well as higher thermal stability due to the formation of more compact structures, (3) terpolymer nanocomposite containing IA unit shows higher thermal behaviour as compared with MA containing nanocomposite due to the effect of strong H-bonding (Figure 3) in the interlamellar terpolymerization, and (4) the change in the content of BMA flexible linkages in terpolymer/DMDA-MMT nanocomposites significantly influence the thermal behaviour of the nanocomposites, and can be described as a function for the correlation of these important properties through *in situ* self-plasticization in the formation of nanostructure with given thermal parameters.

3.3. Dynamic mechanical behaviour as a function of nanostructure formation

Dynamic mechanical analysis (DMA) method allows us to determine the loss tanδ, the storage modulus (G') and the loss modulus (G'') as a function of temperature (Figure 8). The loss tanδ is equal to the ratio of G''/G', which exhibits a higher response to the chemical and physical structural changes and phase transitions of polymer system; the storage modulus G' is associated with the elastic modulus of the polymer or its composite; the loss modulus G'' is related to the energy loss (damping factor) as a result of the friction of polymer chain movement. It is known that the decrease of G' is less dependent on the temperature changes, and this process proceeds very slowly as a function of temperature in the polymer system due to increased polymer chain mobility and flexibility [46]. As seen from DMA curves, this process continues until the glass transition region is approached, and then, G' decreases rapidly. In this isothermal condition, both the loss modulus G'' and loss tanδ increase and go via a maximum. The glass transition temperature (T_g) is determined as the temperature at which a maximum of loss tanδ is observed. This is well known and is a more exact method for determination of T_g values of polymers and their composites [47]. The glass transition region of polymeric materials can be broadened and shifted through various chemical and physical means [48].

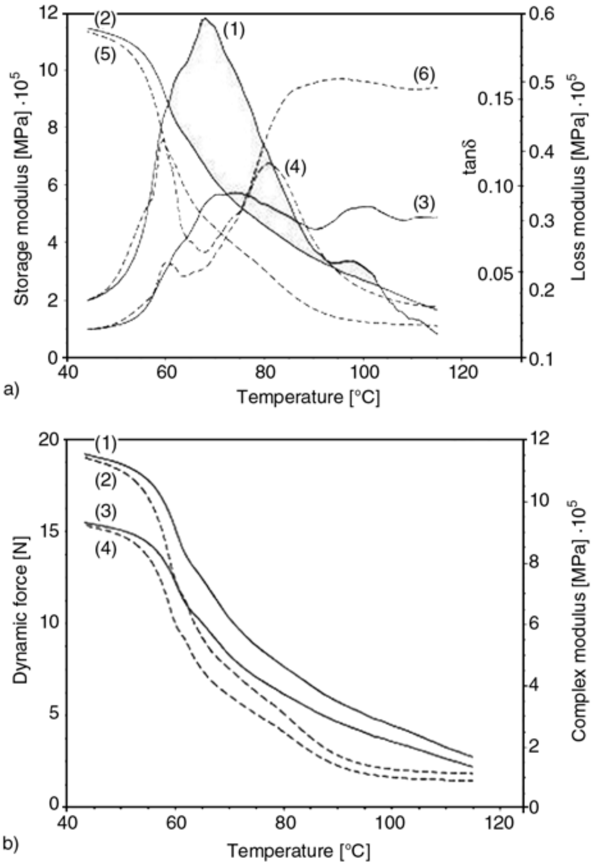

Figure 8. DMA curves of copolymer and its nanocomposite: (a) plots of (1 and 4) loss modulus (G''), (2 and 5) storage modulus (G') and (3 and 6) tanδ (G''/G'), and (b) (1 and 2) complex modulus and (3 and 4) dynamic force vs. temperature for poly(MA-*co*-BMA) (---) and poly(MA-*co*-BMA)/DMDA-MMT nanocomposite (—)

Masenelli-Varlot *et al.* [49] proposed an interpretation of the DMA spectra, according which the intensity of the interfacial adhesion strength directly influences the intensity of the reinforcement above the T_g. This principle can also be used to characterize the microstructure of functional (co)terpolymer/DMDA-MMT nanocomposite in terms of interfacial adhesion strength. Comparative DMA analysis of pure poly(MA-*co*-BMA) and poly(MA-*co*-BMA)/DMDA-MMT nanocomposites (Figure 8a) indicates the following changes of DMA curves when copolymer is intercalated between organo-silicate layers by interlamellar radical copolymerization: (1) increase of the elastic modulus by more than 7.1%, i.e., increase of the relaxation temperature from 58.3 up to 62.8°C, (2) increase of the glass transition behavior from 60.1 to 74.2°C, (3) unlike the pure copolymer, which has two peaks for the flexible BMA segments at 59.3°C and rigid MA units at 80.9°C, respectively, copolymer nanocomposite exhibits a single broad peak of higher intensity at 67.9°C; the significant increase in intensity of this peak indicates that relaxations of the flexible BMA segments decrease due to the increase of interfacial adhesion strength, i.e., the highest interaction occurs between anhydride units and organo-MMT. Plots of dynamic force (DF) and complex modulus (CM) vs. temperature are illustrated in Figure 8b. Observed significant difference (Δ) between these parameters [Δ = DF (nanocomposite)–DF(copolymer)] or [Δ = CM (nanocomposite)–CM(copolymer)] above T_g, related to the copolymer and its nanocomposite, can be described as a function of the formation of nano-structural architecture in poly(MA-*co*-BMA)/DMDA-MMT system. It can be proposed that Δ value is also associated with interfacial adhesion strength depending on the flexibility and hydrophobic/hydrophilic balance of the functional polymer chains and their ability to form interfacial complexes. The maximum values of Δ were observed around 85–95°C corresponding to the lower values of DF and CM parameters.

3.4. Nanostructure–XRD parameters relationship

The basal spacing (d_{001}) of copolymer, organo-MMT and nanocomposites were determined from XRD measurements. XRD patterns of studied systems are illustrated in Figures 9 and 10, and the obtained XRD parameters are summarized in Table 3. It is well known that organo-silicates exhibit an effective nucleation behaviour in the crystallization process and morphology formation of polymer nanocomposites [50, 51]; nanofillers can also change the crystallinity degree and crystallization rate, as well as provide the formation of thermodynamically stable crystalline phase in the polymer matrix [52, 53]. As seen from Figure 9, (co)terpolymers exhibit predominantly amorphous structure while their nanocomposites show characteristic semi-crystalline structure. IA-containing terpolymer nanocomposites (T-IA-NC) exhibit relatively higher crystallinity equal to 51% (Table 3). The position of the diffraction peaks, related to virgin amorphous (co)terpolymers, is not changed in the spectra of the (co)terpolymer/DMDA-MMT nanocomposites (Figure 10, Table 3). XRD patterns for the virgin DMDA-MMT clearly showed

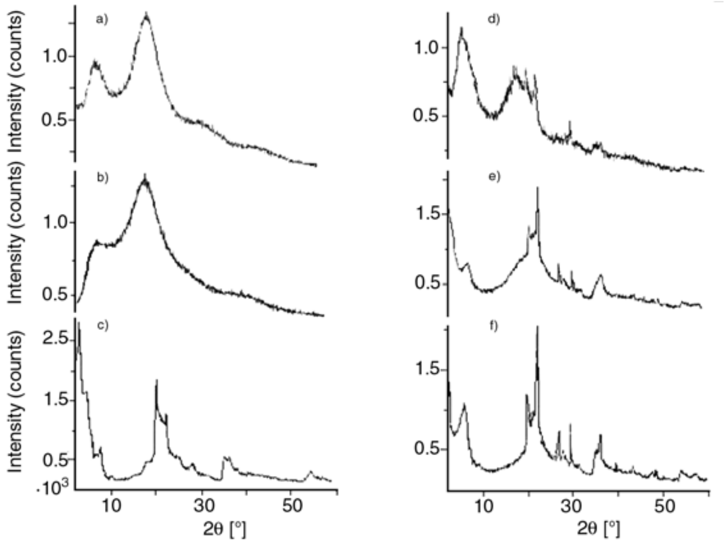

Figure 9. XRD patterns of (a) copolymer, (b) terpolymer-2, (c) pristine DMDA-MMT, (d) copolymer/DMDA-MMT, (e) terpolymer-2/DMDA-MMT, (f) terpolymer-IA/DMDA-MMT

Table 3. XRD parameters and crystallinity of the copolymer (C), terpolymers (T) and their nanocomposites (NCs)

C(T) and NCs	2θ [°]	d-spacing [Å]	Δd [Å]	Intensity (counts)	ED[a] [%]	Peak area (S)		χ_c[%]
						S_a	S_c	
C-1	6.74	13.10	0	1349	-	26208	4866	15.6
C-1-NC	2.22	35.68	17.73	1613	52.4	11250	2760	19.7
T-1	6.53	13.52	0	1271	-	20642	2137	9.4
T-1-NC	2.31	30.87	12.92	1688	53.4	16123	5092	24.0
T-2	6.92	12.76	0	1497	-	30517	4625	13.2
T-2-NC	2.58	34.22	16.27	1750	54.3	16606	6173	27.1
T-3	8.19	10.79	0	1310	-	32817	3737	10.2
T-3-NC	2.10	33.20	15.25	2069	58.4	9279	4447	32.4
T-IA-NC	2.04	44.14	26.19	2100	100	6712	6986	51.0
Pristine organo-MMT	2.78 4.92 7.38	31.75 17.95 11.97	– – –	2769 1475 750[b]	–	7217	10047	58.2

[a] ED (% exfoliation degree) values were calculated using the Equation (4)

[b] This peak disappears in the spectra of all the nanocomposites due to complete exfoliation

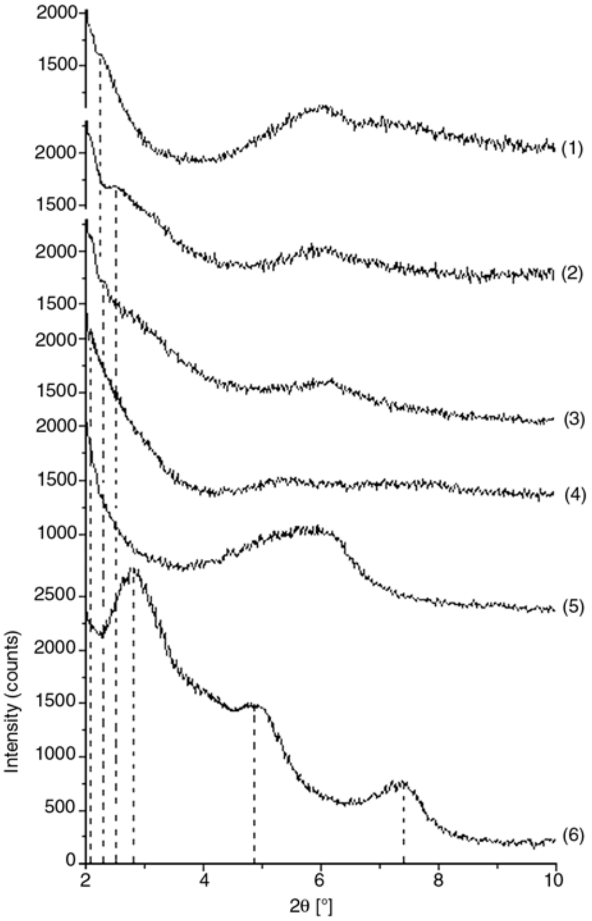

Figure 10. XRD patterns of nanocomposites:
(1) poly(MA-*co*-BMA)/DMDA-MMT,
(2) poly(MA-*alt*-S-*co*-BMA)-1/DMDA-MMT,
(3) poly(MA-*alt*-S-*co*-BMA)-2/DMDA-MMT,
(4) poly(MA-alt-S-co-BMA)-3/DMDA-MMT,
(5) poly(IA-*alt*-S-*co*-BMA)-1/DMDA-MMT
and (6) pristine DMDA-MMT

two broad diffraction peaks at 2.78° (*d*-spacing 31.75 Å) and 4.92° (*d*-spacing 17.95 Å) due to the d_{001} basal reflections, which disappear or significantly shift to lower 2θ regions in nanocomposites. The weak peak for the basal spacing (d_{001}) at 7.38° (11.97 Å) in DMDA-MMT pattern can be related to non-modified silicate plates. Usually this peak for pure MMT appears at 7.0 2θ (*d*-spacing 12.4 Å) [54]. Figure 10 shows the XRD patterns of organo-MMT itself and (co)terpolymer/DMDA-MMT nanocomposites containing 5 wt% of organo-MMT. The intense peak at $2\theta = 2.78°$ ($d = 31.75$ Å), relatively broad peak $2\theta = 4.92°$ ($d = 17.95$ Å) and peak with low intensity at $2\theta = 7.38°$ ($d = 10.97$ Å) in the pattern of DMDA-MMT, are associated with basal spacing for modified and small amount of non-modified silicate layers ($2\theta = 7.38°$), respectively. According to Mermut [55] and Önal [56], $d_{(001)}$ values scattered around 12–14, 14–18 Å and >18 Å are due to the monolayer, bilayer and pseudotrilayer alkyl ammonium configurations, respectively, in the 2:1 layers of organo-MMTs including Viscobent SB-1 [56]. In the case of nanocomposites (patterns 2–4), the original organo-MMT peaks at $2\theta = 7.38°$ disappear, and peaks at 2.78 and 4.92° shift to lower 2θ regions (for the co- and terpolymer nanocomposites, patterns 2, 4 and 6). As seen from Figure 10 and Table 3, these observed changes clearly indicate the significant increase of interlamellar distance ($\Delta d = d_{nc} - d_0 >$ 15 Å) due to *in situ* processing through complex formation or H-bonding between anhydride/acid groups and surface alklammonium cations. This can also produce a driving force necessary for the effective intercalation/exfoliation. The interlamellar complex-formation and (co)terpolymerizaton reactions easily proceed onto alkyl amine modified silicate layers, after ending of which can also proceed onto non-modified silicate layers. In the latter case, anhydride (or carboxylic group which occurs by the hydrolysis of the MA unit) and acid (IA) monomers and their (co)terpolymers can also form interlamellar complexes with the non-modified silicate layers containing oxygen atoms and hydroxyl groups through strong H-bonding [8].

It was observed that the exfoliation degree (ED) depends on the type of alkyl amine configuration, i.e., on the degree of intensity change of basal *d*-spacing peaks. Taking into consideration the three basal peak intensities for the organo-MMT before (I_0) and after interlamellar (co)terpolymerizations (I_e), the values of intercalation/exfoliation degree (ED %) were calculated, and obtained results were presented in Table 3. The peak with weak intensity at 7.38° (*d*-spacing 11.97 Å for non-modified 2:1 layers) disappears in the XRD spectra for all the nanocomposites (Figure 8) due to the complete exfoliation process. This observed fact confirms the above mentioned proposed mechanism. It was also observed that the crystallinity of the (co)terpolymers/DMDA-MMT nanocomposites depends on the degree of exfoliation. Relatively high crystalline copolymer-NC and terpolymer-IA-NC exhibit higher values of ED (Table 3). A visible increase in ED for terpolymer-MA-NC nanocomposites increases the crystallinity of these NCs. This phenomenon may be explained by the effect of complex formation between functional polymer chains and organo-silicate layers on the local chain folding and crystallization process in the (co)terpolymer matrix. The ED values visibly increase with increasing content of the flexible BMA linkages in terpolymer-MA-NCs, in spite of the decreasing content of the complex-forming anhydride/acid units. This fact can be explained by self-plasticization effect of side-chain *n*-butylester groups in terpolymers that increases the dispersion of the organo-MMT into matrix.

3.5. Surface morphology of nanocomposites

Figure 11 shows the SEM image of the terpolymers containing different amounts of BMA units and their nanocomposites prepared by interlamellar copolymerization. SEM images of this hybrid composites inferred that the size of the particles significantly depends on the content of flexible BMA linkages and type of interfacial interaction. The increase of BMA content in terpolymers provides the facile exfoliation of polymer chains into

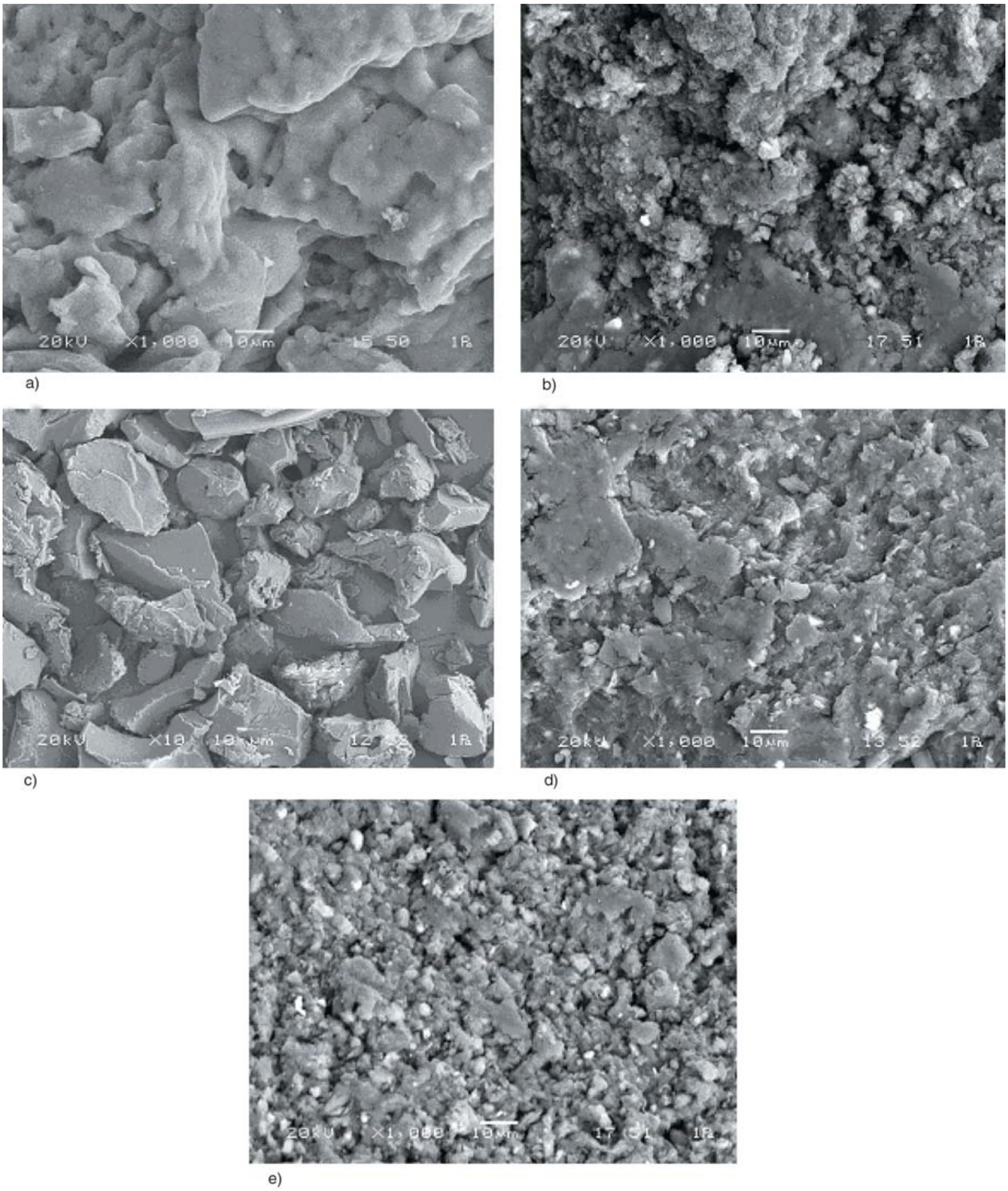

Figure 11. SEM patterns of (a) terpolymer-2, (b) terpolymer-2/DMDA-MMT, (c) terpolymer-3, (d) terpolymer-3/DMDA-MMT and (e) terpolymer-IA/DMDA-MMT

DMDA-MMT galleries and formation of relatively high dispersed particles. In the case of poly(IA-*co*-S-BMA)/DMDA-MMT nanocomposite (e), the formation of well dispersed particles was observed due to the strong H-bonding between free carboxylic acid of IA monomer or terpolymer chain and alkyl amine on the silicate layers.

4. Conclusions

This work has attempted to develop novel polymer layered silicate nanocomposites by complex-radical interlamellar (co)terpolymerization of intercalated MA…DMDA-MMT and IA…DMDA-MMT monomer complexes with S and BMA. It was shown that the intercalation/exfoliation behaviour of functional (co)terpolymers, and therefore, the formation of nano-structure in the studied systems depend on the hydrophilic/hydrophobic balance in amphiphilic terpolymers, amount of flexible BMA linkages and interlayer complex-formation between anhydride/acid units and surface alkylammonium fragments (Figure 1). The comparative analysis of structure–composition–property relationship of the virgin (co)terpolymers and their nanocomposites showed significant increase in the thermal and dynamic mechanical behaviour and crystallinity of synthesized nanocomposites due to the homogeneous dispersion of the silicate nano-galleries in the functional (co)terpolymer matrix. Unlike amorphous virgin (co)terpolymers the nanocomposites exhibit crystallization behaviour and considerably improved thermal properties depending on the structure (presence of anhydride or acid moieties) and composition of terpolymers, especially on the content of flexible side-chain *n*-butylester linkages. The significant increase in *d*-spacing (intergallery distance) and degree of exfoliation indicates the formation of nano-structure in the studied (co)terpolymer/DMDA-MMT systems. Obtained results show that the formation of nanoarchitectures in the studied (co)terpolymer/DMDA-MMT systems predominantly proceeds through interlamellar complex-formation and *in situ* intercalation/exfoliation processing.

Synthesized polymer hybrids may be also used as reactive compatibilizer-nanofillers for the thermoplastic polymer blends, especially for the acrylic and styrene polymer-based systems, and to prepare the various nanomaterials in melt by reactive extrusion *in situ* processing. This will be a subject of our future investigations.

Acknowledgements

This study was carried out in according to the Polymer Science and Engineering Program of the Chemical Engineering Department, Hacettepe University (HU). The support of the TÜB?TAK (Turkish National Scientific and Technical Research Council) through TBAG-HD/249-107T238 project is gratefully acknowledged.

References

[1] Alexandre M., Dubois P.: Polymer-layered silicate nanocomposites: Preparation, properties and uses of a new class of materials. Material Science and Engineering: Reports, **28**, 1–63 (2000).

[2] Sinha Ray S., Okamoto M.: Polymer/layered silicate nanocomposites: A review from preparation to processing. Progress in Polymer Science, **28**, 1539–1641 (2003).

[3] Moniruzzaman M., Winey K. I.: Polymer nanocomposites containing carbon nanotubes. Macromolecules, **39**, 5194–5205 (2006).

[4] Rzaev Z. M. O., Yilmazbayhan A., Alper E.: A one-step preparation of compatibilized polypropylene-nanocomposites by reactive extrusion processing. Advances in Polymer Technology, **26**, 41–55 (2007).

[5] Utracki L. A., Sepehr M., Boccaleri E.: Synthesic, layered nanoparticles for nanocomposites (PNCs). Polymers for Advanced Technology, **18**, 1–37 (2007).

[6] Krawczak P.: Compounding and processing of polymer nanocomposites: From scientific challenges to industrial stakes. Express Polymer Letters, **1**, 188–188 (2007).

[7] Da Z. L., Zhang Q. Q., Wu D. M., Yang D. Y., Qiu F. X.: Synthesis, characterization and thermal properties of inorganic-organic hybrid. Express Polym Letters, **1**, 698–703 (2007).

[8] Kawasumi M., Hasegawa N., Kato M., Usuki A., Okada A.: Preparation and mechanical properties of polypropylene-clay hybrids. Macromolecules, **30**, 6333–6338 (1997).

[9] Okada A., Usuki A.: The chemistry of polymer-clay hybrids. Material Science and Engineering, part C: Biomimetic Materials, Sensors and Systems, **3**, 109–115 (1995).

[10] Messersmith P. B., Giannelis E. P.: Synthesis and barrier properties of poly(ε-caprolactone)-layered silicate nanocomposites. Journal of Polymer Science, Part A: Polymer Chemistry, **33**, 1047–1057 (1995).

[11] Burnside S. D., Gianellis E. P.: Synthesis and properties of new poly(dimethylsiloxane) nanocomposites. Chemistry of Materials, **7**, 1597–1600 (1995).

[12] Liu Y-L., Wu C-S., Chiu Y-S., Ho W-H.: Preparation, thermal properties, and flame retardance of epoxy-silica hybrid resins. Journal of Polymer Science, Part A: Polymer Chemistry, **41**, 2354–2367 (2003).

[13] Tang Y., Hu Y., Wang S. F., Gui Z., Chen Z., Fan W. C.: Preparation and flammability of ethylene-vinyl acetate copolymer/montmorillonite nanocomposites. Polymer Degradation and Stabilization, **78**, 555–559 (2002).

[14] Yeh J-M., Liou S-J., Lai C-Y., Wu P-C.: Enhancement of corrosion protection effect in polyaniline via the formation of polyaniline-clay nanocomposite materials. Chemistry of Materials, **13**, 1131–1136 (2001).

[15] Yeh J-M., Liou S-J., Lin C-Y., Cheng C-Y., Chang Y-W., Lee K-R.: Anticorrosively enhanced PMMA-clay nanocomposite materials with quaternary alkylphosphonium salt as an intercalating agent. Chemistry of Materials, **14**, 154–161 (2002).

[16] Doh J. G., Cho I.: Synthesis and properties of polystryrene-organoammonim montmorillonite hybrid. Polymer Bulletin, **41**, 511–518 (1998).

[17] Zeng Q. H., Wang D. Z., Lu G. Q.: Synthesis of polymer-montmorillonite nanocomposites by in situ intercalative polymerization. Nanotechnology, **13**, 549–553 (2002).

[18] Liu G., Zhang L., Zhao D., Qu X.: Bulk polymerization of styrene in the presence of organomodified montmorillonite. Journal of Applied Polymer Science, **96**, 1146–1152 (2005).

[19] Biswas M., Sinha Ray S.: Preparation and evaluation of composites from montmorillonite and some heterocyclic polymers. 1. Poly(*N*-vinylcarbazole)-montmorillonite nanocomposite system. Polymer, **39**, 6423–6428 (1998).

[20] Friedlander H. Z.: Spontaneous polymerization in and on clay. ACS Division Polymer Chemistry Reprints, **4**, 300–306 (1963).

[21] Di J., Sogah D. Y.: Intergallery living polymerization using silicate-anchored photoiniferter. A versatile preparatory method for exfoliated silicate nanocomposites. Macromolecules, **39**, 1020–1028 (2006).

[22] Stadtmueller L. M., Ratinac K. R., Ringer S. P.: The effect of intragallery polymerization on the structure of PMMA-clay nanocomposites. Polymer, **46**, 9574–9584 (2005).

[23] Li H-M., Chen H-B.: Synthesis and characterization of poly(*N*-n-butylmaleimide)-clay nanocomposites. Material Letters, **57**, 3000–3004 (2003).

[24] Yan-wu Z., Jun-qing J.: Preparation of low-molecular-weight polyamide 6/hydrotalcite intercalated nanocomposites via in situ polymerization. Express Polymer Letters, **1**, 98–103 (2007).

[25] Vaysse C., Guerlou-Demourgues L., Delmas C., Duguet E.: Tentative mechanisms for acrylate intercalation and in situ polymerization in nickel-based layered double hydroxides. Macromolecules, **37**, 45–51 (2004).

[26] Vaysse C., Guerlou-Demourgues L., Duguet E., Delmas C.: Acrylate intercalation and in situ polymerization in iron-, cobalt-, or manganese-substituted nickel hydroxides. Inorganic Chemistry, **42**, 4559–4567 (2003).

[27] Vieille L., Moujahid E. M., Taviot-Gueho C., Cellier J., Besse J-P., Leroux F.: In situ polymerization of interleaved monomers: A comparative study between hydrotalcite and hydrocalumite host structures. Journal Physical Chemistry of Solids, **65**, 385–393 (2004).

[28] Cao C., Huang F., Cao C. T., Li J., Zhu H.: Synthesis of carbon nitride nanotubes via a catalytic-assembly solvothermal route. Chemistry of Materials, **16**, 5213–5215 (2004).

[29] Yu F., Yao K., Shi L., Wan W., Zhong Q., Fu Y., You X.: Investigation of acrylic acid polymerization in novel two-dimensional space with regular amino groups of layered aminipropylsilica. Chemistry of Materials, **19**, 3412–3418 (2007).

[30] Xu M. Z., Coi Y. S., Kim Y. K., Wang K. H., Chung I. J.: Synthesis and characterization of exfoliated poly(styrene-*co*-methyl methacrylate)/clay nanocomposites via emulsion polymerization with AMPS. Polymer, **44**, 6387–6395 (2003).

[31] Noh M. H., Jang L. W., Lee D. C.: Intercalation of styrene-acrylonitrile copolymer in layered silicate by emulsion polymerization. Journal of Applied Polymer Science, **74**, 179–188 (1999).

[32] Liu G., Zhang L., Gao C., Qu X.: Copolymerization of styrene with *N*-phenyl maleimide in the presence of montmorillonite. Journal of Applied Polymer Science, **98**, 1932–1937 (2005).

[33] Liu J.-H., Zhang J., Li F.: Flame retardancy of styrene and butyl acrylate/montmorillonite nanocomposites. Polymer Material Science and Engineering, **21**, 156–159 (2005).

[34] Al-Esaimi M. M.: Reaction catalyzed by montmorillonite: Polymerization of methyl methacrylate. Journal of Applied Polymer Science, **64**, 367–372 (1997).

[35] Liu G-D., Li X., Zhang L-C., Qu X-G., Liu P., Yang L., Gao C-H.: Thermal analysis of solution copolymers of styrene with *N*-phenylmaleimide. Journal of Applied Polymer Science, **83**, 417–422 (2002).

[36] Wang D., Zhu J., Yao Q., Wilkie C. A.: A comparison of various methods for the preparation of polystyrene and poly(methyl methacrylate) clay nanocomposites. Chemistry of Materials, **14**, 3837–3843 (2002).

[37] Wang D., Zhu J., Yao Q., Wilkie C. A.: In-situ reactive blending to prepare polystyrene-clay and polypropylene-clay nanocomposites. Polymer Degradation and Stability, **80**, 171–182 (2003).

[38] Rzaev Z. M. O., Guner A., Can H. K., Aşici A.: Reaction of some anhydride-containing copolymers with γ-aminopropyltriethoxysilane. Polymer, **42**, 5599–606 (2001).

[39] Can H. K., Rzaev Z. M. O., Güner A.: Synthesis and characterization of new hydrogels on the basis of water-soluble maleic anhydride copolymers with γ-aminopropyltriethoxysilane. Journal of Applied Polymer Science, **90**, 4009–4015 (2003).

[40] Rzayev Z. M. O.: Nanotechnology methods in polymer engineering. in '4th Nanoscience and Nanotechnology Conference Proceedings, Ankara, Turkey' 154 (2007).

[41] Rabek J. F.: Experimental methods in polymer chemistry. Wiley, New York (1980).

[42] Figueruelo J. E., García-Lopera R., Monzó I. S., Abad C., Campos A.: Determination of χ from liquid-liquid phase data in ternary polymer systems (solvent/polymer/polymer) with hydrogen bonding. Express Polymer Letters, **2**, 313–329 (2008).

[43] Cowie J. M. G.: Alternating copolymers. Plenum, New York (1985).

[44] Hendricks S. B.: Base exchange of the clay mineral montmorillonite for organic cations and its dependence upon adsorption due to van der Waals forces. Journal of Physical Chemistry, **45**, 65–81 (1941).

[45] Sun S. F.: Physical chemistry of macromolecules. John Wiley and Sons, New Jersey (2004).

[46] Gong X., Liu J., Baskaran S., Voise R. D., Young J. S.: Surfactant-assisted processing of carbon nanotube/polymer composites. Chemistry of Materials, **12**, 1049–1052 (2000).

[47] Mark H. F., Bikales N. M., Overberger C. C., Menges G.: Encyclopedia of polymer science and engineering. John Wiley and Sons, New York (1987).

[48] Sperling L. H.: Introduction to physical polymer science. John Wiley and Sons, New York (1992).

[49] Masenelli-Varlot K., Vigier G., Vermogen A., Gauthier C., Cavaille J. Y.: Quantitative structural characterization of polymer-clay-nanocomposites and discussion of an 'ideal' microstructure, leading to the highest mechanical reinforcement. Journal of Polymer Science, Part B: Polymer Physics, **45**, 1243–1351 (2007).

[50] Fornes T. D., Paul D. R.: Crystallization behavior of nylon 6 nanocomposites. Polymer, **44**, 3945–3961 (2003).

[51] Harrats C., Groeninckx G.: Features, questions and future challenges in layered silicates clay nanocomposites with semicrystalline polymer matrice. Macromolecular Rapid Communication, **29,** 14–26 (2008).

[52] Lewin N. H., Pearce M. E., Levon K., Mey-Maron A., Zammarano M., Wilkie C. A., Jang B. N.: Nanocomposites at elevated temperatures: Migration and structural changes. Polymers for Advanced Technology, **17**, 226–234 (2006).

[53] Ajayan M., Schadler L. S., Braun P. V.: Nanocomposite science and technology. Wiley-VCH, Weinheim (2003).

[54] Cho J. M., Paul D. R.: Nylon 6 nanocomposites by melt compounding. Polymer, **42**, 1083–1094 (2001).

[55] Mermut A. R.: Layer charge characteristics of 2:1 silicate clay minerals. The Clay Mineral Society, Aurora (1994).

[56] Önal M.: Examination of some commercial sorptive organobentonites. Turkish Journal of Chemistry, **31**, 579–588 (2007).

eXPRESS Polymer Letters Vol.2, No.9 (2008) 655–664
Available online at www.expresspolymlett.com
DOI: 10.3144/expresspolymlett.2008.78

Enhancement of properties of PA6/PP nanocomposites via organic modification and compatibilization

Kusmono[1], *Z. A. Mohd Ishak*[1*], *W. S. Chow*[1], *T. Takeichi*[2], *Rochmadi*[3]

[1]School of Materials and Mineral Resources Engineering, Engineering Campus, Universiti Sains Malaysia, 14300 Nibong Tebal, Pulau Pinang, Malaysia
[2]Department of Materials Science, Toyohashi University of Technology, Toyohashi 441-8580, Japan
[3]Department of Chemical Engineering, Gadjah Mada University, Jln. Grafika 2 Yogyakarta, Indonesia

Received 12 May 2008; accepted in revised form 6 August 2008

Abstract. Nanocomposites based on polyamide 6/polypropylene (PA6/PP = 70/30) blend containing organophilic montmorillonite (OMMT) and maleated polypropylene (PP-g-MA) as compatibilizer were prepared by melt compounding followed by injection molding. Modification of montmorillonite (MMT) with dodecyalmine was successfully performed. The morphological and mechanical properties of nanocomposites were investigated by using x-ray diffraction (XRD), transmission electron microscopy (TEM), tensile, flexural, and impact tests. The thermal stability of nanocomposites was characterized by using thermogravimetric analysis (TGA) and heat distortion temperature (HDT). XRD and TEM results indicated that the intercalated structure was obtained for PA6/PP/MMT composite, a mixture of intercalated and exfoliated structures for PA6/PP/OMMT nanocomposite, and exfoliated structure for PP-g-MA compatibilized PA6/PP/OMMT nancomposite. Thermal stability and HDT of PA6/PP matrix were improved by the addition of both MMT and OMMT. The introduction of PP-g-MA into the PA6/PP/OMMT nanocomposite enhanced the properties such as stiffness, strength, ductility, impact strength, and HDT. This was attributed to the compatibilizing effect of PP-g-MA which improved interfacial adhesion between OMMT with PA6/PP matrix and also promoted the degree of exfoliation of silicate layers in the PA6/PP matrix.

Keywords: *nanocomposites, polyamide 6, polypropylene, OMMT, PP-g-MA*

1. Introduction

Blends of polyamide 6 (PA6) and polypropylene (PP) have received much attention over recent years, since they combine thermomechanical characteristics of the former with the ease of processing of the latter. Unfortunately, these polymers are incompatible because of their different polarity and crystalline morphologies [1]. Therefore, compatibilizing agent has to be used to reduce the interfacial tension and to improve the adhesion between two constituents. Maleated PP (PP-g-MA) has well been documented as one of the most effectively compatibilizing agents for PA6/PP blends [2, 3].

Compounding polymers with inorganic materials has long been an interesting topic of scientific research and industrial applications, because inorganic materials can be employed to improve the mechanical properties, provide enhanced barrier properties and reduce the flammability of the resultant polymer composites [4]. Among various inorganic fillers, montmorillonite clay with large aspect ratios has proven to be particularly effective in polymer matrix reinforcement [5]. However, pristine MMT layers are not easily exfoliated in most polymers due to the strong electrostatic forces between them and to the chemical incompatibility

---

[*] Corresponding author, e-mail: zarifin.ishak@googlemail.com

Table 1. Designation and composition of samples

Sample designation	Composition	Parts [phr]
PA6/PP	PA6/PP	70/30
PA6/PP/PP-g-MA	PA6/PP/PP-g-MA	70/30/5
PA6/PP/MMT	PA6/PP/MMT	70/30/4
PA6/PP/OMMT	PA6/PP/Dodecylamine modified MMT	70/30/4
PA6/PP/OMMT/PP-g-MA	PA6/PP/Dodecylamine modified MMT/PP-g-MA	70/30/4/5

of the MMT surface with polymers. Long-chain alkyl ammonium surfactants were usually employed to pre-modify the MMT interlayer galleries through cation exchange reactions so as to weaken the interaction between adjacent layers and to enhance the compatibility/wettability of the MMT layer with the polymer matrix [6]. Dodecylamine is one of most popular alkyl ammonium surfactants and has been widely employed for preparation of polymer nanocomposites. The dodecylamine modified MMT improved the mechanical properties for nanocomposites based on PA6 [7] and PP [8]. Recently, nanocomposites based on PA6/PP blends have been extensively studied by many researchers [9, 10]. Most of them prepared PA6/PP nanocomposites using a commercial organoclay. To our knowledge, the application of organic modification of MMT such as the dodecylamine modified MMT for PA6/PP nanocomposites was still limited.

In this work, nanocomposites based on PA6/PP blends (PA6/PP = 70/30) were prepared by melt compounding using a co-rotating twin screw extruder followed by injection molding. The dodecylamine modified montmorillonite and PP-g-MA were used as reinforcement and compatibilizer, respectively. The influence of organic modification and compatibilizer on the morphological and mechanical properties of PA6/PP/OMMT nanocomposites was investigated by using X-ray diffraction (XRD), transmission electron microscopy (TEM), tensile, flexural, and impact tests. In addition, thermal stability was also characterized by thermogravimetric analysis (TGA) and heat distortion temperature tests.

2. Experimental

2.1. Materials

PA6 (Amilan CM 1017) used in this study was a commercial product of Toray Nylon Resin AMILAN, Japan. The melt flow index or MFI (at 230°C and 2.16 kg load) and density of PA6 were 35 g/10 min and 1.14 g/cm^3, respectively. PP (Pro-Fax SM-240) was purchased from Titan Himont Polymer (M) Sdn. Bhd., Malaysia. The MFI (at 230°C and 2.16 kg load) and density of PP were 25 g/10 min and 0.9 g/cm^3, respectively. Polypropylene grafted with 1.2 wt% of maleic anhydride (Polybond 3200) was purchased from Uniroyal Chemical, Middlebury. Kunipia-F, sodium montmorillonite (MMT) clay with cation exchange capacity (CEC) of 119 meq/100 g, was supplied by Kunimine Industry Co., Japan. The alkyl ammonium salt used to modify Na-MMT clay was dodecylamine [$CH_3(CH_2)_{11}NH_2$], supplied from Kishida Chemical Co., Osaka Japan. The designation and composition of samples tested are given in Table 1.

2.2. Preparation of OMMT

Organophilic montmorillonite (OMMT) was prepared by cation exchange of MMT with dodecylamine according to a method reported by Agag and Takeichi [11]. Dodecyl ammonium chloride solution was prepared by the addition of 4.17 g of conc. HCl (40 mmol) to 7.41 g of dodecylamine (40 mmol) in 1000 ml of distilled water. The mixture was stirred at 80°C until a clear solution was obtained, indicating the formation of dodecyl ammonium chloride. To this solution, a suspension of 20 g of MMT in 1000 ml of distilled water was added; the mixture was mechanically stirred at 80°C for 5 hours. The obtained white precipitate was collected by suction filtration and then washed by hot water to remove salt. This process was repeated several times until no chloride was detected in the filtrate by 0.1 N $AgNO_3$. The resultant precipitate was air-dried, ground in mortar, sieved to obtain powders, and finally dried in an air-blowing oven at 110°C for 3 days, affording white powder. The modified MMT was termed OMMT.

2.3. Sample preparation

PA6/PP/OMMT nanocomposites were prepared in a co-rotating intermeshing twin-screw extruder (BERSTORFF ZE 25, Germany) at temperature ranging from 230 to 240°C and at a screw speed of 70 rpm. The extrudates were then injection-molded into standard tensile (ASTM D638 type I) and flexural specimens (ASTM D790) using an injection molding machine (Haitian HTF160X, China). The barrel zone temperatures were set at 190, 235, 250, 255, 260, and 250°C and a mold temperature of 110°C. Prior to extrusion and injection molding, all pellets and clay were dried in an oven at 80°C for 15 hours.

2.4. Characterization and mechanical testing

Fourier transform infra-red spectroscopy (FT-IR) analysis of MMT and OMMT were performed on JASCO spectrophotometer model FT/IR-420, Japan. About 2 mg of sample was mixed with 200 mg of potassium bromide (KBr) prior to compacting into thin pellets with a hydraulic press. FTIR spectra were obtained from KBr pellets at wave numbers from 400–4000 cm^{-1}. X-ray diffraction measurements were conducted directly from MMT and OMMT powders while for the nanocomposites were carried out on bars. All these experiments were performed in reflection mode with a D5000 diffractometer (Siemens, Germany) using CuK_α radiation at a scan rate of 0.3°/min in a 2θ range of 2–10°, and operated at 30 kV and 20 mA. TEM measurements were carried out with a JEOL JEM-200CX TEM (Japan) operating at an accelerating voltage of 200 kV. The specimens were prepared using a Leica Ultracut UCT ultramicrotome. Ultra-thin sections of about 60 nm in thickness were cut with a Diatome diamond knife (35°) at room temperature.

The thermal stability of samples was studied using thermogravimetric analysis (TGA; Perkin-Elmer TGA-6, USA). The sample was heated from room temperature to 600°C at 10°C/min under nitrogen atmosphere. Heat distortion temperature (HDT) of samples was measured using specimens having dimensions 125×12.50×3.0 mm^3 according to ASTM D 648. The test was conducted at a heating rate of 2°C/min and a fiber stress of 1.8 MPa using a 4 Station Advanced HDT/Vicat Softening Point Apparatus (Ray-Ryan Test Equipment Ltd, UK).

Tensile and flexural tests were performed on a universal testing machine (Instron 3366, USA) at room temperature according to ASTM D638 type I and ASTM D790, respectively. Tensile test was conducted at a crosshead speed of 50 mm/min. For flexural test, a three-point bending configuration was selected with a support span length of 50 mm and a crosshead speed of 3 mm/min. Izod impact test was carried out on notched specimens using a Pendulum Hammer Impact 25 S/N V67R (Galdabini, Italy) according to ASTM 256-02 with a impact speed of 3.46 m/s.

3. Results and discussion

3.1. FT-IR analysis

Figure 1 shows the FT-IR spectra of MMT and OMMT. The absorption peaks at 3629, 1643, 1043, 914, and 521 cm^{-1} correspond to –OH stretching, –OH bending, Si–O stretching, –OH bending, and Si–O bending, respectively, which are characteristic absorption bands of MMT. In addition to those peaks, OMMT also exhibits peaks at 3251 and 2920 cm^{-1} corresponding to N–H stretching and $–CH_3$ stretching, respectively, while peaks at both 2850 and 1469 corresponds to $–CH_2$ stretching. This indicates that dodecylammoniun has been intercalated into the galleries of MMT by a cation exchange reaction.

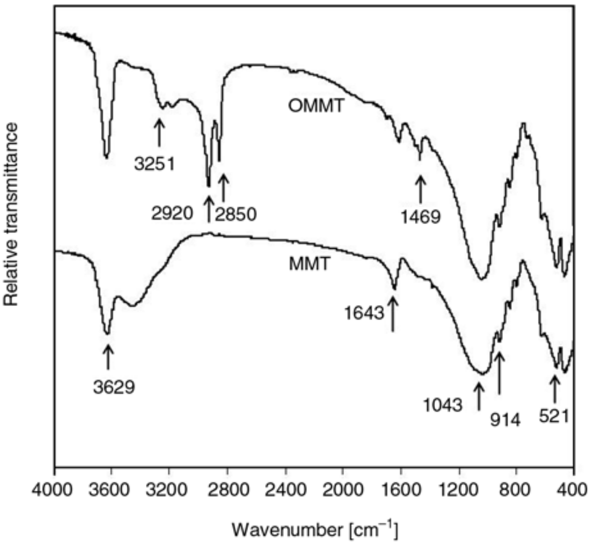

Figure 1. FT-IR spectra of MMT and OMMT

3.2. XRD

Figure 2 presents the XRD patterns of MMT and OMMT. MMT and OMMT depict the characteristic diffraction peaks at $2\theta = 7.12$ and 5.44° corresponding to basal spacing (d_{001}) of 1.24 and 1.62 nm, respectively. Thus, OMMT exhibits a larger basal spacing than MMT. The expanded basal spacing suggests that the dodecylammonium has intercalated into the galleries of MMT, which is in agreement with the FT-IR results discussed earlier. The increase in basal spacing also indicates the successful modification of MMT through a cation exchange reaction.

Figure 3 shows the XRD patterns of PA6/PP blends and its nanocomposites. After incorporating of the MMT into PA6/PP matrix by melt compounding, the diffraction peak of MMT shifts to $2\theta = 6.29°$, with a basal spacing of 1.40 nm, indicating a slight increase in basal spacing. This suggests the polymer molecular chains have entered into the galleries of MMT and the intercalated structure is formed in the PA6/PP/MMT composite. In the XRD pattern of PA6/PP/OMMT nanocomposite, a broad shoulder peak appears at $2\theta = 2.99°$ corresponding to a basal spacing of 2.95 nm. The presence of a broad shoulder peak probably indicates the formation of a mixture of intercalated and exfoliated structures in the PA6/PP/OMMT nanocomposites [4]. After introduction of PP-g-MA into PA6/PP/OMMT, the diffraction peak of OMMT disappears in the XRD pattern of PA6/PP/OMMT/PP-g-MA nanocomposite. The absence of diffraction peak indicates the formation of exfoliated structure in the nanocomposite [4]. Thus, the presence of PP-g-MA in the PA6/PP/OMMT has promoted the dispersion and exfoliation of OMMT in the PA6/PP matrix. This may be attributed to the strong hydrogen-bonding interaction between maleic anhydride group in PP-g-MA and amine group in organic modifier of organoclay. This leads the expansion of interlayer spacing and further weakening of the interaction between the silicate layers. Furthermore, it will facilitate the intercalation of polymer matrix chains into the silicate galleries and results in the formation of the exfoliated structure [12].

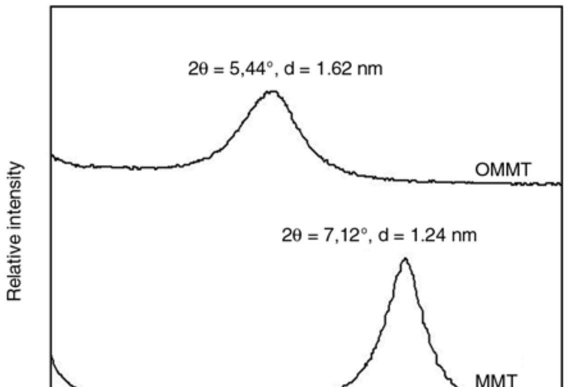

Figure 2. XRD patterns of MMT and OMMT

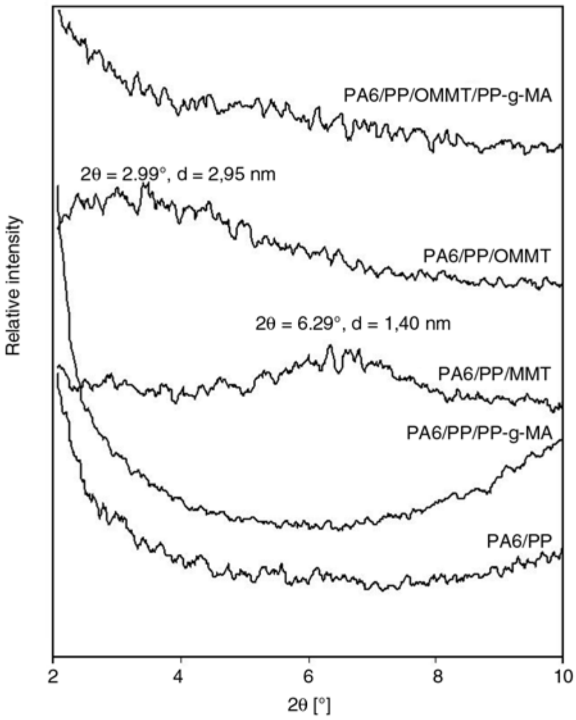

Figure 3. XRD patterns of PA6/PP blends and its nanocomposites

3.3. TEM

Figures 4–6 display the TEM images of PA6/PP/MMT, PA6/PP/OMMT, and PA6/PP/OMMT/PP-g-MA nanocomposites, respectively. The dark lines represent the intersection of silicate layers whereas the gray background corresponds to PA6 phase. A poor dispersion of clay platelets, i.e. intercalated clay layers stacks and large clay aggregates can be observed in the TEM image of PA6/PP/MMT composite (cf. Figure 4). This may be attributed to the presence of strong electrostatic forces between clay layers [6]. The most exfoliated silicate layers and

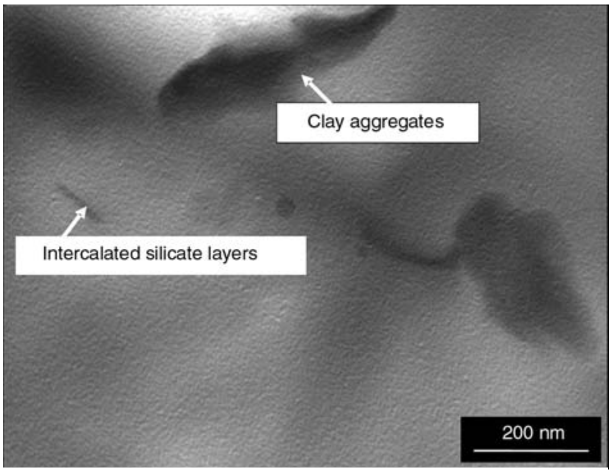

Figure 4. TEM image of PA6/PP/MMT composite

few intercalated clay layers stacks are observed in the PA6/PP/OMMT nanocomposite (cf. Figure 5). This suggests the formation of a mixture of intercalated and exfoliated structures in the nanocomposite. For PA6/PP/OMMT/PP-g-MA nanocomposite (cf. Figure 6), the individual silicate layers are homogenously dispersed in the PA6 phase, hence suggesting the formation of exfoliated structure. Accordingly, the presence of PP-g-MA in the PA6/PP/OMMT nanocomposite promoted the dispersion and exfoliation of silicate layers in the PA6 phase. When PA6/PP matrix, OMMT, and PP-g-MA were mixed together, PP-g-MA could easily penetrate the interlayer of organoclay. The driving force for intercalation originates from the strong hydrogen bonding between maleic anhydride groups in PP-g-MA and amine groups in organoclay and leads to the expansion of interlayer spacing and a further weakening of interactions between the silicate layers [12]. This facilitates the intercalation of PA6 chains into silicate galleries and resulted in the formation of the exfoliated structure as confirmed by XRD results earlier. The better dispersion obtained by the addition of compatibilizer was also found by Pegoretti *et al.* [13] for PE-g-MA compatibilized PE/clay nanocomposites. Furthermore, the white particle dispersed in the PA6 phase corresponds to the PP phase without silicate layers inside (cf. Figures 5 and 6). The strong tendency of silicate layers to be located in the PA6 phase could be attributed to the fact that the silicate layers has a higher affinity to the more polar PA6 phase instead of PP phase. This is in agreement with our previous works on nanocomposites based on PA6 matrix [14] and PA6/PP blend [15] whereby AFM was used to prove the affinity of nanoclays to PA6 phase.

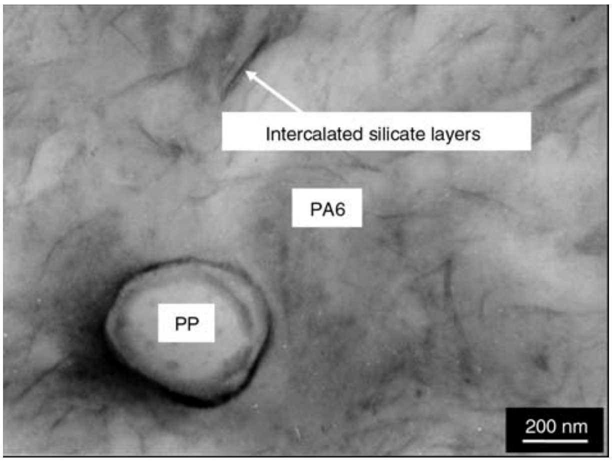

Figure 5. TEM image of PA6/PP/OMMT nanocomposite

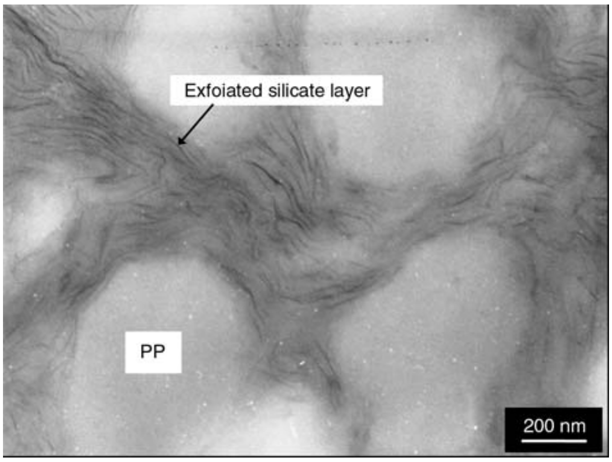

Figure 6. TEM image of PA6/PP/OMMT/PP-g-MA nanocomposite

3.4. TGA

Figure 7 shows the TGA curves of MMT and OMMT. Below 100°C, MMT exhibits a relatively higher weight loss than OMMT corresponding to the removal of water from interlayer coordinated to Na^+. At this temperature, the weight loss for OMMT is lower because of the organophilic properties of OMMT containing alkyl ammonium ions [12]. The weight loss observed at 100–600°C for MMT may be attributed to the decomposition of hydrogen-bonded water molecules and some of the OH group from tetrahedral sheets [16]. On other hand, the greater weight losses displayed by OMMT in this temperature range could be explained mainly by the decomposition of intercalated ammonium and partly by the adsorbed water

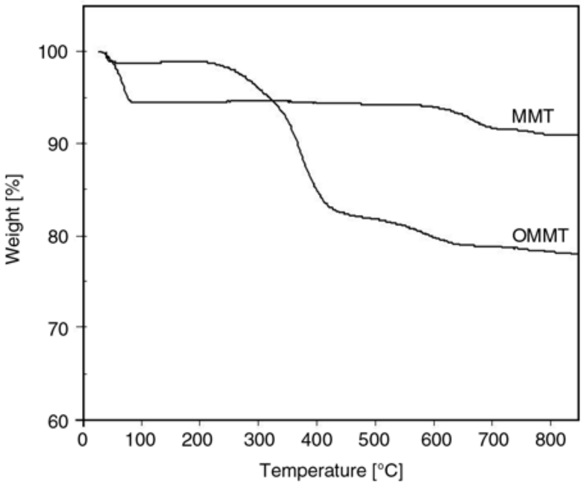

Figure 7. TGA curves of MMT and OMMT

molecules below 220°C [17]. In the temperature range of 600–850°C, the weight losses for MMT and OMMT was probably associated with the dehydroxylation of MMT [18].

Figure 8 displays the TGA curves of PA6/PP blends and its nanocomposites. It can be seen that all samples displayed single-step degradation process. According to Liu *et al*. [19], the onset of decomposition temperature was characterized by the temperature at 5% weight loss ($T_{5\%}$) and summarized in Table 2. The decomposition of PA6/PP matrix started at 358°C, whereas the onset of decomposition for PA6/PP/PP-g-MA was observed at 391°C. This result indicates that the addition of PP-g-MA significantly improved the thermal stability of PA6/PP matrix. This could be attributed to the interaction (compatibility) between the maleic anhydride group of PP-g-MA and the amine terminal group of PA6 leading to the formation of a PP-g-PA6 copolymer, which could act as a compatibilizer [20]. Furthermore, the onset of decomposition for PA6/PP/MMT and PA6/PP/OMMT was observed at 362 and 371°C, respectively. This indicates that the incorporation of both MMT and OMMT improved the thermal stability of PA6/PP matrix at the beginning of degradation stage. The improvement in the initial degradation temperature could be associated with the clay as an inorganic material with high thermal stability and great barrier properties that can prevent the heat from transmitting quickly and can limit the continuous decomposition [21]. Furthermore, the initial decomposition temperature of PA6/PP/OMMT nanocomposite decreased, i.e. 355°C in the presence of PP-g-MA. The degradation of PP-g-MA is probably believed to be responsible for the observed trend. Furthermore, in the temperature range of 400–500°C, the PA6/PP/OMMT/PP-g-MA nanocomposite exhibited higher decomposition temperature than the PA6/PP blend and uncompatibilized PA6/PP/OMMT nanocomposites, indicating the enhancement of the thermal stability. The better dispersion and exfoliation of silicate layers in the polymer matrix for the PA6/PP/OMMT/PP-g-MA as confirmed by the XRD and TEM results earlier may be responsible for the improved thermal stability. The dispersed nanoscale silicate layers in the polymer matrix could be more effective in hindering diffusion of volatile decomposition products within the nanocomposite [22].

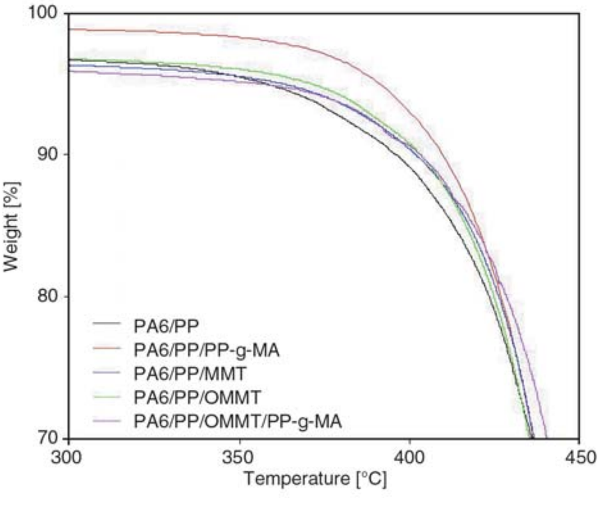

Figure 8. TGA curves of PA6/PP blends and its nanocomposites

Table 2. $T_{5\%}$ and HDT of PA6/PP blends and its nanocomposites

Sample designation	T5% [°C]	HDT [°C]
PA6/PP	358	90
PA6/PP/PP-g-MA	391	92
PA6/PP/MMT	362	98
PA6/PP/OMMT	371	109
PA6/PP/OMMT/PP-g-MA	355	113

3.5. HDT

Table 2 summarizes the HDT of PA6/PP blends and its nanocomposites. It can be seen that HDT of PA6/PP blend slightly increased in the presence of PP-g-MA. Furthermore, the addition of both MMT and OMMT increased the HDT of PA6/PP blend. This confirms the improved thermal stability of the PA6/PP blend with the presence of clay particles.

The presence of strong hydrogen bonds between the polymer matrix and clay surface is believed to be responsible for the increased HDT [23]. Compared with the PA6/PP/MMT composite, the PA6/PP/OMMT nanocomposite exhibited better improvement in HDT due to the better dispersion and exfoliation of clay layers in the polymer matrix. Similar observations were reported by Mohanty and Nayak [22] and Xie *et al.* [23] for PA6/montmorillonite nanocomposites. They found that the exfoliated PA6/OMMT nanocomposites showed larger improvement in HDT as compared to the intercalated PA6/MMT nanocomposites. Furthermore, the slight increase in the HDT of PA6/PP/OMMT nanocomposite in the presence of PP-g-MA could be attributed to the compatibilization effect of PP-g-MA.

3.6. Mechanical properties

Table 3 illustrates the tensile properties of the PA6/PP blends and its nanocomposites. It can be seen that the presence of PP-g-MA decreased the tensile modulus and strength of PA6/PP blend. The low modulus of PP-g-MA may be believed to be responsible for the observed trend. The addition of both MMT and OMMT significantly increased the tensile modulus of PA6/PP blend. This may be due to the reinforcement effect of the rigid inorganic clay and the constraining effect of silicate layers on molecular motion of polymer molecular chains [4, 6]. On other hand, the presence of both MMT and OMMT did not improve but decreased the tensile strength of PA6/PP blend. The poor dispersion of clay platelets as confirmed by the presence of a mixture of intercalated and exfoliated structures is believed to be responsible for the reduced tensile strength. It is interesting to note that the tensile modulus and strength of PA6/PP/OMMT significantly increased by the addition of PP-g-MA. By the addition of both OMMT and PP-g-MA, the tensile modulus and strength of PA6/PP matrix were increased by 27 and 30%, respectively. This remarkable improvement could be attributed to the compatibilizing effect of PP-g-MA. The presence of PP-g-MA improved the interfacial adhesion between PA6, PP, and OMMT resulting from the formation of PP-g-PA6 copolymer; besides promoting dispersion and exfoliation of OMMT in the PA6/PP matrix as confirmed by XRD and TEM results discussed earlier. It is accepted that the hydrogen bonding could form between the amide group of the PP-g-PA6 copolymer and amine group of organic modifier in the OMMT. This amide-amine reaction could happen when the OMMT was exfoliated in the PA6/PP matrix; subsequently the amine group of organic modifier is capable of forming a chemical linkage with PP-g-PA6 copolymer. The formation of PP-g-PA6 and the chemical linkage of PP-g-PA6 copolymer with organic modifier of OMMT have been reported in our previous study [24] for PP-g-MA compatibilized PA6/PP nanocomposites using commercial organoclay with the organic modifier of octadecylamine (Nanomer I30TC, USA). The tensile strength of PP-g-MA compatibilized PA6/PP nanocomposites containing OMMT with the organic modifier of dodecylamine (51.81 MPa) is higher than the commercial organoclay (49.6 MPa). This could be attributed to the OMMT containing dodecylamine is more effective for the formation of the exfoliated structure. Reichert *et al.* [8] have reported a similar observation where the presence of PP-g-MA enhanced the tensile modulus and strength of PP/organoclay nanocomposites due to the improved interfacial adhesion between PP and organoclay.

From Table 3, it is evident that the elongation at break of PA6/PP blend drastically increased with the presence of PP-g-MA. This could be attributed to the formation of PP-g-PA6 copolymer which improved interfacial adhesion between PA6 and PP phases. Furthermore, the addition of both MMT

Table 3. Mechanical properties of PA6/PP/OMMT nanocomposites

Sample designation	Tensile modulus [GPa]	Tensile strength [MPa]	Elongation at break [%]	Flexural modulus [GPa]	Flexural strength [MPa]	Impact strength [kJ/m²]
PA6/PP	1.76 ± 0.02	39.96 ± 0.43	12.21 ± 0.75	1.91 ± 0.05	62.50 ± 1.25	5.47 ± 0.45
PA6/PP/PP-g-MA	1.60 ± 0.00	30.70 ± 1.80	55.70 ± 6.30	1.70 ± 0.00	59.20 ± 0.40	6.10 ± 0.40
PA6/PP/MMT	1.95 ± 0.02	38.65 ± 0.82	8.15 ± 0.91	2.32 ± 0.05	62.51 ± 0.03	3.58 ± 0.18
PA6/PP/OMMT	2.01 ± 0.03	38.67 ± 0.46	2.72 ± 0.14	2.56 ± 0.04	62.22 ± 0.42	1.55 ± 0.05
PA6/PP/OMMT/PP-g-MA	2.23 ± 0.03	51.81 ± 0.88	3.46 ± 0.13	2.56 ± 0.03	78.47 ± 1.89	1.88 ± 0.11

and OMMT drastically decreased the elongation at break of PA6/PP matrix. This suggests that the PA6/PP matrix became brittle in the presence of clay particles. The reduction in ductility was attributed to the constrained mobility of polymer chains in the presence of clay particles [25]. The higher ductility observed for the PA6/PP/MMT compared to PA6/PP/OMMT nanocomposite may be attributed to the intercalated structure in the PA6/PP/MMT composite and a mixture of intercalated and exfoliated structure in the PA6/PP/OMMT nanocomposite. Masenelli-Varlot *et al.* [26] reported that the intercalated PA6/clay nanocomposites had a higher elongation at break than exfoliated nanocomposites. The slight increase in elongation at break was obtained for the PP-g-MA compatibilized PA6/PP/OMMT nanocomposite albeit it was still lower than the PA6/PP blend. The improved interfacial adhesion between PA6, PP, and OMMT resulting from the formation of PP-g-PA6 a copolymer is believed to be responsible for the observed trend.

Table 3 also highlights the flexural properties of the PA6/PP blends and its nanocomposites. The addition of PP-g-MA reduced the flexural modulus and strength of PA6/PP blend. This trend resembles that of the tensile properties. The reduction in flexural properties could be attributed to the low molecular weight and low modulus of PP-g-MA. The incorporation of both MMT and OMMT significantly increased the flexural modulus of PA6/PP blend. This could be attributed to high stiffness and aspect ratio of silicate layers [27]. Compared with the PA6/PP/MMT composite, the flexural modulus of PA6/PP/OMMT nanocomposite was higher because of the nanoscale structure, the large aspect ratio, the large surface area of the layered silicates, and the corresponding strong interaction between polymer molecules chains and silicate surface [28]. On other hand, the flexural strength of PA6/PP matrix remained unchanged by the addition of both MMT and OMMT. However, the flexural properties of PA6/PP/OMMT nanocomposite significantly increased by the addition of PP-g-MA as in case of tensile properties discussed earlier. This may be again attributed to the compatibilizing effect of PP-g-MA in which improved the interfacial adhesion and promoted the degree of exfoliation of OMMT in the PA6/PP matrix.

From Table 3, it can also be noted that the incorporation of PP-g-MA led to an increase in impact strength of the PA6/PP blend. A similar trend to that of the elongation at break was observed. The enhanced impact strength may be attributed to the improved interfacial adhesion between PA6 and PP resulting from the formation of PP-g-PA6 copolymer [3]. The incorporation of both MMT and OMMT drastically decreased the impact strength of PA6/PP blend. The reduction in toughness may be attributed to the lack of the crack front deflection and cavitation mechanisms in the clay-polymer nanocomposites reinforced with silicate nano-layers of high stiffness [29]. According to Nair *et al.* [30], the reduction in toughness of polyamide 6,6/clay nanocomposites may be caused by the formation of micro voids or micro cracks in the crack-tip region and tend to reduce toughness. The lower impact strength observed for the PA6/PP/OMMT compared to the PA6/PP/MMT could be attributed to a mixture of intercalated and exfoliated structures in the nanocomposite. According to Miyagawa *et al.* [31], the individual exfoliated clay platelets (~1 nm in thickness) are not effective to prevent the crack from propagating. It is easy to break the exfoliated clay platelets due to their high stiffness. Consequently, the PA6/PP/OMMT nanocomposite has low impact strength. Cavitation may occur in the vicinity of intercalated clay platelets in the PA6/PP/MMT composite. Cavitation mechanism may be believed to be responsible for higher impact strength in the PA6/PP/MMT [32]. Furthermore, the slight increase in impact strength could be observed for the PA6/PP/OMMT in the presence of PP-g-MA. The improved interfacial adhesion resulting from the formation of a PP-g-PA6 copolymer is believed to be responsible for the slight increase in toughness. The improvement in impact strength by the addition of PP-g-MA was also reported by Liu *et al.* [33] for PA6/clay nanocomposites.

4. Conclusions

The organic modification of MMT with dodecylamine was successfully performed as confirmed by the FTIR (the presence of organic groups such as –NH and –CH) and XRD results (the expanded basal spacing). XRD and TEM results revealed that the intercalated structure was formed for PA6/PP/

MMT composite, a mixture of intercalated and exfoliated structures for PA6/PP/OMMT nanocomposite, and exfoliated structure for PP-g-MA compatibilized PA6/PP/OMMT nanocomposite. The addition of both MMT and OMMT improved stiffness, thermal stability, and HDT but reduced toughness of PA6/PP matrix. The presence of PP-g-MA in the PA6/PP/OMMT nanocomposite enhanced properties such as stiffness, strength, ductility, impact strength, and HDT.

Acknowledgements

The authors would like to AUN/SEED-Net JICA, Japan for financial support (project grant no: 6050071) and short-term study program for one of us (Mr. Kusmono) at Toyohashi University of Technology, Japan.

References

[1] Marco C., Ellis G., Gómez M. A., Fatou J. G., Arribas J. M., Campoy I., Fontecha A.: Rheological properties, crystallization, and morphology of compatibilized blends of isotactic polypropylene and polyamide. Journal of Applied Polymer Science, **65**, 2665–2677 (1997).

[2] Ide F., Hasegawa A.: Studies on polymer blend of nylon and polypropylene or nylon 6 and polystyrene using the reaction of polymer. Journal of Applied Polymer Science, **18**, 963–974 (1974).

[3] Sathe S. N., Devi S., Rao G. S. S., Rao K. V.: Relationship between morphology and mechanical properties of binary and compatibilized ternary blends of polypropylene and nylon 6. Journal of Applied Polymer Science, **61**, 97–107 (1996).

[4] Liu T., Tjiu W. C., He C., Na S. S., Chung T. S.: A processing-induced clay dispersion and its effect on the structure and properties of polyamide 6. Polymer International, **53**, 392–399 (2004).

[5] Cho J. W., Paul D. R.: Nylon 6 nanocomposites by melt compounding. Polymer, **42**, 1083–1094 (2001).

[6] Yu Z. Z., Yan C., Yang M., Mai Y. W.: Mechanical and dynamic mechanical properties of nylon 66/montmorillonite nanocomposites fabricated by melt compounding. Polymer International, **53**, 1093–1098 (2004).

[7] Ma C. C. M., Kuo C. T., Kuan H. C., Chiang C. L.: Effects of swelling agents on the crystallization behavior and mechanical properties of polyamide 6/clay nanocomposites. Journal of Applied Polymer Science, **88**, 1686–1693 (2003).

[8] Reichert P., Nitz H., Klinke S., Brandsch R., Thomann R., Mülhaupt R.: Poly(propylene)/organoclay nanocomposite formation: Influence of compatibilizer functionality and organoclay modification. Macromolecular Materials and Engineering, **275**, 8–17 (2000).

[9] Chow W. S., Mohd Ishak Z. A., Ishiaku U. S., Karger-Kocsis J., Apostolov A. A.: The Effect of organoclay on the mechanical properties and morphology of injection-molded polyamide 6/polypropylene nanocomposites. Journal of Applied Polymer Science, **91**, 175–189 (2004).

[10] Tang Y., Hu Y., Zhang R., Gui Z., Wang Z., Chen Z., Fan W.: Investigation on polypropylene and polyamid-6 alloys/montmorillonite nanocomposites. Polymer, **45**, 5317–5326 (2004).

[11] Agag T., Takeichi T.: Polybenzoxazine-montmorillonite hybrid nanocomposites: synthesis and characterization. Polymer, **41**, 7083–7090 (2000).

[12] Zheng H., Zhang Y., Peng Z., Zhang Y.: Influence of the clay modification and compatibilizer on the structure and mechanical properties of ethylene-propylene-diene rubber/montmorillonite composites. Journal of Applied Polymer Science, **92**, 638–646 (2004).

[13] Pegoretti A., Dorigato A., Penati A.: Tensile mechanical response of polyethylene-clay nanocomposites. Express Polymer Letters, **1**, 123–131 (2007).

[14] Chow W. S., Mohd Ishak Z. A.: Mechanical, morphological and rheological properties of polyamide 6/organo-montmorillonite nanocomposites. Express Polymer Letters, **1**, 77–83 (2007).

[15] Chow W. S., Mohd Ishak Z. A., Karger-Kocsis J.: Atomic force microscopy study on blend morphology and clay dispersion in polyamide-6/polypropylene/organoclay systems. Journal of Polymer Science Part B: Polymer Physics, **43**, 1198–1204 (2005).

[16] Bray H. J., Redfern S. A. T., Clark S. M.: The kinetics of dehydration in Ca-montmorillonite; an in situ X-ray diffraction study. Mineralogical Magazine, **62**, 647–656 (1998).

[17] Bala P., Samantaraya B. K., Srivastava S. K.: Synthesis and characterization of Na-montmorillonite-alkylammonium intercalation compounds. Materials Research Bulletin, **35**, 1717–1724 (2000).

[18] Olphen H. V., Fripiat J. J.: Data handbook for clay materials and other non-metallic minerals. Pergamon Press, Oxford (1979).

[19] Liu T., Lim K. P., Tjiu W. C., Pramoda K. P., Chen Z. K.: Preparation and characterization of nylon 11/organoclay nanocomposites. Polymer, **44**, 3529–3535 (2003).

[20] Jose S., Thomas P. S., Thomas S., Karger-Kocsis J.: Thermal and crystallisation behaviours of blends of polyamide 12 with styrene-ethylene/butylene-styrene rubbers. Polymer, **47**, 6328–6336 (2006).

[21] Zhang W., Liang Y., Luo W., Fang Y.: Effects of clay-modifying agents on the morphology and properties of poly (methyl methacrylate)/clay nanocomposites synthesized via γ-ray irradiation polymerization. Journal of Polymer Science Part A: Polymer Chemistry, **41**, 3218–3226 (2003).

[22] Mohanty S., Nayak S. K.: Effect of clay exfoliation and organic modification on morphological, dynamic mechanical, and thermal behavior of melt-compounded polyamide-6 nanocomposites. Polymer Composites, **28**, 153–162 (2007).

[23] Xie S., Zhang S., Wang F., Liu H., Yang M.: Influence of annealing treatment on the heat distortion temperature of nylon-6/montmorillonite nanocomposites. Polymer Engineering and Science, **45**, 1247–1253 (2005).

[24] Chow W. S., Mohd Ishak Z. A., Karger-Kocsis J., Apostolov A. A., Ishiaku U. S.: Compatibilizing effect of maleated polypropylene on the mechanical properties and morphology of injection molded polyamide 6/polypropylene/organoclay nanocomposites. Polymer, **44**, 7427–7440 (2003).

[25] Chen L., Wong S. C., Pisharath S.: Fracture properties of nanoclay-filled polypropylene. Journal of Applied Polymer Science, **88**, 3298–3305 (2003).

[26] Masenelli-Varlot K., Reynaud E., Vigier G., Varlet J.: Mechanical properties of clay reinforced polyamide. Journal of Polymer Science Part B: Polymer Physics, **40**, 272–283 (2002).

[27] Parija S., Nayak S. K., Verma S. K., Tripathy S. S.: Studies on physico-mechanical properties and thermal characteristics of polypropylene/layered silicate nanocomposites. Polymer Composites, **25**, 646–652 (2004).

[28] Shishan W., Dingjun J., Xiaodong O., Fen W., Jian S.: The structure and properties of PA6/MMT nanocomposites prepared by melt compounding. Polymer Engineering and Science, **44**, 2070–2074 (2004).

[29] Bao S. P., Tjong S. C.: Impact essential work of fracture of polypropylene/montmorillonite nanocomposites toughened with SEBS-*g*-MA elastomer. Composites Part A: Applied Science and Manufacturing, **38**, 378–387 (2007).

[30] Nair S. V., Goettler L. A., Lysek B. A.: Toughness of nanoscale and multiscale polyamide-6,6 composites. Polymer Engineering and Science, **42**, 1872–1882 (2002).

[31] Miyagawa H., Jurek R. J., Mohanty A. K., Misra M., Drzal L. T.: Biobased epoxy/clay nanocomposites as a new matrix for CRFP. Composites Part A: Applied Science and Manufacturing, **37**, 54–62 (2006).

[32] Zhang H., Zhang Z., Yang J. L., Friedrich K.: Temperature dependence of crack initiation fracture toughness of various nanoparticles filled polyamide 66. Polymer, **47**, 679–689 (2006).

[33] Liu X., Wu Q., Berglund L. A., Fan J., Qi Z.: Polyamide 6-clay nanocomposites/polypropylene-grafted-maleic anhydride alloys. Polymer, **42**, 8235–8239 (2001).

eXPRESS Polymer Letters Vol.2, No.9 (2008) 665–676
Available online at www.expresspolymlett.com
DOI: 10.3144/expresspolymlett.2008.79

Finite element investigations on the microstructure of fibre-reinforced composites

A. R. Maligno[*], *N. A. Warrior, A. C. Long*

School of Mechanical, Materials and Manufacturing Engineering, The University of Nottingham, University Park;
Nottingham, NG7 2RD, UK

Received 21 June 2008; accepted in revised form 8 August 2008

Abstract. The effect of residual stress due to the curing process on damage evolution in unidirectional (UD) fibre-reinforced polymer-matrix composites under longitudinal and transverse loading has been investigated using a three-dimensional micromechanical representative volume element (RVE) model with a hexagonal packing geometry and the finite element method. Residual stress has been determined by considering two contributions: volume shrinkage of matrix resin from the crosslink polymerization during isothermal curing and thermal contraction of both resin and fibre as a result of cooling from the curing temperature to room temperature. To examine the effect of residual stress on failure, a study based on different failure criteria and a stiffness degradation technique has been used for damage analysis of the RVE subjected to mechanical loading after curing for a range of fibre volume fractions. Predicted damage initiation and evolution are clearly influenced by the presence of residual stress.

Keywords: *damage mechanism, residual stress, failure criteria*

1. Introduction

The fabrication process of fibre-reinforced polymer matrix composite materials requires a high temperature curing procedure. Stresses are generated during cool-down, mainly due to the mismatch between the coefficients of thermal expansion (CTE) of the fibre and matrix. Residual stresses have important effects on the thermo-mechanical behaviour of composite materials and, moreover, the resulting stresses are sufficient to initiate fracture within the matrix immediately around the fibre [1, 2]. Therefore, it is important to determine the current state of the residual stresses and their effects on the behaviour of the composite when subsequently subjected to multi-axial mechanical loading. After curing and cooling of the composite, the matrix is subject to a tri-axial residual stress state [3]. The resulting thermal residual stresses are of compressive nature in the fibre and tensile nature in the matrix [4]. For glass fibre epoxy resin composites, Fiedler *et al.* [4] showed that the thermal residual stresses can be calculated by finite element analysis (FEA) using the actual temperature dependent stiffness of the resin [4]. Asp *et al.* [5] showed by a FEA study that the thermal residual stress strongly reduces the ultimate strength of transversely loaded unidirectional (UD) composites. When load is applied to the fibre-reinforced composite the tri-axial stresses in the matrix increase. Both the polymer matrix and the fibres cannot behave as they would individually as bulk materials, and the difference in the Poisson's ratios causes a tri-axial stress state reducing the maximum bearable load. In recent studies [5–7], it was shown that yield criteria are applicable to glassy polymers under uniaxial, biaxial and triaxial load-

---

[*]Corresponding author, e-mail: angelo.maligno@nottingham.ac.uk

ing if the hydrostatic stress effect is accounted for. Also it was found that for UD composites, yielding is suppressed while a brittle failure due to crack growth occurs. Fiedler *et al.* [4] also demonstrated that the parabolic Mohr failure criterion is suitable to describe the experimentally observed macroscopic yield and fracture behaviour of epoxy resin [8, 9]. The micro-residual stresses depending on the local fibre distribution can improve or reduce the local ultimate transverse strength of the composite [10]. In order to clarify the role of thermal residual stresses in composites a number of analytical models have been proposed. Analytical approaches include methods based on the Self-Consistent Model (SCM) of Hill [11], extension of the Eshelby's equivalent inclusion technique [12], Vanishing Fibre Diameter (VFD) model of Dvorak [13], Concentric Cylinder Models [14, 15] and Aboudi's Method of Cells [16]. The effects of thermal residual stresses on mechanical behaviour of the composite materials have also been extensively studied by Nimmer [17] and Wisnom [18]. They examined the transverse behaviour of high temperature composites in the presence of thermally induced residual stress fields and found that the presence of residual stresses is beneficial for the transverse behaviour of composites with low interfacial strength due to the generation of compressive residual stresses at the interface of the fibre and matrix. Three dimensional finite element models have been employed to study the influence of residual stresses on shear response of the composites [19, 20]. More recently, a finite element micromechanical based model has been developed to investigate the off-axis behaviour of unidirectional composites [21]. This model is general and can be used for any combination of normal and shear loading with residual stresses. Use of FEA with periodic representative volume elements (RVE) is well established [5, 6, 22, 23]. In most cases, the analysis is based on a uniform, square or hexagonal fibre array. In this work, a 3D finite element analysis was used to study the residual stress distribution and its effect on transverse and longitudinal failure and damage evolution of fibre-reinforced polymer matrix composites using a micromechanical RVE model. Moreover, four different fibre volume fraction (V_f) RVEs were investigated in order to evaluate their response to uniaxial loading with and without residual stress. The residual stress introduced during curing was determined by considering the contributions from both the chemical shrinkage of resin and the thermal cooling contraction of fibre and resin. Effects of residual stress on damage evolution and failure in RVEs subjected to mechanical loading were predicted using two different failure criteria and a post-failure stiffness reduction technique.

2. Finite element modelling

2.1. Micromechanical model

Composite materials properties, e.g. strength and stiffness, are dependent upon the fibre volume fraction and individual properties of the constituent fibre and matrix materials and the estimation of damage and failure progression is more complex than in conventional metallic materials. In the micromechanical approach, the constituent fibre and matrix materials and their interaction are distinctively considered to predict the overall behaviour of the composite material structure. The advantage of the micromechanical model is that the stresses can be associated and related to each constituent (fibre and matrix). Therefore, failure can be identified in each of these constituents and the appropriate property degradation can be modelled. Also, different fibre volume fractions can be taken into account by varying the geometry of the RVE. Here, the micromechanical model considers a RVE in which fibre and matrix are assumed to be perfectly bonded to the fibres throughout the analysis, with fibres arranged in a hexagonal cross section array by assuming the repetitive or periodic nature of the fibre and matrix materials. The RVE is a three-dimensional solid and the geometry of each

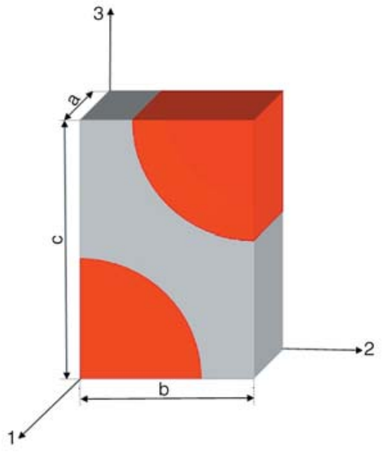

Figure 1. Ideal RVE for the hexagonal array packing

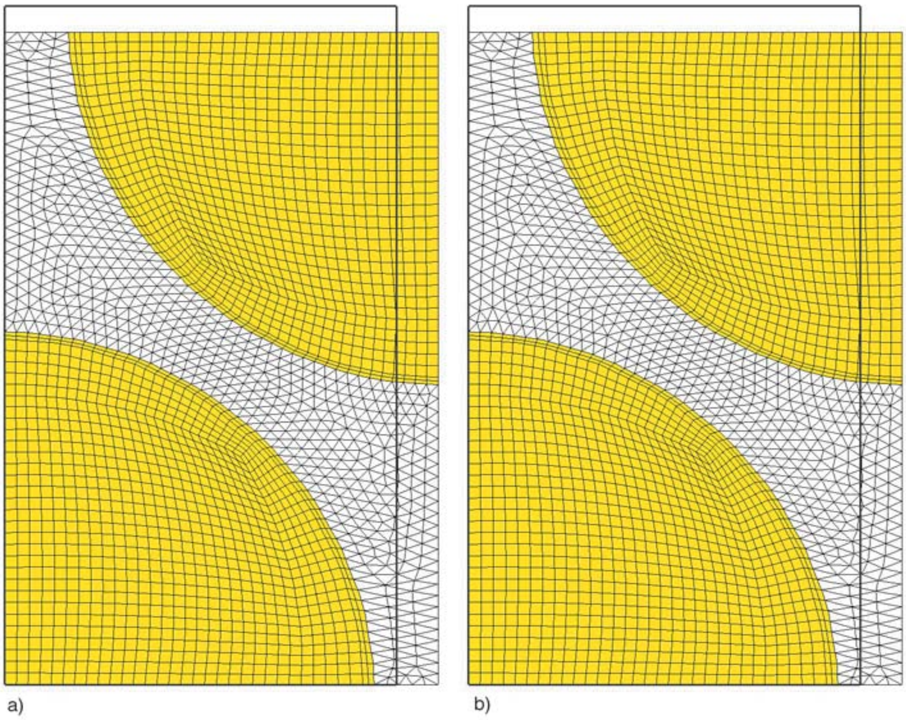

Figure 2. Un-deformed meshed (a) and its deformed shape (b) on transverse loading (2-direction) for an RVE with $V_f = 70\%$

RVE depends on the fibre volume fraction [22]. The RVE used in these investigations is displayed in Figure 1. The displacement constraints applied to the finite element model displayed in Figure 1 are [22]: $\mathbf{u_1}$ (0,2,3) = 0; $\mathbf{u_1}$ (a,2,3) = constant = δ_1; $\mathbf{u_2}$ (1,0,3) = 0; $\mathbf{u_2}$ (1,b,3) = constant = δ_2; $\mathbf{u_3}$ (1,2,0) = 0; $\mathbf{u_3}$ (1,2,c) = constant = δ_3; where $\mathbf{u_1}$, $\mathbf{u_2}$, $\mathbf{u_3}$ denote displacements in the 1-, 2- and 3-direction, respectively. The meshes generated for the micromodels investigated are 20-noded hexahedral elements. The number of elements varies approximately from 6000 to 9000 depending on the V_f. Mesh sensitivity analysis suggests that the meshes are fine enough to produce accurate results compared to a mesh with twice as many elements, with a difference within 0.2% in terms of residual stress and failure strain level. In Figure 2 is depicted an example of the mesh for an RVE with a $V_f = 70\%$ loaded in the transverse direction (2-direction).

2.2. Residual stress analysis

The total induced strain of the resin due to chemical shrinkage and thermal cooling can be expressed by Equation (1):

$$\mathrm{d}\varepsilon_{ij} = \mathrm{d}e_{ij} + \delta_{ij}\mathrm{d}s + \delta_{ij}\alpha(T)\mathrm{d}T \tag{1}$$

where $\mathrm{d}\varepsilon_{ij}$ is the total strain increment, $\mathrm{d}e_{ij}$ the elastic strain increment, ds the free shrinkage strain increment due to the chemical reaction (cross-linking) in the absence of constraint, $\alpha(T)$ the thermal expansion coefficient which is dependent on the temperature, dT the temperature change and δ_{ij} is the Kronecker delta. From Equation (1), the stress-strain relationship can be derived as shown in Equation (2):

$$\mathrm{d}\sigma_{ij} = C_{ijkl}\mathrm{d}e_{kl} = C_{ijkl}\{\mathrm{d}\varepsilon_{kl} - \delta_{ij}\mathrm{d}s - \delta_{ij}\alpha(T)\mathrm{d}T\} \tag{2}$$

where $\mathrm{d}\sigma_{ij}$ are the stress increments and C_{ijkl} the stiffness components. The above stress analysis is based on linear elasticity and the stiffness components C_{ijkl} are related to the Young's modulus E and the Poisson's ratio ν of the material. Equation (2) was derived for the residual stress analysis in the resin.

2.3. Material

Several authors such as Zhao *et al*. [23] have employed in their studies more realistic constitutive theories for the epoxy matrix (e.g. non linear viscoelasticity). However, numerical results have shown that damage onset and evolution are not influenced by the stress-relaxation, induced by the viscoelastic behaviour and, the final amount of residual stress (after cooling) is not in general significantly affected by the viscoelastic property of the resin. Hence, residual stress and its effect on transverse and longitudinal failure of UD composites have been investigated considering the linear-elastic behaviour of the constituents. In particular, the materials used in this investigation are glass fibre and epoxy resin, whose properties are given in [24]. The properties of glass fibre are assumed to remain constant and independent of the temperature change with Young's modulus $E = 80$ GPa and Poisson's ratio $\nu = 0.22$, the coefficient of thermal expansion $\alpha = 4.9\cdot10^{-6}$/°C and the longitudinal tensile (σ_T) and compressive (σ_C) strength are 2150 and 1450 MPa, respectively. However, for the epoxy resin, thermal transition temperatures such as the glass transition temperature T_g strongly affect mechanical properties [24]. In order to represent this behaviour accurately the material properties of the resin are defined as a function of temperature. The following relations are used:

(a) Poisson's ratio is assumed to be temperature independent ($\nu = 0.35$).

(b) To evaluate the variation of Young's modulus E over the temperature range from curing to room temperature, the total temperature range can be divided into three regions:

- $T_g - \Delta T \le T \le T_g + \Delta T$, in which E varies greatly.
- $T > T_g + \Delta T$, the matrix is in liquid or rubbery state and E has a very small value.
- $T < T_g - \Delta T$, the matrix is in solid state and E changes only slightly.

For each region, the modulus is obtained using the following functions given by Equations (3)–(5) [25]:

$$E(T) = E(T_r)\exp\left(-k_1\frac{T-T_r}{T_g-\Delta T-T_r}\right),\quad T < T_g - \Delta T, \tag{3}$$

$$E(T) = E(T_g-\Delta T)\exp\left(-k_2\frac{T-T_g+\Delta T}{\Delta T+\Delta T}\right),\quad T_g - \Delta T \le T \le T_g + \Delta T, \tag{4}$$

$$E(T) = 0.01E(T_r),\ T > T_g + \Delta T, \tag{5}$$

with: $T_g = 110$°C; $T_r = 23$°C; $\Delta T = 35$°C; $E(T_r) = 3.35$ GPa; $E(T_g - \Delta T) = 0.7E(T_r)$; $E(T_g + \Delta T) = 0.01E(T_r)$; $k_1 = 0.357$; $k_2 = 4.249$.

(c) The thermal expansion coefficient α is assumed to change linearly with the temperature: $\alpha(T) = K(T - T_{ref}) + \alpha(T_r)$, with a slope given by Equation (6):

$$K = \frac{\alpha_l - \alpha(T_r)}{T_g - T_r} \tag{6}$$

where $\alpha(T_r) = 58\cdot10^{-6}$/°C and $\alpha_l = 139\cdot10^{-6}$/°C.
The longitudinal tensile (σ_T) and compressive (σ_C) strength of the resin are taken to be 80 and 120M Pa, respectively.

3. Failure criteria and damage evolution model

The selection of a proper failure criterion, both for matrix and fibre, represents a very important task of the modelling formulation. In particular in polymers the yield behaviour is sensitive to hydrostatic stress and as a consequence, the yield stress in tension is different from that in compression [7, 26, and 27]. Both fibre and resin are isotropic materials and the Maximum Principal Stress theory is applicable to simulate damage onset and evolution within the RVE (e.g. fibre/matrix debonding, matrix crack). If the stress level satisfies the failure criterion, the fibre or matrix would crack. Final failure corresponds to the rupture of the composite, which is unable to carry further load. The Maximum Principal Stress failure criterion is summarized as shown in Equations (7) and (8):

$$\sigma_{\max} < \sigma_u^t \tag{7}$$

$$|\sigma_{\min}| < \sigma_u^c \tag{8}$$

where σ_{max} and $\sigma_{\min}$ are the Maximum and Minimum Principal Stresses, σ_u^t is the tensile strength and σ_u^c is the compressive strength of the material.

A modification of the von Mises criterion has also been also considered to evaluate failure in the matrix. As the von Mises criterion does not predict differences in yield stress between tension and compression, modifications of this criterion have incorporated the effects of hydrostatic pressure. A general form for the modified von Mises criterion can be written as shown in Equation (9) [7]:

$$A(\sigma_1+\sigma_2+\sigma_3)+ \\ B[(\sigma_1-\sigma_2)^2+(\sigma_2-\sigma_3)^2+(\sigma_3-\sigma_1)^2]=1 \tag{9}$$

It is possible to determine the constants A and B in term of the simple uniaxial tensile ($\sigma_{y,T}$) and compressive ($\sigma_{y,C}$) yield stresses. The modified von Mises stress criterion was suggested by Raghava and has been shown to agree very well with experimental data for epoxy resin – see Equation (10) [7]:

$$2(\sigma_{y,C}-\sigma_{y,T})(\sigma_1+\sigma_2+\sigma_3)+ \\ [(\sigma_1-\sigma_2)^2+(\sigma_2-\sigma_3)^2+(\sigma_3-\sigma_1)^2]=2\sigma_{y,C}\sigma_{y,T} \tag{10}$$

If $\sigma_{y,C} = \sigma_{y,T}$ this criterion reduces to the von Mises criterion. To simulate damage, it is necessary to evaluate the current stress state at each integration point. Then by comparing the current stress state with a specific failure criterion, the material properties are reduced at each 'failed' integration point to values representing the particular type of damage that has occurred [28–30]. The degradation scheme, together with the residual stress analysis was programmed into a user-defined material subroutine (UMAT) interfaced with the commercial finite element code ABAQUS Standard [31]. When failure is detected the degradation is applied only on the elastic moduli by multiplying them with a discount factor $d_i \in (0, 1]$ (i designates the elastic modulus to which the factor is applied). Both resin and fibre were modelled as isotropic with they the stiffness matrix shown in Equation (11):

$$[C]=[S]^{-1}= \begin{bmatrix} \frac{1}{d_E E} & -\frac{\nu}{d_E E} & -\frac{\nu}{d_E E} & 0 & 0 & 0 \\ -\frac{\nu}{d_E E} & \frac{1}{d_E E} & -\frac{\nu}{d_E E} & 0 & 0 & 0 \\ -\frac{\nu}{d_E E} & -\frac{\nu}{d_E E} & \frac{1}{d_E E} & 0 & 0 & 0 \\ 0 & 0 & 0 & \frac{1}{d_G D} & 0 & 0 \\ 0 & 0 & 0 & 0 & \frac{1}{d_G D} & 0 \\ 0 & 0 & 0 & 0 & 0 & \frac{1}{d_G D} \end{bmatrix}^{-1} \tag{11}$$

The Young's modulus E and the shear modulus G are degraded independently by discount factor d_E and d_G both initially set equal to the unity. If during the analysis the stress level exceed the maximum strength allowed for matrix and/or fibre according to the failure criterion, the modulus E is degraded to 1% of its initial value ($d_E = 0.01$) at the particular integration point. The shear modulus G is reduced to 20% of the initial value ($d_G = 0.2$) under the assumption that some shear stiffness remains due to the friction still present on the failure plane [30]. The behaviour of the matrix and the fibre was assumed to be linear elastic until damage was predicted. The response after damage occurred was also linear elastic but with degraded moduli.

4. Results and discussion

4.1. Residual stress

Residual stress has two parts: the chemical shrinkage residual stress and the thermal cooling residual stress. The analysis was performed by two discrete steps, where step *one* is the shrinkage stress analysis and step *two* is the thermal cooling stress analysis. The shrinkage residual stress was calculated by applying a given amount of resin shrinkage. For the epoxy resin considered here, the linear shrinkage strain was chosen to be 1%, which corresponds to a volumetric change of less than 3% [32] depending on the fibre volume fraction and the effect of the fibres on longitudinal shrinkage during curing. The thermal residual stress is due to the cooling of the system from the curing temperature, 149°C, to room temperature, 23°C. The distribution of the resin's maximum principal residual stress in the matrix, after curing and cooling is presented in Figure 3. The mechanical properties of the resin, in terms of shear modulus (and Young's modulus

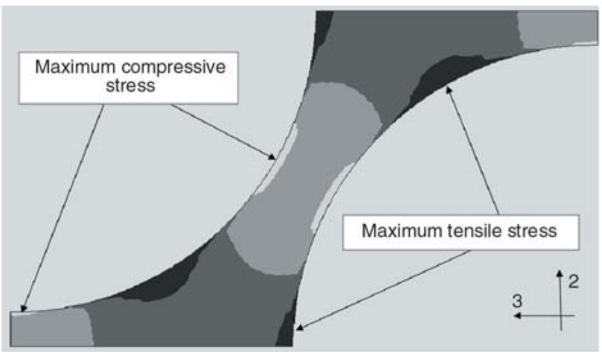

Figure 3. Distribution of residual stress in the matrix after curing and cooling-down

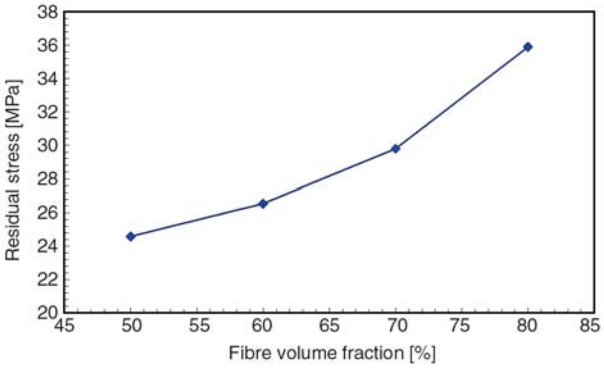

Figure 4. Trend of maximum principal residual stress [MPa] after curing and cooling-down evaluated in the area of max tensile stress at different V_f

when the resin becomes solid), increase drastically as the material evolves from a liquid state to a solid state. So in the resin, geometrically constrained within the interstices present between fibres, tensile stresses develop more easily. The largest values reached after chemical shrinkage and cooling are depicted in Figure 4. Results from the analysis attribute the primary contribution to residual stress mainly to thermal cooling. In Figure 5 the small contribution from the chemical shrinkage for four different fibre volume fractions is shown. Moreover, as afore mentioned, the small calculated internal stress level, due to the curing process, is likely to be overestimated since the viscoelastic properties of the resin are not taken into account (i.e. these stresses are likely to relax further with time) [23]. These curing stresses are small as a result of the mechanical properties of the resin during the curing process. In fact, its state is rubbery and almost liquid so the capability to interact with the fibres by transferring stresses is negligible. These results agree with most of the published work on residual stresses in which thermal cooling was evaluated as the main source of residual stress in polymer composites [33, 34].

4.2. Effect of residual stress on transverse and longitudinal failure

To study the influence of residual stress/strain on the overall response of the composites at their microscale, the damage evolution in the matrix was examined under transverse loading. After curing and thermal cooling analyses, a global strain was applied to the micro-models which were achieved by specifying a uniform displacement on the RVEs faces. At each time increment of the analysis, the damaged area in the matrix was determined using both the Maximum Principal Stress failure criterion and the von Mises criterion modified by Raghava. Throughout the following analyses, the fibre showed no sign of damage due to its high strength, therefore, damage and failure refer to the matrix only.

4.2.1. Uniaxial tensile loading along 1-direction

In UD composites the effect of the fibre is dominant, therefore during curing, in which resin is in a rubbery state, realistically, no deformation is established along the 1-direction. The strains, developed during the manufacturing process, are parallel to the fibres orientation as the resin evolves from a liquid/rubbery state into a solid state. In addition, as the fibres are dominant, the strength of the micromodels is improved if fibre volume fraction is increased. A comparison between two different combinations of failure criteria was investigated:

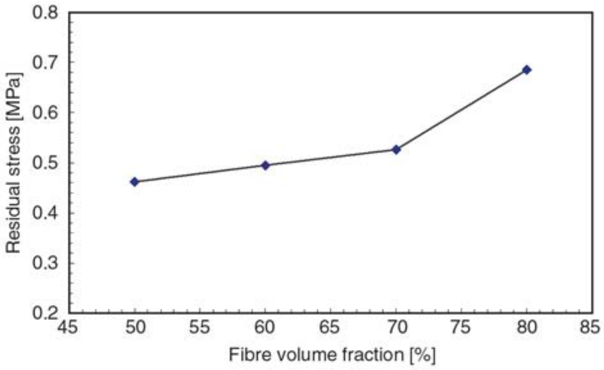

Figure 5. Trend of maximum principal residual stress [MPa] after curing evaluated in the area of max tensile stress at different V_f

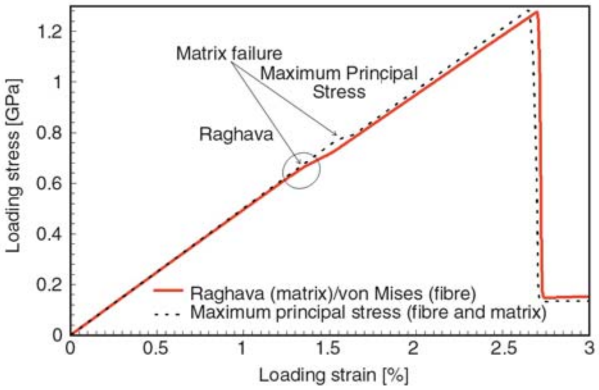

Figure 6. Global stress-strain curve in 1-direction for uniaxial tensile loading for $V_f = 60\%$ (Residual stress analysis)

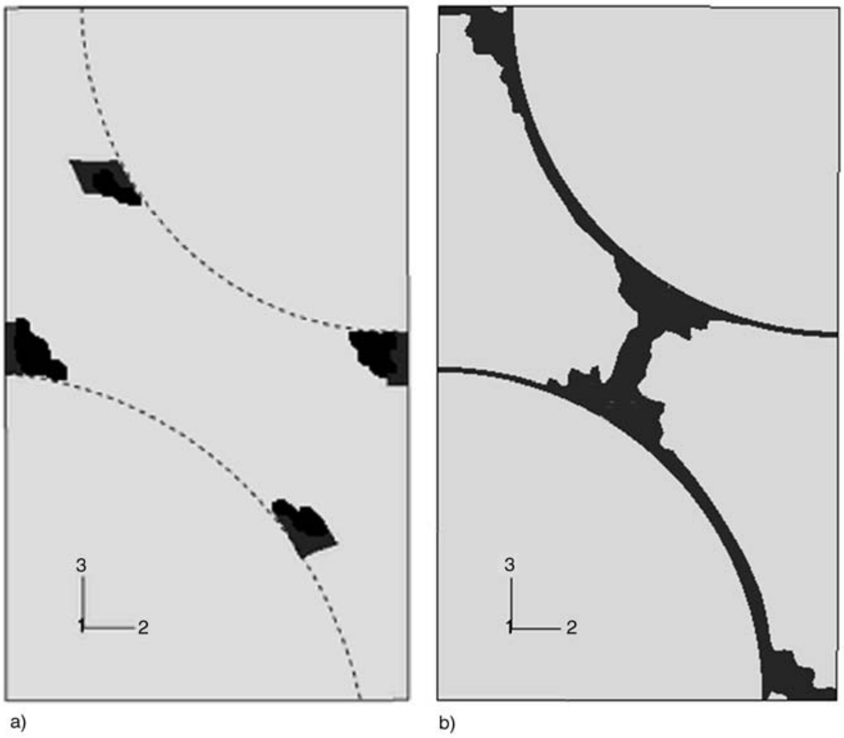

Figure 7. Comparison on damage onset prediction ($V_f = 60\%$) in presence of residual stress. Maximum Principal Stress (a), Raghava failure criterion (b).

1 – Raghava (matrix)/von Mises (fibre).
2 – Maximum Principal Stress (matrix)/Maximum Principal Stress (fibre).

Both combinations show similar results in terms of ultimate strength for the fibre with residual stress (Figure 6) but, the Raghava criterion predicts matrix failure at a lower loading strain. In addition, the two combinations of failure criteria show a difference in the prediction of damage onset in the matrix. In fact, while for the Maximum Principal Stress the initiation of the damage is concentrated in four regions at the fibre/matrix interface (Figure 7a), the Raghava failure criterion predicts a drastic fibre/matrix debonding and also damage within the resin at the interstices between fibres, as shown in (Figure 7b). Comparison between stress/strain curves with and without residual stress (Figure 8) shows that a premature matrix failure occurs if residual stresses are applied. In fact, it is evident from Figure 8 that, although the presence of thermal residual stresses does not modify the ultimate strength of fibres along the 1-direction of loading, it leads to a greatly detrimental reduction in the epoxy matrix on its capability to bear loads. Residual stresses are always detrimental for the matrix in 1-direction longitudinal loading and in the case of biaxial (especially 1-2, 1-3 direction) or even triaxial states of loading small loading strains could cause debonding at the fibre/matrix interface.

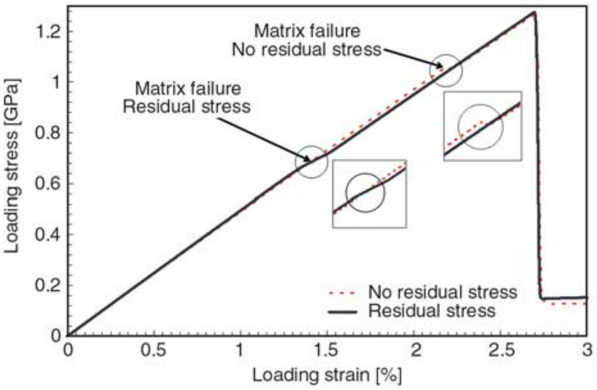

Figure 8. Global stress-strain curve in 1-direction for uniaxial tensile loading for $V_f = 60\%$. Failure criteria: von Mises for the fibre and Raghava for the matrix.

4.2.2. Uniaxial tensile loading along 2-direction and 3-direction

On transverse uniaxial tensile loading along the 2-direction, the Maximum Principal Stress criterion predicts the damage initiation (represented by black shading) to start from the corners of the RVE (Figure 9a), while the failure propagates within the matrix along the edges of the micro-model (Fig-

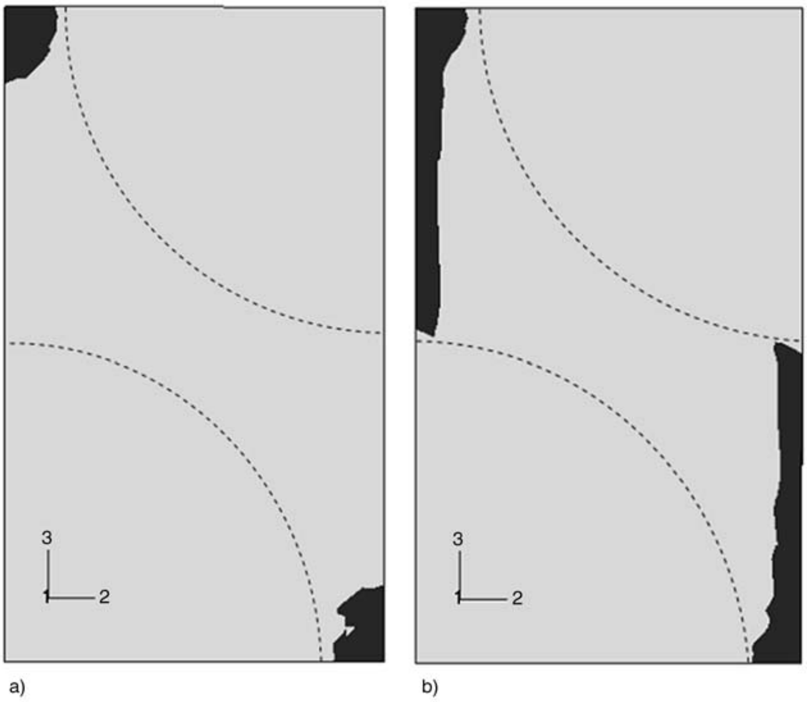

Figure 9. Damage initiation (a) and evolution (b) under uniaxial transverse tensile loading along 2-direction evaluated by means of the Maximum Principal Stress with no residual stress ($V_f = 60\%$)

ure 9b). The evolution of damage for uniaxial tensile loading in the 2-direction in the residual stress analysis is shown in Figure 10. The residual stress/strain state corresponds to the conditions of 1% shrinkage strain and 149°C curing temperature. It can be seen that the site of damage initiation and the subsequent evolution are clearly affected by thermal residual stress. In fact, FE analysis proved that the damage initiates at the fibre/matrix interface (Figure 10a) and evolves along the fibre/matrix interface (Figure 10b). The damage onset in the 3-direction with no residual stress takes place at the fibre/matrix interface as depicted in Figure 11. For this load case damage initiation and its evolu-

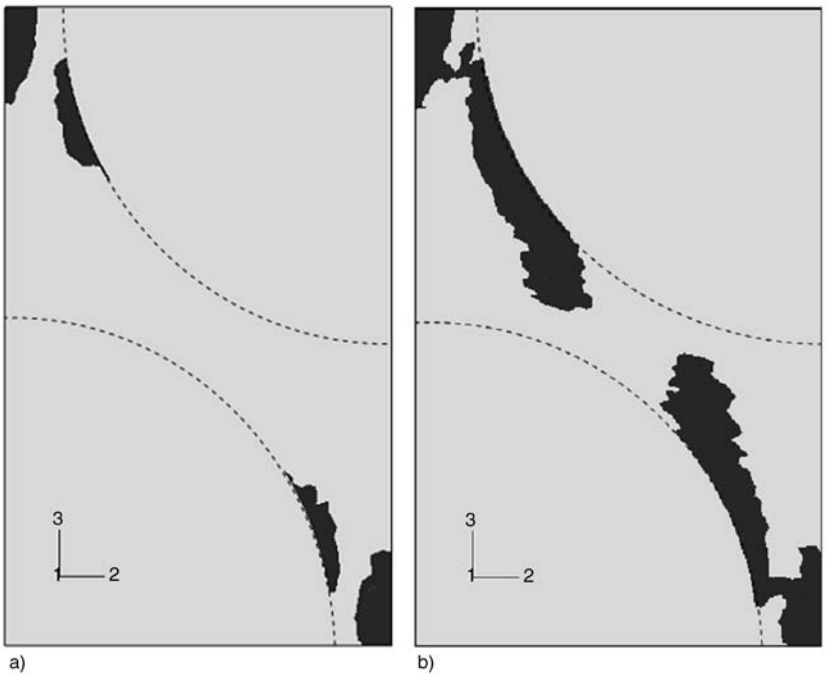

Figure 10. Damage initiation (a) and evolution (b) under uniaxial transverse tensile loading along 2-direction evaluated by means of the Maximum Principal Stress with residual stress ($V_f = 60\%$)

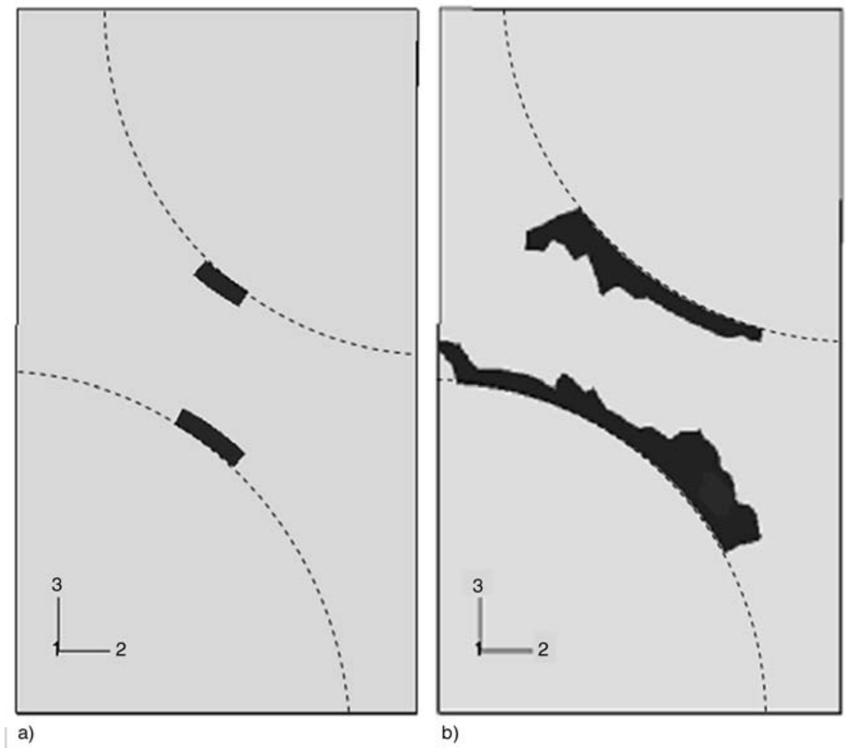

Figure 11. Damage initiation (a) and evolution (b) under uniaxial transverse tensile loading along 3-direction evaluated by means of Maximum Principal Stress criterion with residual stress ($V_f = 60\%$)

tion are not affected significantly by the presence of residual stresses. A crucial result is that the initiation of the damage depends on the mode of loading: 2-direction or 3-direction. As displayed in Figure 9a and Figure 11a the damage onset occur within the matrix in different areas. Specifically, in the 2-direction, damage takes place in the corners of the RVE and in the 3-direction, at the fibre/matrix interface in the centre of the RVE. The interpretation for such a difference is due to the particular *line of symmetry* [35] in the RVE under investigation in which fibres are assembled with a hexagonal packing array (Figure 12). Hence the stress field, distributed symmetrically about the line of symmetry, is different than in a square packing array. During the damage analysis, the global stress-strain response in the loading direction was monitored and an example of results is given in Figure 13 for the cases with and without residual stress. For both cases, the carried stress starts to drop from the point of damage initiation. Once damage is initiated, the model tends to fail suddenly. Thus, the initial failure strain level is also the final failure level for transverse loading. This brittle behaviour is also observed under the 3-direction loading. In Figure 14 the dependence of ultimate strength on fibre content is displayed for these load directions in the case of *no residual stress*. The

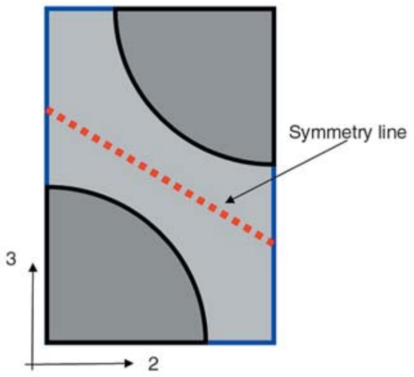

Figure 12. Line of symmetry in a RVE (hexagonal packing array)

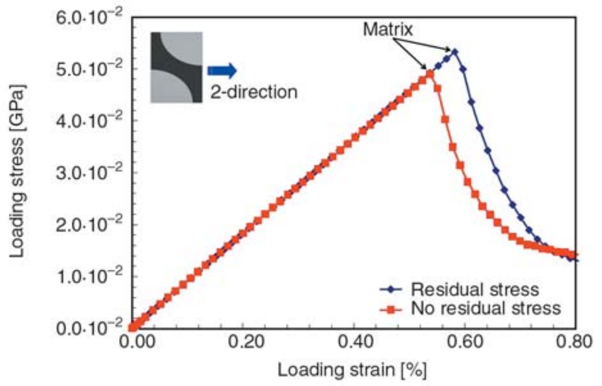

Figure 13. Global stress-strain curve in 2-direction for uniaxial transverse tensile loading

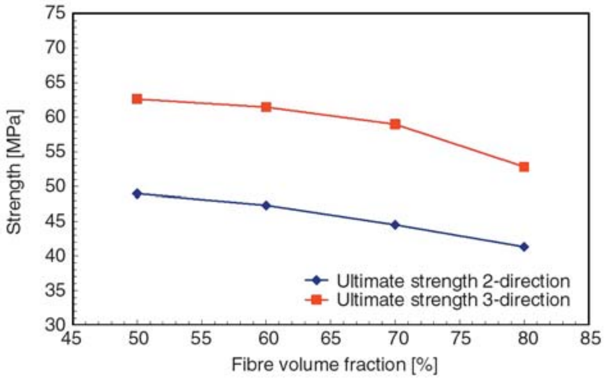

Figure 14. Comparison of ultimate strength for 2-direction and 3-direction loading by using the Maximum Principal Stress criterion. No residual stress applied.

comparison between the strengths predictions using the Maximum Principal Stress and the Raghava failure criteria at different fibre content has an immediate consequence. In fact, the Raghava failure criterion shows the same location in predicting damage onset for the all cases (no-residual stress and residual stress, 2- and 3-direction loading state) but it is always less conservative in terms of ultimate strength (Figure 15 and Figure 16). Furthermore, the presence of residual stress in the 2-direction (Figure 17) and 3-direction loading is in general beneficial. Residual stresses, arising during the simulated manufacturing process, imply a redistribution of the internal stress field which in general leads to lower stresses within the resin and, to improve the ability to bear loads in the transverse directions. Numerical models with a low fibre volume fractions undergo a detrimental effect due to thermal residual stress when the model is loaded in the 3-direction. After cooling the highest values of residual stresses in the matrix are concentrated along the fibre/matrix interface in particular areas but the evolution of the stress field by applying a displacement in 3-direction is dissimilar. In fact, for high fibre volume fractions stresses tend to spread internally within the resin whilst for low fibre contents they remain highly concentrated at the interface throughout the analysis, weakening this area significantly. Hence, residual stresses could play an important role in decreasing the overall response of the composite negating the potential beneficial effects for 2- and 3-direction transverse loading and producing a drastic failure of the composite.

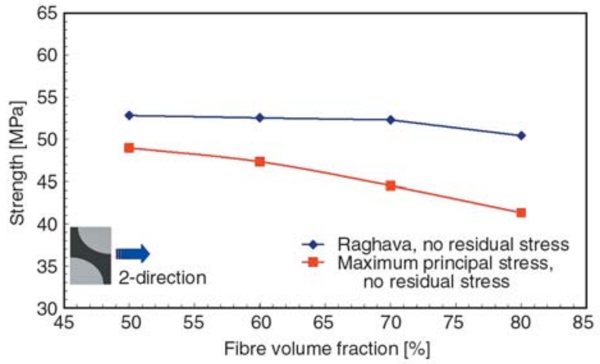

Figure 15. Trend of ultimate strength [MPa] in 2-direction evaluated with Maximum Principal Stress and Raghava failure criteria. No residual stress.

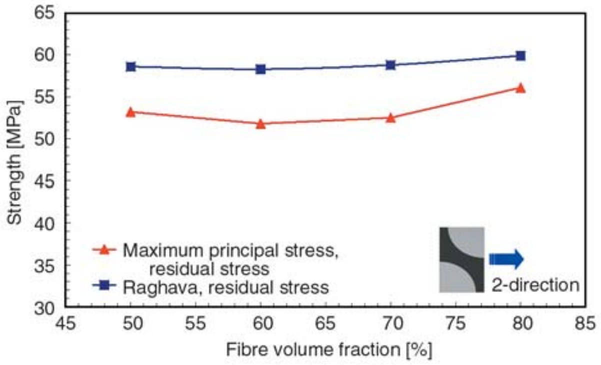

Figure 16. Trend of ultimate strength [MPa] in 2-direction evaluated with Maximum Principal Stress and Raghava failure criteria. Effect of residual stress.

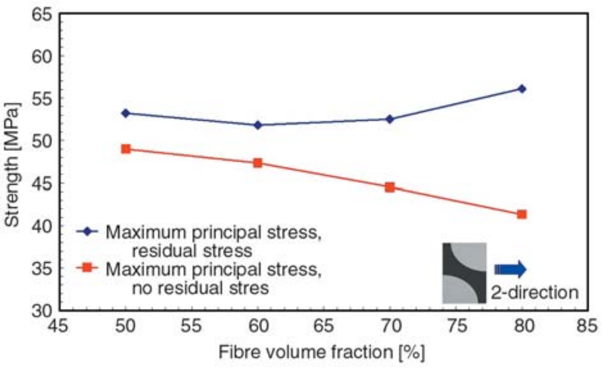

Figure 17. Ultimate strength [MPa] with and without residual stress (2-direction)

5. Conclusions

Residual stress and its effect on transverse and longitudinal failure of UD glass fibre/epoxy resin composites were studied using a micromechanical RVE model and the finite element methods. The overall residual stress is determined by considering two contributions: volume shrinkage of matrix resin from the crosslink polymerization during isothermal curing and thermal contraction of both resin and fibre as a result of cooling from the curing temperature to room temperature. Analyses confirm the isothermal residual stress during curing can be considered negligible compared to the thermal residual stress due to cooling. A study of two different failure criteria was also performed for the epoxy matrix in order to evaluate differences in the capability to predict failure. The assessment of these failure criteria has proved their capability to describe qualitatively the material behaviour of the UD composites under longitudinal and transverse loading. Interestingly, energy based failure criteria (e.g. Raghava), also demonstrated in [36], are particular sensitive to high triaxial stresses which arise at the fibre/matrix interface on uniaxial tensile loading parallel to the fibres orientation and, due to the particular assumptions applied to the RVEs (e.g. perfect bonding between fibres and matrix) in these numerical investigations. Numerical analyses have shown that predicted damage initiation and evolution are clearly influenced by the presence of residual stress. In particular, residual stress causes a premature failure in the matrix at a lower strain than with no residual stress conditions on longitudinal loading case (1-direction) and it is always detrimental for the matrix while for the fibre there is no important alteration in terms of ultimate strength. In addition, the effect of residual stress on transverse tensile loading (2- and 3-direction) depends on the fibre volume fraction and produces beneficial results in the 2-direction at the fibre volume fractions studied while, in 3-direction it is detrimental for low fibre volume fractions.

Acknowledgements

This work is funded by the UK Engineering and Physical Sciences Research Council (EPSRC) through the Nottingham Innovative Manufacturing Research Centre (NIMRC).

References

[1] Zahl D. B., McMeeking M. R.: The influence of residual stress on the yielding of metal matrix composites. Acta Metallurgica et Materialia, **39**, 1117–1122 (1991).

[2] Bigelow C. A.: Thermal residual stresses in a silicon-carbide/titanium [0/90] laminate. Journal of Composites Technology and Research, **15**, 304–310 (1993).

[3] Hull D., Clyne T. W.: An introduction to composite materials. Cambridge University Press, Cambridge (1996).

[4] Fiedler B., Hojo M., Ochiai S.: The influence of thermal residual stresses on the transverse strength of CFRP using FEM. Composites Part A: Applied Science and Manufacturing, **33**, 1323–1326 (2002).

[5] Asp L. E., Berglund L. A., Talreja R.: Prediction of matrix-initiated transverse failure in polymer composites. Composites Science and Technology, **56**, 1089–1097 (1996).

[6] Asp L. E., Berglund L. A., Gudmundson P.: Effects of a composite-like stress state on the fracture of epoxies. Composites Science and Technology, **53**, 27–37 (1995).

[7] Asp L. E., Berglund L. A., Talreja R.: A criterion for crack initiation in glassy polymers subjected to a composite like stress state. Composites Science and Technology, **56**, 1291–1301 (1996).

[8] Fiedler B., Hojo M., Ochiai S., Schulte K.: Yield criteria for polymers in composite-like stress state. in 'Proceeding of the 23rd Symposium of the Society of Composite Materials Japan. Yamagata, Japan', 154–155 (1998).

[9] Fiedler B., Hojo M., Ochiai S., Schulte K., Ando M.: Failure behavior of an epoxy matrix under different kinds of static loading. Composites Science and Technology, **61**, 1615–1624 (2001).

[10] Fiedler B., Hojo M., Ochiai S., Schulte K., Ochi M.: Finite-element modeling of initial matrix failure in CFRP under static transverse tensile load. Composites Science and Technology, **61**, 95–105 (2001).

[11] Gramoll K. C., Walker K. P., Freed A. D.: An overview of self-consistent methods for fibre reinforced composites. NASA TM 103713 (1991).

[12] Mori T., Tanaka K.: Average stress in matrix and average elastic energy of materials with misfitting inclusions. Acta Metallurgica, **21**, 571–574 (1973).

[13] Yeh N. M., Krempl E.: The influence of cool-down temperature histories on the residual stresses in fibrous metal-matrix composites. Journal of Composite Materials, **27**, 973–995 (1993).

[14] Uemura M., Iyama H., Yamaguchi Y.: Thermal residual stresses in filament-wound carbon-fibre-reinforced composites. Journal of Thermal Stresses, **2**, 393–412 (1979).

[15] Mikata Y., Taya M.: Stress field in a coated continuous fiber composite subjected to thermo-mechanical loadings. Journal of Composite Materials, **19**, 554–578 (1985).

[16] Jayaraman K., Reifsnider K. L.: Residual stresses in a composite with continuously varying Young's modulus in the fibre/matrix interphase. Journal of Composite Materials, **26**, 770–791 (1992).

[17] Nimmer R. P.: Fibre-matrix interface effects in the presence of thermally induced residual stress. Journal of Composites Technology and Research, **12**, 65–75 (1990).

[18] Wisnom M. R.: Factors affecting the transverse tensile strength of unidirectional continuous silicon carbide fibre reinforced 6061 Aluminium. Journal of Composite Materials, **24**, 707–726 (1990).

[19] Nedele M. R., Wisnom M. R.: Finite element micromechanical modelling of a unidirectional composite subjected to axial shear loading. Composites, **25**, 263–272 (1994).

[20] Aghdam M. M., Pavier M. J., Smith D. J.: Micromechanical modelling of metal matrix composites subjected to combined thermal and shear loading. in 'Proceedings of the Sixth International Conference on Computer Methods in Composite Materials (CADCOMP 98). Montreal, Canada', 321–330 (1998).

[21] Aghdam M. M., Pavier M. J., Smith D. J.: Micromechanics of off-axis loading of metal matrix composites using finite element analysis. International Journal of Solids and Structures, **38**, 3905–3925 (2001).

[22] Sun C. T., Vaidya R. S.: Prediction of composite properties from a representative volume element. Composites Science and Technology, **56**, 171–179 (1996).

[23] Zhao L. G., Warrior N. A., Long A. C.: A thermo-viscoelastic analysis of process-induced residual stress in fibre-reinforced polymer-matrix composites. Material Science and Engineering: A. Structural Materials: Properties, Microstructure and Processing, **452**, 483–498 (2007).

[24] Soden P. D., Hinton M. J., Kaddour A. S.: Lamina properties, lay-up configurations and loading conditions for a range of fibre-reinforced composite laminates. in 'Failure criteria in fibre-reinforced-polymer composites' (eds.: Soden P. D., Hinton M. J., Kaddour A. S.) Elsevier, Oxford, 30–51 (2004).

[25] Zhang Y., Xia Z., Ellyin F.: Evolution and influence of residual stress/strains of fiber reinforced laminates. Composites Science and Technology, **64**, 1613–1621 (2004).

[26] Altenbach H., Tushtev K.: A new static failure criterion for isotropic polymers. Mechanics of Composite Materials, **37**, 475–482 (2001).

[27] Altenbach H.: A unified phenomenological limit state criterion for ductile and brittle materials. in 'Conference on Plasticity and Impact Mechanics, New Delhi, India' 42–51 (2003).

[28] Tabiei A., Ivanov I.: Materially and geometrically non-linear woven composite micro-mechanical model with failure for finite element simulations. International Journal of Non-Linear Mechanics, **39**, 175–188 (2004).

[29] Tabiei A., Song G., Jiang Y.: Strength simulation of woven fabric composite materials with material non-linearity using micromechanics based model. Journal of Thermoplastic Composite Materials, **16**, 5–20 (2003).

[30] Blackketter D. M., Walrath D. E., Hansen A. C.: Modelling damage in a plain weave fabric-reinforced composite material. Journal of Composites Technology and Research **15**, 136–142 (1993).

[31] Hibbitt D., Karlsson B., Sorensen P.: ABAQUS v6.5. User's Manuals. Providence (RI) (2005).

[32] Zhang L., Ernst L. J., Brouwer H. R.: Transverse behavior of a unidirectional composite (glass fibre reinforced unsaturated polyester). Part II. Influence of shrinkage strains. Mechanics of Materials, **27**, 37–61 (1998).

[33] Eom Y., Boogh L., Michaud V., Sunderland P., Manson J.-A.: A Stress-initiated void formation during cure of a three-dimensionally constrained thermoset resin. Polymer Engineering and Science, **41**, 492–503 (2001).

[34] Lange J., Toll S., Manson J.-A. E., Hult A.: Residual stress build-up in thermoset films cured below their ultimate glass transition temperature. Polymer, **38**, 809–815 (1997).

[35] Li S.: On the unit cell for micromechanical analysis of fibre-reinforced composites. in 'Proceeding of the Royal Society of London, London, UK', Vol 455, 815–838 (1999).

[36] Maligno A. R.: Finite element investigations on the microstructure of composite materials. PhD Thesis, The University of Nottingham (2008).

eXPRESS Polymer Letters Vol.2, No.9 (2008) 677–686
Available online at www.expresspolymlett.com
DOI: 10.3144/expresspolymlett.2008.80

Potassium diperiodatocuprate-mediated preparation of poly(methyl methacrylate)/organo-montmorillonite composites via *in situ* grafting copolymerization

K. L. Deng[1]*, *J. Liu*[1], *G. Z. Wang*[2], *H. Tian*[1], *X. B. Ren*[1], *H. B. Zhong*[1], *P. F. Zhang*[1]

[1]College of Chemistry and Environmental Science, Hebei University, Baoding, 071002, China
[2]Zunhua Public Bureau Hygienic Supervision Institute, Zunhua, 064200, China

Received 29 June 2008; accepted in revised form 17 August 2008

Abstract. In this study, potassium diperiodatocuprate (Cu^{3+}) was selected as an initiator to prepare poly(methyl methacrylate)/organo-montmorillonite composites (OMMT-*g*-PMMA) by *in situ* graft copolymerization. Three synthetic parameters were systematically evaluated as a function of the temperature, the concentration of initiator, pH and the ratio of MMA to OMMT. It was found that Cu^{3+} was a highly efficient initiator for the preparation of OMMT-*g*-PMMA i.e., monomer conversion and grafting efficiency were as higher as 95%. The X-ray diffraction measurement showed the intercalation of PMMA chains into OMMT layers on base of an increasing basal spacing after polymerization. FTIR analysis also suggested that the PMMA chains were effectively grafted onto OMMT substrate. The enhanced thermal stabilities of OMMT-*g*-PMMA composites were confirmed by the thermal gravimetric analysis (TGA). Finally, a single-electron-transfer mechanism was proposed to illustrate the formation of radicals and the preparation process of OMMT-*g*-PMMA composites. Cu^{3+} can be used as an effective and practical initiator in preparing the organic/inorganic composite due to its high grafting efficiency and the milder reaction condition.

Keywords: *polymer composites, potassium diperiodatocuprate, montmorillonite*

1. Introduction

Organic/inorganic nanocomposite, as a special type of material, has attracted considerable interests in the recent years [1–3]. The nanocomposites were actually obtained by the successful incorporation of an organic polymer and an inorganic component into one single material. Various minerals [4, 5], metal particles [6], and metal oxides [7] are often used as the inorganic component in the composites and the organic polymer includes polystyrene [8], polymethyl methacrylate [9], polypropylene [10], and so on. The organic/inorganic composites usually differ from both the original pure polymers and the inorganic particles in some chemical and physical properties. In comparison with the single component, the composites often show many unique appealing properties such as enhanced mechanical property [11], fire retardance and excellent thermal stability [12, 13], good ionic conductivity [14] and gas barrier property [15]. For example, the elastic modulus of the nano-composite composed of polyester and 5% nanoclay was increased to 6646 from 5393 MPa for unreinforced polyester [11]. The enhancement in ion conductivity of polymethyl methacrylate/CeO_2 was observed due to the increase in the number of charge carriers by reaction of CeO_2 with anion and cation [14].

To date, several synthetic procedures have been developed in order to prepare the composites. For instance, the typical synthetic methods used to pro-

---

*Corresponding author, e-mail: dkl369@hbu.edu.cn

duce polymer/mineral clay nanocomposites are *in situ* intercalative polymerization [16], exfoliation-adsorption [17], melt intercalation [18] and template synthesis etc. [19]. It is well known that the grafting reaction of monomers onto some inorganic particles is also an effective strategy to prepare the corresponding organic/inorganic composites [20–23]. In the preparation of these composites, the polymers chains grow from inorganic material substrates by the grafting reaction. Besides, the terminal reactive groups on the polymer chains can directly react with the reactive ones bound to the substrates. Luo *et al.* described the preparation of a novel nano-superabsorbent composite by graft copolymerization of acrylamide and acrylic acid onto montmorillonite/starch initiated using ^{60}Co-ray irradiation [20]. The polymer/silica composite was synthesized via the grafting copolymerization of the polymers having pendant peroxycarbonate groups and the silica with azo groups in the presence of vinyl acetate [22].

In our previous work [24–28], many graft copolymerizations initiated by the high valence metal ions of the common monomers, especially onto the synthetic and natural polymers have been investigated widely. The high valence transition metals ions, including Ni^{4+}, Ag^{3+} and Cu^{3+} ions, have proved to be the highly efficient initiators. For instance, potassium diperiodatocuprate was successfully employed to initiate the graft copolymerization of methyl acrylate onto chitosan. On the optimal reaction condition, the grafting efficiency reached as high as 95% [24]. Also, the graft copolymer with high graft parameters from methyl acrylate and poly(vinyl alcohol) was prepared using potassium diperiodatonickelate (Ni^{4+}) or potassium diperiodatoargentate (Ag^{3+}) as the initiators [25, 28]. In the aforementioned studies on the grafting copolymerization, the radicals formed by the redox reaction of the high valence metal ions with some reductive groups on the substrate. Actually, the redox reaction of the metal ions underwent a two-step single electron-transfer progress. This radical-producing mechanism has been used to explain the formation of the graft sites and the initiation in the graft copolymerization [24–26]. If the high valence metal ions are used to initiate the graft copolymerization of the common monomers onto some inorganic materials such as glass fiber, montmorillonite, and kaolin, a new method for the preparation of the corresponding composites can be developed. Poly (methyl methacrylate) (PMMA) and montmorillonite were selected as the two organic/ inorganic components in the composite prepared in this study. PMMA is an amorphous, transparent polymer and widely used in various fields. On the other hand, montmorillonite is often selected as the inorganic component in the preparation of organic/inorganic composite. Because of the hydrophobic nature of montmorillonite, it is often modified by exchanging of an alkyl ammonium ions with the cations between the silicate layers. As an extension of our previous work, the high valence metal ions were applied to the inorganic material field in this study, that is, potassium diperiodatocuprate (Cu^{3+}) was used as an initiator for the preparation of PMMA/OMMT composite via the *in situ* grafting copolymerization. The synthetic parameters for composites were evaluated by varying the temperature, monomer concentration, and initiator concentration. The experimental result has shown that potassium diperiodatocuprate is an efficient initiator for the synthesis of OMMT-*g*-PMMA composite via the grafting copolymerization. Theoretically speaking, the titled OMMT-*g*-PMMA composite can be directly used as an inorganic clay-modified material or a new potential blend-compatilizer in the modification of organic polymers with inorganic minerals.

2. Experimental section

2.1. Materials

Organophilic montmorillonite (OMMT) (DK-2) used in this study was purchased from Fenghong Clay Chemicals Co. Ltd., Zhejiang Province, and received as fine particle powders. The surfactant used to modify montmorillonite was a long-chain organic amine salt. Methyl methacrylate (MMA) was washed successively with aqueous sodium hydroxide and distilled water to remove the hydroquinone inhibitors, and then it was dried over anhydrous sodium sulfate overnight and finally distilled. The grafting initiator, potassium diperiodatocuprate (Cu^{3+}) was synthesized and characterized according to the reported literature [24, 29]. The other chemicals were analytical grade and were used without any further purification.

2.2. Measurements

The structures of OMMT-*g*-PMMA, OMMT and pure PMMA were characterized by Fourier transform infrared spectrum with an FTS-40 spectrophotometer (BIORAD, USA) in potassium bromide pellets. The X-ray diffraction pattern was measured with a Rigaku D/MAX 2400 X-ray diffractometer. The X-ray beam was derived from nickel-filtered CuK$_\alpha$ (λ = 0.154 nm) radiation in a sealed tube operated at 40 kV and 200 mA. The experiments were conducted in the angle range 1–50°, at a scanning rate of 8°/min and a scanning step of 0.02°. The thermo-gravimetric analysis (TGA) curves were completed with a Shimadzu DGC-40 DTATG apparatus (Shimadzu, Japan) in N_2 atmosphere at a heating rate of 10°C/min.

2.3. Preparation of OMMT-*g*-PMMA composite and treatment

A series of the graft copolymerizations were carried out in a glass tube (20 mm in diameter and 200 mm in length) equipped with a magnetic bar. In the typical procedure, 0.5 g OMMT, deionized water and required amount of MMA were added into a tube. Then, several standard cycles of evacuation and backfill with dry and pure nitrogen was performed to thoroughly remove oxygen. The tube was charged with the oxygen-free Cu^{3+} aqueous solution and water-acetone by a syringe. The total volume of reaction system was controlled at 6 ml by the addition of mixed solvent (water/acetone = 3:1). Herein, it is necessary to state that the aim of addition of some acetone is to maintain more uniform dispersion of OMMT during the graft copolymerization. The graft copolymerization was performed under the designated conditions of different monomer concentrations, initiator concentrations, pH and temperatures. After a definite time, the polymerization was terminated by several drops of hydrochloric acid solution. Subsequently, the reaction mixture was poured into a large amount of methanol, and the crude graft copolymer was filtered through a weighted, sintered glass funnel. The crude graft copolymer was dried at 90°C in air for several hours and then dried to a constant weight under vacuum at 60°C. The exhaustive Soxhlet extraction with acetone for 48 h was performed to remove some homopolymers in the crude graft copolymer. The resulting OMMT-*g*-PMMA composite was dried at 60°C to a constant weight under vacuum.

Monomer conversion ($C\%$), grafting percentage ($P\%$) and grafting efficiency ($E\%$) were designated as the synthetic parameters in the preparing OMMT-*g*-PMMA composites, and were defined in the following manner (see Equations (1)–(3)):

$$C\% = (\text{total weight of PMMA} \div \text{weight of MMA charged})\cdot 100\% \tag{1}$$

$$P\% = (\text{weight of PMMA grafted} \div \text{weight of substrate})\cdot 100\% \tag{2}$$

$$E\% = (\text{weight of PMMA grafted} \div \text{total weight of PMMA formed})\cdot 100\% \tag{3}$$

3. Results and discussion

3.1. Effect of the different factors on synthetic parameters

3.1.1. Effect of Cu^{3+} concentration

The effect of Cu^{3+} concentration on synthetic parameters was investigated when the other reaction conditions are kept unchanged. As shown in Figure 1, the three synthetic parameters exhibited a considerable dependence on the Cu^{3+} concentration, especially for $C\%$ and $P\%$. With increasing Cu^{3+} concentration in the range of 0.6–0.8·10^{-3} mol/l, $C\%$, $P\%$, and $E\%$ all increased quickly. For example, when the Cu^{3+} concentration was 0.65·10^{-3} and 0.80·10^{-3} mol/l, $C\%$ and $P\%$ reached to 79.9 from 46.2%, and 508 from 222%, respectively. However, beyond the Cu^{3+} concentration of 0.8·10^{-3} mol/l, $C\%$, and $P\%$ are found to

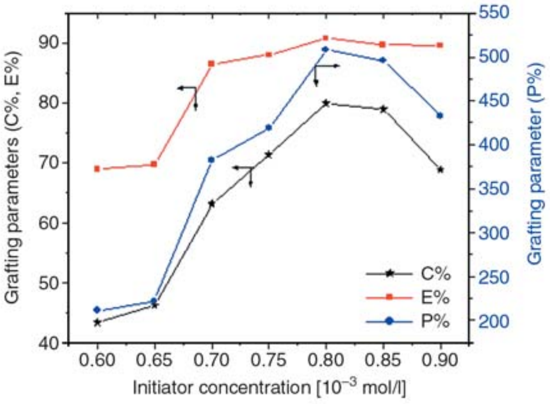

Figure 1. Effect of initiator concentration on synthetic parameters (time = 3 h; temperature = 25°C; MMA/OMMT = 8; pH = 11.7)

decrease. In another word, the optimum value of Cu^{3+} concentration was $0.8 \cdot 10^{-3}$ mol/l in this study. In the lower concentration of Cu^{3+} ranging 0.6–$0.8 \cdot 10^{-3}$ mol/l, the higher Cu^{3+} concentration in the reaction system led to increasing in the number of macro-radicals formed by redox reaction of Cu^{3+}. Therefore, *C%*, *P%* and *E%* increased as Cu^{3+} concentration grew up. A similar observation was also found in the Cu^{3+}-initiated graft copolymerization of acrylic acid [30]. If, however, excessive Cu^{3+} ions were added into the reaction system, the probability of the collision between Cu^{3+} ions with the radicals formed was greatly enhanced. As a result, the partial radicals produced in the reaction were again converted into some inert species by the excessive Cu^{3+} ions [24]. This side-reaction likely decreased the number of grafting radicals formed in the system and also terminated the continuous propagation of some copolymer chains. It is necessary to mention that compared with *C%* and *P%*, *E%* was basically independent on the higher Cu^{3+} concentration range. This experimental result indicated the homo-polymerization of MMA was not increased with Cu^{3+} concentration.

In order to testify the effective grafting copolymerization initiated by Cu^{3+} ions, the comparative experiments have been conducted. When potassium persulfate (2% to monomer) rather than Cu^{3+} was added into the tube with required amount of MMA, acetone/water, and OMMT at 45°C, no obvious polymer was obtained after 2 h. At the same time, no polymerization behaviors were observed in the OMMT-free reaction system using Cu^{3+} as initiators. If the above-mentioned experiment contained OMMT and MMA was carried out at 45°C using Cu^{3+} as an initiator, a large amount of polymers were obtained after 2 h. This phenomenon implied that Cu^{3+} ion acted as an effective redox initiator for the polymerization of MMA at lower temperature. The radicals were easily formed through the redox reaction of Cu^{3+} ion with some reductive groups on OMMT. For potassium persulfate, no obvious decomposition takes place at 45°C to produce the corresponding radicals. The characteristics of the formation of radicals via the Cu^{3+} redox reaction have been reported in several publications [29–31].

3.1.2. Effect of the ratio of MMA to OMMT

The effect of MMA/OMMT ratio on the three synthetic parameters is depicted in Figure 2. With increasing the ratio of MMA to OMMT, *P%*, *E%* and *C%* increase drastically. For instance, as the ratio of MMA to OMMT was fixed at 5 and 7, *C%* reached 47.7, 83.7%, and *P%* were 189, 480%, respectively. Apparently, the concentration of MMA was heightened with increasing the ratio of MMA/OMMT because the total volume of reaction system and OMMT was kept unchanged. In addition, the number of radical sites on OMMT could be considered as constant when other reaction conditions were kept invariable. According to the basic principle of radical polymerization, *C%* and *P%* affirmatively augmented with an increasing of MMA/OMMT ratio. The higher concentration of MMA in close vicinity to each radical site resulted in the quicker polymerization rate and the production of more polymers in the reaction.

Additionally, three synthetic parameters showed remarkable declining tendency when the ratio of MMA/OMMT was larger than 8. As the ratio of MMA/OMMT was 8 and 10, *C%* decreased to 18.9 from 84.7%; *P%* went down to 85 from 623%, respectively. The higher ratio of MMA/OMMT implied that the less water was added into the system because of the fixed volume in the polymerization. Furthermore, the graft copolymerization was carried out in heterogeneous systems because Cu^{3+} dissolves only in water, MMA, however, dissolves in some organic solvents, and OMMT is not soluble in common solvent. As a result, the collision probability between OMMT and Cu^{3+} was greatly decreased at the higher ratio of MMA/OMMT. The

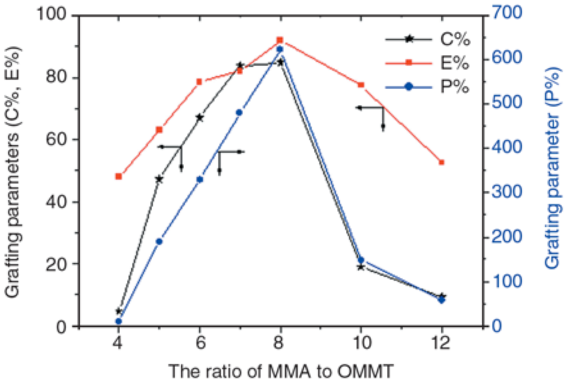

Figure 2. Effect of the ratio of MMA to OMMT on synthetic parameters (time = 3 h; temperature = 25°C; $[Cu^{3+}] = 0.8 \cdot 10^{-3}$ mol/l; pH = 11.7)

number of radicals was decreased with increasing ratio of MMA/OMMT, finally resulting in a considerable fall in the synthetic parameters.

3.1.3. Effect of temperature

The effect of reaction temperature on synthetic parameters has been studied by varying the temperature in the range of 0–65°C. As shown in Figure 3, it is found that *E%* is slightly dependent on the reaction temperature between 25 and 50°C. On the other hand, *C%* and *P%* exhibited a remarkable dependence on the temperature selected in graft copolymerization. The activation energy was a small positive value when investigating the redox reaction of Cu^{3+} ions with some reducing groups including amino and hydroxyl groups [29, 32]. Furthermore, the radicals were produced via a single electron transfer process in Cu^{3+} redox reaction and initiated the polymerization of acrylonitrile [29, 32]. So, the formation rate of radicals is accelerated with increasing temperature, leading to the increase of *C%* and *P%*. For example, when the reaction temperature was controlled at 12 and 25°C, *C%* increased to 94.5 from 35.1% and P% climbed up to 580 from 229%, respectively.

In addition, *C%* and *P%* decreased drastically as the temperature was further increased to 65 from 25°C. The reason for this phenomenon is mainly ascribed to the following fact. Many radicals were formed via the redox reaction of Cu^{3+} ions within a short time period at higher temperature. The graft copolymerization was conducted in the heterogeneous system because of the different solubilities of MMA, OMMT, and Cu^{3+} ions. It took a certain time for the MMA to approach the formed radicals via diffusion and subsequently to polymerize. In this case, many radicals were likely scavenged through the bimolecular termination or other by-reactions before the radicals initiated the polymerization of MMA. Consequently, *C%* and *P%* exhibited a decreasing tendency with increasing the temperature. At the higher temperature, the chain transfer reaction of the radicals to the molecules except OMMT was also enhanced owing to the increased activity of the radicals. Therefore, the synthetic parameter *E%* showed decreasing trend to some extent especially over 50°C. Savina *et al*. presented the similar results when investigating the effect of temperature on the grafting parameters in graft copolymerization [30]. By the overall comparison among three synthetic parameters, the other experiment was carried out at 25°C to obtain the higher synthetic parameters.

3.1.4. Effect of pH

Figure 4 has shown the effect of pH value on the synthetic parameters. In this study, the hydrochloric acid or potassium hydroxide solution were used as pH-adjustor to control the required alkalinity in the reaction system. The synthetic parameters were evaluated under the different pH value in the range of 8.8–13.0. It was found that *C%*, *E%* and *P%* were significantly dependent on pH value in the reaction system. The three synthetic parameters increased drastically with pH value, and thereafter went down as the pH value further increased. *C%* and *P%* went up to the highest value (74.3 and 475%) at pH = 11.7, whereas the graft parameter

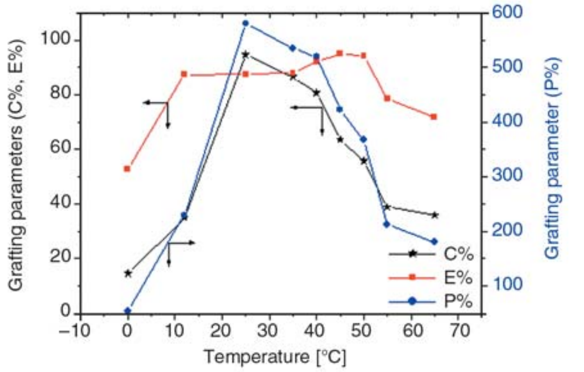

Figure 3. Effect of temperature on synthetic parameters (time = 3 h; $[Cu^{3+}] = 0.8 \cdot 10^{-3}$ mol/l; MMA/OMMT = 8; pH = 11.7)

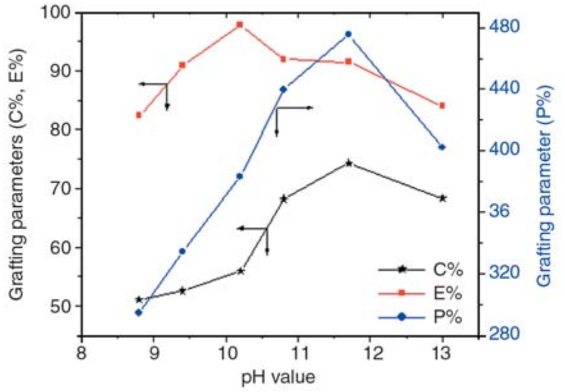

Figure 4. Effect of pH on synthetic parameters (time = 3 h; temperature = 25°C; $[Cu^{3+}] = 0.8 \cdot 10^{-3}$ mol/l; MMA/OMMT = 8)

E% reached its highest value at pH = 10.2. The results indicated the presence of optimal pH value in the preparation of the composites.

The two main active forms of Cu^{3+} complexes including $[Cu(H_3IO_6)_2(OH)_2]^{3-}$ and $[Cu(H_2IO_6)(H_3IO_6)]^{2-}$ have been detected in alkaline medium. Cu^{3+} complex species actually vary with the alkalinity in the medium, because the dissociation of the various species of H_5IO_6 obviously depends on the pH value [29, 32]. Most importantly, the different forms of Cu^{3+} complexes have different reactivity in the redox reaction. At excessively low or high pH range, the $H_3IO_6^{2-}$ and $H_2IO_6^{3-}$ ions all decrease, which further induces to decrease the concentration of active $[Cu(H_3IO_6)_2(OH)_2]^{3-}$ and $[Cu(H_2IO_6)(H_3IO_6)]^{2-}$ species. Thus, pH value plays a key role in the formation of radicals in the Cu^{3+} redox reaction, and determines the number of radicals used for the polymerization. By the estimation based on the dissociation constants of periodic acid [32], the pH value at which the higher synthetic parameters were obtained is basically close to that for the existence of $H_3IO_6^{2-}$ and $H_2IO_6^{3-}$ ions. The same effecting behaviors of pH on the grafting parameters were also observed in the other Cu^{3+}-initiated grafting system [30]. Because the property of composites mainly depends on *P%* rather than *E%*, we selected pH = 11.7 to carry out other experiments.

3.2. Characterization of the OMMT-*g*-PMMA composites

3.2.1. FTIR measurements

In order to illustrate the structural change before and after polymerization, the FTIR spectra of original OMMT, the pure PMMA, and OMMT-*g*-PMMA composite (*P%* = 600%) were recorded in the range of 4000–400 cm^{-1}. As shown in Figure 5, the two peaks at about 3600 and 3450 cm^{-1} in the spectrum of OMMT implied the presence of the reactive groups including –OH and –NH–. In the FTIR spectrum of the OMMT-*g*-PMMA composite, the strong absorption bands at 1731.8 cm^{-1} was observed, corresponding to the characteristics of C=O stretching vibration from PMMA. Also, the characteristic absorption bands at 1149.2, 1192, and 1243.2 cm^{-1} could be ascribed to the C–O–C stretching vibration in PMMA chains [21]. Furthermore, several characteristic absorption peaks attributed to OMMT were also recorded in the FTIR spectrum of the composite. For instance, the absorption peaks at 1036.9 cm^{-1} corresponded to the Si–O–Si stretching vibration from OMMT substrate. The bands at 3620.5 and 3436.1 cm^{-1} were related to the reactive groups in OMMT. From these spectral data, it could be concluded that the composite was consisted of both PMMA and OMMT moieties. Therefore, the PMMA chains were chemically grafted onto OMMT because the composite has been completely extracted with a large amount acetone.

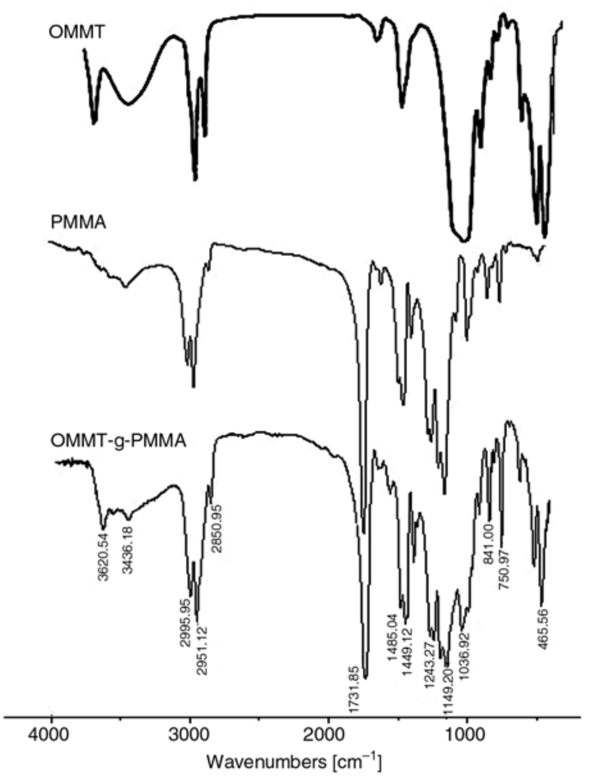

Figure 5. FTIR spectra of OMMT, PMMA and OMMT-*g*-PMMA composites

3.2.2. TGA analysis

The thermo-gravimetric analysis (TGA) of OMMT, PMMA and OMMT-*g*-PMMA (*P%* = 550%) has illustrated the decomposition behaviors under heating in an inert atmosphere. As shown in Figure 6, the weight loss behavior regarding water likely bound to the OMMT-*g*-PMMA was observed in the range of 100–260°C. The second step degradation of OMMT-*g*-PMA composite started at about 275°C, and the final decomposition temperature was found to be 405°C. This process mainly corresponded to the decomposition of the

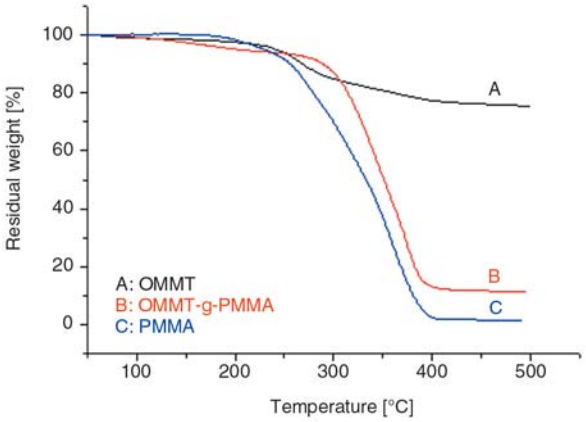

Figure 6. Thermal analysis for OMMT, OMMT-*g*-PMMA and PMMA

organic component in the composite. On the other hand, the pure PMMA exhibited only one step degradation between 180–400°C. Compared with the pure PMMA, the initial decomposition temperature of OMMT-*g*-PMMA was about 95°C higher than that of pure PMMA. The improvement in the thermal stability for OMMT-*g*-PMMA is ascribed to the introduction of OMMT into PMMA. The inorganic clay component effectively absorbed or retarded the heat in the OMMT-*g*-PMMA thermal degradation. In addition, the finally residual weight of OMMT-*g*-PMMA was found to be around 11.8%. This value is in a good agreement with the one calculated from the organic-component content in OMMT and the grafting percentage of sample used.

3.2.3. XRD patterns

As shown in Figure 7, the X-ray diffraction patterns of OMMT, OMMT-*g*-PMMA and the mixture of PMMA and OMMT were measured to investigate the change of OMMT structure after grafting. In the XRD pattern of pure OMMT, several diffraction peaks at 2θ = 3.68, 19.62, and 34.78°, were recorded, which implied the presence of the ordered layer-like structure of OMMT [2]. The basal spacing corresponding to the 2θ = 3.68° was 2.40 nm according to Bragg’s equation. In order to further elucidate the influence of polymerization on the OMMT structure, the XRD of a mixture of the pure PMMA and OMMT was also determined at the same 2θ range. Obviously, except for a broad diffraction peak ascribed to PMMA at 2θ from about 8 to 20°, the XRD pattern of the mixture was almost the same as that of pure OMMT substrate. This result suggested the layer-like structure of OMMT did not change after the simple mixing.

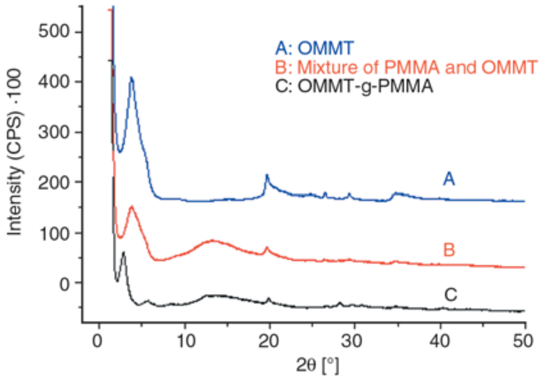

Figure 7. X-ray diffraction patterns of OMMT, OMMT-*g*-PMMA and the mixture of PMMA/OMMT

In the small angle region of the XRD pattern for the composite, however, three sharp diffraction peaks at 2.74, 5.56 and 8.32° were recorded, indicating an ordered structure. Considerably, the diffraction peak at 3.68° attributed to the original OMMT has shifted to 2.74°. According to Bragg’s equation, the corresponding gallery space of the OMMT increased to 3.22 from 2.40 nm after graft polymerization. This result likely was caused by the intercalation of some PMMA chains into the interlayers of OMMT, leading to an increase in the gallery space. From the comparison of three XRD patterns, it could be seen that in the grafting copolymerization, the clay sheets of OMMT were intercalated by the continuous swelling of PMMA chains and finally uniformly dispersed in the organic PMMA formed. As an additional proof, the PMMA chains were grafted onto the substrate OMMT.

3.3. Formation of radicals and preparation of OMMT-*g*-PMMA nanocomposite

The formation of radicals and preparation of nanocomposite via the *in situ* graft copolymerization is shown in Figure 8. First, Cu^{3+} ion is a strong oxidizer in the alkaline aqueous solution [29]. Cu^{3+} ions readily reacted with some reactive groups including hydroxyl and amino groups on OMMT, resulting in the producing of the corresponding radical-cations, as well as Cu^{2+} ions. These radical-cations are chemically bound on the substrate OMMT. And then, the radical-cation further reacted with hydroxyl ion (OH^{-1}) provided by the alkaline medium so as to produce the macroradicals

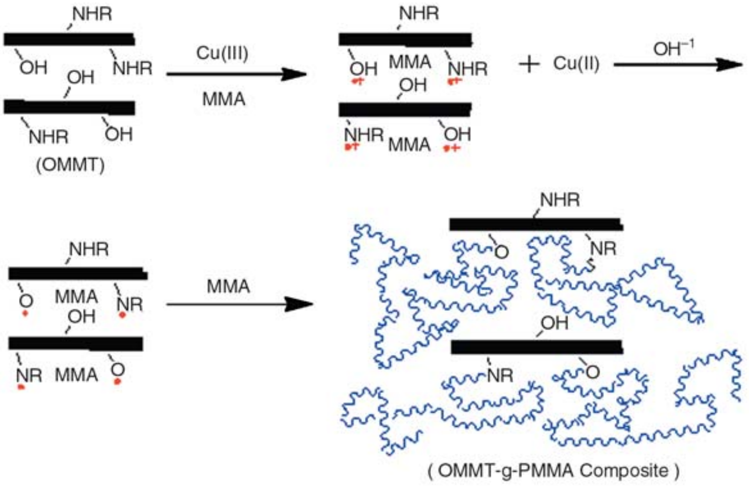

Figure 8. The proposed mechanism for the preparation for the nanocomposite by Cu^{3+}

on OMMT. The macroradicals are sites for the subsequent grafting copolymerization of MMA onto OMMT. The monomers MMA in close vicinity to the macro-radicals were initiated and followed by the quick chain growth of PMMA in the interlayers of OMMT. The similar mechanism about the radical formation and initiation was also proposed by Savina *et al.* [30]. In fact, MMA and Cu^{3+} ions can diffuse into the interlayers of OMMT because of the usage of acetone/water mixture and surfactant used as modifier in OMMT. The interlayer structure of OMMT was intercalated due to the continuous swelling of the PMMA chains. Finally, the fine OMMT particles dispersed homogeneously in the PMMA formed, which was supported by the aforementioned XRD measurement. Because the radicals were generated via the redox reaction of Cu^{3+} with reactive groups in OMMT, nearly all of the PMMA chains were chemically bound to OMMT, not simply mixed. In conclusion, the composites of PMMA and OMMT formed simultaneously in course of the graft copolymerization of MMA onto OMMT.

4. Conclusions

The present article described a new initiator, potassium diperiodatocuprate (Cu^{3+}), for preparing the composite based on OMMT and PMMA through *in situ* polymerization. By investigating the effect of reaction conditions on the synthetic parameters, the optimum of synthetic procedure was given as follow: pH = 11.6; temperature = 25°C; Cu^{3+} concentration is $0.80 \cdot 10^{-3}$ mol/l; ratio of MMA to OMMT is fixed at 8. From the experimental results, it could be seen that Cu^{3+} is an effective and practical initiator for the preparation of the organic/inorganic composite via the *in sui*t polymerization. Moreover, the preparation of the intercalation-type composite could be conducted under milder conditions because of the lower activation energy in Cu^{3+} redox reaction. The grafting of PMMA chain onto OMMT and the improvement in the thermal stability were demonstrated by FTIR, TGA, and X-ray diffraction measurements. Further studies on the mechanical properties of OMMT-*g*-PMMA composite are now in progress.

Acknowledgements

The authors thank the Natural Science Foundation of Hebei Province (B2008000573) for the financial support. And, the authors also would like to thank the Institute of Chemistry, Chinese Academy of Sciences, Beijing, China, for the XRD measurement.

References

[1] Tang E. J., Cheng G. X., Ma X. L.: Preparation of nano-ZnO/PMMA composite particles via grafting of the copolymer onto the surface of zinc oxide nanoparticles. Powder Technology, **161**, 209–214 (2006).
[2] Chow W. S., Mohd Ishak Z. A.: Mechanical, morphological and rheological properties of polyamide 6/organo-montmorillonite nanocomposites. Express Polymer Letters, **1**, 77–83 (2007).
[3] Avella M., Errico M. E., Gentile G.: PMMA based nanocomposites filled with modified $CaCO_3$ nanoparticles. Macromolecular Symposia, **247**, 140–146 (2007).

[4] Qi R. R., Jin X., Zhou C. X.: Preparation and properties of polyethylene-clay nanocomposites by an in situ graft method. Journal of Applied Polymer Science, **102**, 4921–4927 (2006).

[5] Zou H., Ma Q. Q., Tian Y., Wu S. S., Shen J.: Structure and properties of nanocomposites prepared by directly melt blending ethylene-co-vinylacetate and natural montmorillonite. Polymer Composites, **27**, 529–532 (2006).

[6] Psarras G. C.: Hopping conductivity in polymer matrix-metal particles composites. Composites Part A: Applied Science and Manufacturing, **37**, 1545–1553 (2006).

[7] Fan X. W., Lin L. J., Messersmith P. B.: Surface-initiated polymerization from TiO_2 nanoparticle surfaces through a biomimetic initiator: A new route toward polymer–matrix nanocomposites. Composites Science and Technology, **66**, 1198–1204 (2006).

[8] Chen Y., Qian Z., Zhang Z. C.: Novel preparation of magnetite/polystyrene composite particles via inverse emulsion polymerization. Colloids and Surfaces A: Physicochemical and Engineering Aspects, **312**, 209–213 (2008).

[9] Kumar J., Singh R. K., Siwach P. K., Singh H. K., Singh R., Srivastava O. N.: Low field magneto-transport in LBSMO-PMMA composite. Journal of Magnetism and Magnetic Materials, **299**, 155–160 (2006).

[10] Cai L. F., Mai Y. L., Rong M. Z., Ruan W. H., Zhang M. Q.: Interfacial effects in nano-silica/polypropylene composites fabricated by in-situ chemical blowing. Express Polymer Letters, **1**, 2–7 (2007).

[11] Dhakal H. N., Zhang Z. Y., Richardson M. O. W.: Nanoindentation behaviour of layered silicate reinforced unsaturated polyester nanocomposites. Polymer Testing, **25**, 846–852 (2006).

[12] Diagne M., Gueye M., Vidal L., Tidjani A.: Thermal stability and fire retardant performance of photo-oxidized nanocomposites of polypropylene-graft-maleic anhydride/clay. Polymer Degradation and Stability, **89**, 418–426 (2005).

[13] Tidjani A., Wald O., Pohl M-M., Hentschel M. P., Schartel B.: Polypropylene-graft-maleic anhydride-nanocomposites: I-Characterization and thermal stability of nanocomposites produced under nitrogen and in air. Polymer Degradation and Stability, **82**, 133–140 (2003).

[14] Rajendran S., Mahendran O., Kannan R.: Ionic conductivity studies in composite solid polymer electrolytes based on methylmethacrylate. Journal of Physics and Chemistry of Solids, **63**, 303–307 (2002).

[15] Nah C. W., Ryu H. J., Kim W. D., Choi S-S.: Barrier property of clay/Acrylonitrile-butadiene copolymer nanocomposite. Polymers for Advanced Technologies, **13**, 649–652 (2002).

[16] Zhang B., Li Y. F., Pan X. B., Jia X., Wang X. L.: Intercalation of acrylic acid and sodium acrylate into kaolinite and their in situ polymerization. Journal of Physics and Chemistry of Solids, **68**, 135–142 (2007).

[17] Hiroyuki E., Michael M. L.: Synthesis of polymer/1T-TaS_2 layered nanocomposites. Materials Research Bulletin, **37**, 1499–1507 (2002).

[18] Limpanart S., Khunthon S., Taepaiboon P., Supaphol P., Srikhirin T., Udomkichdecha W., Boontongkong Y.: Effect of the surfactant coverage on the preparation of polystyrene-clay nanocomposites prepared by melt intercalation. Materials Letters, **59**, 2292–2295 (2005).

[19] Ballarin B., Facchini M., Dal Pozzo L., Martini C.: Comparison of different porous sol-gel matrices: template synthesis of polythiophene. Electrochemistry Communications, **5**, 625–631 (2003).

[20] Luo W., Zhang W. A., Chen P., Fang Y. E.: Synthesis and properties of starch grafted poly[acrylamide-co-(acrylic acid)]/montmorillonite nanosuperabsorbent via γ-ray irradiation technique. Journal of Applied Polymer Science, **96**, 1341–1346 (2005).

[21] Rong M. Z., Zhang M. Q., Wang H. B., Zeng H. M.: Surface modification of magnetic metal nanoparticles through irradiation graft polymerization. Applied Surface Science, **200**, 76–93 (2002).

[22] Hayashi S., Fujiki K., Tsubokawa N.: Grafting of hyperbranched polymers onto ultrafine silica: post-graft polymerization of vinyl monomers initiated by pendant initiating groups of polymer chains grafted onto the surface. Reactive and Functional Polymers, **46**, 193–201 (2000).

[23] Tsubokawa N., Maruyama K., Sone Y., Shimomura M.: Graft polymerization of acrylamide from ultrafine silica particles by use of a redox system consisting of ceric ion and reducing groups on the surface. Polymer Journal, **21**, 475–481 (1989).

[24] Liu Y. H., Liu Z. H., Zhang Y. Z., Deng K. L.: Graft copolymerizaztion of methyl acrylate onto chitosan initiated by potassium diperiodatocuprate (III). Journal of Applied Polymer Science, **89**, 2283–2289 (2003).

[25] Liu Y. H., Liu X. H., Deng K. L., Liu Z. J.: Graft copolymerization of methyl acrylate onto poly(vinyl alcohol) initiated by potassium diperiodatonickelate(IV). Journal of Applied Polymer Science, **87**, 529–534 (2003).

[26] Liu Y. H., Zhang Y. Z., Liu Z. H., Deng K. L.: Graft copolymerization of butyl acrylate onto casein initiated by potassium diperiodatonickelate(IV) in alkaline medium. European Polymer Journal, **38**, 1619–1625 (2002).

[27] Liu Y. H., Bai L. B., Zhou W. Q., Liu Y. W., Li Y. X., Deng K. L.: Block copolymerization of poly(diethylene glycol phthalic anhydride) and methyl methacrylate initiated by potassium diperiodatonickelate(IV). Journal of Applied Polymer Science. **100**, 1312–1317 (2006).

[28] Liu Y. H., Liu X. H., Liu Y. W., Zhang J. S., Deng K. L., Liu Z. J.: Graft copolymerization of methyl acrylate onto poly(vinyl alcohol) initiated by potassium diperiodatoargentate(III). Polymer International, **53**, 1611–1616 (2004).

[29] Timy P. J., Suresh M. T.: Oxidation of threonine by the analytical reagent diperiodatocuprate(III)–An autocatalysed reaction. Journal of Molecular Structure, **827**, 137–144 (2007).

[30] Savina I. N., Mattiasson B., Galaev I. Y.: Graft polymerization of acrylic acid onto macroporous polyacrylamide gel (cryogel) initiated by potassium diperiodatocuprate. Polymer, **46**, 9596–9603 (2005).

[31] Savina I. N., Galaev I. Y., Mattiasson B.: Anion-exchange supermacroporous monolithic matrices with grafted polymer brushes of *N,N*-dimethylaminoethylmethacrylate. Journal of Chromatography A, **1092**, 199–205 (2005).

[32] Chimatadar S. A., Basavaraj T., Thabaj K. A., Nandibewoor S. T.: Ruthenium(III) catalysed oxidation of gabapentin (neurontin) by diperiodatocuprate(III) in aqueous alkaline medium-A kinetic and mechanistic study. Journal of Molecular Catalysis A: Chemical, **267**, 65–71 (2007).